TITLE

SPARK regulates AGC kinases central to the *Toxoplasma gondii* asexual cycle

AUTHORS

Alice L. Herneisen[1], Michelle L. Peters[1], Tyler A. Smith[1], and Sebastian Lourido[1,*]

[1] Whitehead Institute for Biomedical Research and Department of Biology, Massachusetts Institute of Technology, Cambridge, MA

* Correspondence: lourido@wi.mit.edu

ABSTRACT

Apicomplexan parasites balance proliferation, persistence, and spread in their metazoan hosts. AGC kinases, such as PKG, PKA, and the PDK1 ortholog SPARK, integrate environmental signals to toggle parasites between replicative and motile life stages. Recent studies have cataloged pathways downstream of apicomplexan PKG and PKA; however, less is known about the global integration of AGC kinase signaling cascades. Here, conditional genetics coupled to unbiased proteomics demonstrates that SPARK complexes with an elongin-like protein to regulate the stability of PKA and PKG in the model apicomplexan *Toxoplasma gondii*. Defects attributed to SPARK depletion develop after PKG and PKA are down-regulated. Parasites lacking SPARK differentiate into the chronic form of infection, which may arise from reduced activity of a coccidian-specific PKA ortholog. This work delineates the signaling topology of AGC kinases that together control transitions within the asexual cycle of this important family of parasites.

INTRODUCTION

Apicomplexans parasitize a majority of warm-blooded species, including an estimated quarter of the human population (Jones et al., 2014). Central to parasite success is the ability to transition between different life cycle stages to balance proliferation and transmission (Lourido, 2019). The acute phase of infection by *T. gondii,* a model apicomplexan, induces the pathology of disease. Parasites invade host cells, establish an intracellular niche that subverts innate immune responses, replicate, and exit the host via lysis to establish new sites of infection (Blader et al., 2015). These pathogens transcend the inverted biomolecular gradients within and without the host cell in minutes. Such rapid changes in cellular state depend on signal transduction in *T. gondii* and related apicomplexans. Second messenger cascades within the parasite cytoplasm are especially well-suited to rapidly transduce and amplify signals from a changing environment. Accordingly, apicomplexans—and *T. gondii* in particular—have an expanded repertoire of second messenger signaling components, from kinases to cyclases and phosphodiesterases (Brown et al., 2020; Pace et al., 2020).

The roles of second messenger kinases—collectively referred to as AGC kinases for the founding members protein kinases A, G, and C—in apicomplexan life cycles have been elaborated in candidate-by-candidate approaches. cGMP-dependent protein kinase (or protein kinase G, PKG) is necessary for the secretion of parasite-specific adhesins and perforins enabling efficient escape and invasion of host

cells (Brown et al., 2017, 2016; Wiersma et al., 2004). In apicomplexan cells, PKG operates upstream of calcium release and thus potentiates an orthogonal second messenger signaling network. Consequently, PKG inhibitors have been pursued as anti-parasitic compounds (Baker et al., 2017; Donald et al., 2006; Sidik et al., 2016b). Another cyclic nucleotide-dependent protein kinase, PKA, similarly promotes parasite spread during infection; in *Plasmodium* spp. merozoites, PKA function enables parasite invasion of host cells (Flueck et al., 2019; Patel et al., 2019; Wilde et al., 2019), and in *T. gondii* balanced PKA C1 function is required to ensure that parasites do not exit the host cell prematurely (Jia et al., 2017; Uboldi et al., 2018). *T. gondii* has an additional ortholog of the PKA catalytic subunit, PKA C3, which maintains parasites in the acute phase of the infection and reduces conversion to a slowly proliferating, chronic infection termed the bradyzoite stage (Sugi et al., 2016).

Several recent studies have sought to characterize the downstream targets of second messenger kinases in apicomplexans, including PKA, PKG, and calcium-dependent protein kinases (Alam et al., 2015; Balestra et al., 2021; Brochet et al., 2014; Chan et al., 2023; Herneisen et al., 2022; Jia et al., 2017; Nofal et al., 2022). The second messenger networks in these parasites are intricately interwoven, with documented crosstalk between parasite cAMP, cGMP, and calcium signaling cascades. Comparatively little work has addressed upstream signal integration in apicomplexans. In metazoans, growth factor kinases such as mammalian target of rapamycin (mTOR) and phosphoinositide-dependent protein kinase 1 (PDK1) prime numerous AGC kinases for further second messenger-based activation (Laplante and Sabatini, 2012; Mora et al., 2004).

We recently identified the *S*tore *P*otentiating/*A*ctivating *R*egulatory *K*inase (SPARK), an apicomplexan ortholog of metazoan PDK1, as a fitness-conferring candidate in pooled screens of the *T. gondii* kinome. Parasites depleted of SPARK for multiple replication cycles failed to enter and exit host cells upon stimulation with zaprinast, a chemical that elevates cGMP in parasites (Smith et al., 2022). In a concurrent study, chemical mutagenesis implicated the *Plasmodium falciparum* ortholog of SPARK in invasion and proliferation through the regulation of the PKA pathway (Hitz et al., 2021). Although parasites with disrupted SPARK alleles were characterized phenotypically, evidence for the PDK1 activity of SPARK was indirect. Here, we map the topology of the signaling network regulated by SPARK in *T. gondii*. SPARK complexes with an elongin-like protein we name SPARKEL. Phenotypic and proteomic experiments show that SPARK dysregulation lessens PKA C1, PKG, and PKA C3 function. Phenotypes attributed to SPARK depletion—reduced invasion, host cell lysis, calcium signaling, and elevated differentiation—can be explained by the attenuated activities of SPARK's client kinases. The proper functioning of SPARK thus ensures that *T. gondii* progresses through the acute stage of its infection cycle.

RESULTS

SPARK complexes with an elongin-like protein, SPARKEL

To identify proteins interacting with SPARK, we immunopurified the mNG epitope of the previously described SPARK-mNG-AID strain (Smith et al., 2022) with anti-mNG nanobodies and quantified protein abundance using label-free quantitative proteomics (**Figure 1—figure supplement 1** and **Supplementary File 1**). The immunoprecipitation (IP) successfully enriched SPARK as well as a

hypothetical protein, TGGT1_291010. IPs with lysates of parasites expressing SPARK-mNG lacking AID demonstrated that the interaction was not due to the presence of the degron; TGGT1_291010 was once again highly enriched (**Figure 1A**), along with a putative AGC kinase (TGGT1_205550). The AGC kinase is restricted to coccidians but is dispensable during acute *T. gondii* infection (Sidik et al., 2016a); we therefore focused our efforts on the hypothetical protein, which contributes to parasite fitness.

TGGT1_291010 is a 23 kDa protein with a C-terminal SKP1/BTB/POZ domain (**Figure 1B**). This domain shares homology with that seen in metazoan Elongin C. For this reason, we named the gene TGGT1_291010 "SPARK Elongin-Like protein" (SPARKEL, **Table 1**). SPARKEL homologs are found in the free-living alveolates *Vitrella brassicaformis* and *Chromera velia* but are absent in Aconoidasida (**Figure 1C**), suggesting that the gene was present in the ancestor of apicomplexans but was selectively lost in some lineages.

Immunoprecipitation and mass spectrometry of SPARKEL enriched SPARK (**Figure 1D** and **Supplementary File 1**) and several putative components of daughter cell replication, including TGGT1_212770 (Dos Santos Pacheco et al., 2021), BCC10, and EFPP/BCC5. To confirm that SPARKEL and SPARK interact *in situ*, we introduced a C-terminal TurboID fusion at the SPARKEL endogenous locus (Branon et al., 2018). These transgenic parasites were treated with biotin while intracellular, and biotinylated proteins were enriched from lysates via streptavidin precipitation. As a control, we conducted a parallel experiment with transgenic parasites expressing TurboID fused to a cytosolic mNG fluorophore. SPARK and the AGC kinase TGGT1_205550 were highly enriched in the SPARKEL proximity-labeling experiment (**Figure 1E** and **Supplementary File 2**). A proximity labeling experiment with parasites expressing TurboID at the N terminus of SPARKEL similarly enriched SPARK and TGGT1_205550 (**Figure 1—figure supplement 1** and **Supplementary File 2**). Thus, the interactions between SPARK, SPARKEL, and TGGT1_205550 were consistently observed across a variety of approaches.

Endogenous tagging of SPARK and SPARKEL in the same parasite strain revealed punctate cytosolic staining for each protein (**Figure 1F**); however, the low expression level of SPARKEL precluded robust colocalization. Nevertheless, strong mass spectrometry evidence for the physical interaction between SPARK and SPARKEL motivated further analysis of their functional relationship.

SPARK and SPARKEL depletion phenocopies at multiple steps in the lytic cycle

To determine the regulatory interaction between SPARK and SPARKEL, we first generated a SPARKEL conditional knockdown allele by inserting V5, HaloTag, mini auxin-inducible degron (mAID), and Ty epitopes at the endogenous SPARKEL C terminus. In this strain, we tagged SPARK with a C-terminal V5-mCherry-HA. Parasites treated with IAA to deplete SPARKEL failed to form plaques in host cell monolayers (**Figure 2A**). As indicated by immunoblot, IAA treatment led to a reduction in detectable SPARKEL signal within one hour, as well as co-depletion of SPARK on a similar time scale (**Figure 2B**). We next generated a strain expressing SPARK-V5-mAID-HA. Similarly, SPARK levels were reduced within one hour of IAA addition (**Figure 2—figure supplement 1**), as reported for a similar strain previously (Smith et al., 2022). In this genetic background, we tagged SPARKEL endogenously with a C-

terminal V5-mNG-Ty. IAA treatment reduced SPARK levels and led to a reduction in SPARKEL abundance (**Figure 2C** and **Figure 2—figure supplement 1**). Together, these results suggest that the AID system leads to co-depletion of SPARK and SPARKEL.

To assess the impact of complex knockdown on parasite replication and transitions between intracellular and extracellular environments, we treated SPARKEL-AID and SPARK-AID parasites with IAA and performed replication, invasion, and egress assays. SPARKEL-AID parasites exhibited normal replication kinetics after 24h of IAA treatment (**Figure 2D**). Invasion and egress efficiency of the AID-tagged strains were reduced after parasites were treated with IAA for 24 hours (**Figure 2E** and **2F**), as previously reported for SPARK (Smith et al., 2022). Intracellular calcium measurements of GCaMP-expressing parasites revealed a similar trend, with SPARKEL- and SPARK-depleted cells exhibiting reduced calcium mobilization after 24 hours of IAA and treatment when stimulated with zaprinast, a compound that stimulates calcium release from parasite intracellular stores (Brown et al., 2016; Sidik et al., 2016b) (**Figure 2G, 2H,** and **Figure 2—figure supplement 1**).

SPARK was previously identified in a genetic screen that distinguished acute and delayed death phenotypes in a pooled population of parasites (Smith et al., 2022). As parasites with conditional SPARK alleles were assessed only in the context of delayed death phenotypes—*i.e.* after several replication cycles with IAA treatment—we characterized the ability of SPARK- and SPARKEL-AID parasites to invade and egress after 3 hours of IAA, which is shorter than the *T. gondii* cell cycle. In marked contrast to the 24 hour treatment regime, SPARKEL- and SPARK-AID parasites exhibited no deficiencies in their ability to invade, egress, or mobilize calcium after 3 hours of depletion (**Figure 2E–J**). Thus, in all measured assays, mutants lacking SPARK and SPARKEL are phenotypically identical, likely due to reciprocal co-depletion, but such phenotypes develop over time.

SPARK and SPARKEL depletion leads to AGC kinase down-regulation and up-regulation of bradyzoite-stage proteins

Having verified the interaction between SPARK and SPARKEL, we next investigated pathways regulated by the complex. Initially, we performed a quantitative proteomics experiment following 24 hours of SPARK depletion—the previously described depletion window (Smith et al., 2022). Extended SPARK depletion led to down-regulation of PKG and both the catalytic and regulatory subunits of PKA (**Figure 3A** and **Table 1**). We also observed up-regulation of bradyzoite-specific genes upon SPARK depletion (**Figure 3A** and **Table 1**), including MAG1, BRP1, TGME49_208740, CST1, CST10, MIC13, and BFD2.

To determine the critical window of SPARK and SPARKEL function, we performed quantitative proteomics with tandem mass tag multiplexing that included samples with 0, 3, 8, and 24 hours of SPARK or SPARKEL depletion. The experiments included internal TIR1 parental strain controls to account for basal downregulation arising from the degron (**Figure 3B**). We detected 3,333 and 3,880 proteins with quantification values in the SPARK and SPARKEL depletion time courses, respectively (**Supplementary File 3**). PKA C1, PKA R, and PKG protein abundances only began to drop after 8 hours of IAA treatment (**Figure 3C**). Globally, these kinase subunits were the most down-regulated proteins

following 24 hours of either SPARK or SPARKEL depletion (**Figure 3—figure supplement 1**). Bradyzoite proteins up-regulated upon SPARK depletion primarily increased between 8 and 24 hours of IAA treatment (**Figure 3D**); the same proteins were initially down-regulated in SPARKEL-AID parasites relative to the parental strain and increased most in abundance before 24 hours of IAA treatment (**Figure 3D**). Thus, depletion of the SPARK-SPARKEL complex consistently leads to up-regulation of proteins associated with the bradyzoite stage of development, as well as down-regulation of PKG and the PKA C1 complex.

A depletion phosphoproteome implicates SPARK in the signaling, gene regulation, and metabolic states of the lytic cycle

To determine SPARK-dependent phosphoregulation, we enriched and analyzed phosphopeptides from the depletion proteome. We identified 18,518 phosphopeptides with quantification values, of which 8,867 were quantified with more than one peptide sequence match (PSM). Principal component analysis (PCA) separated the SPARK-AID samples treated for 24 h with IAA from all other samples, while closely clustering biological replicates (**Figure 3—figure supplement 1**). Despite the low abundance of SPARK and SPARKEL, individual phosphopeptides were detected for each protein. Likely due to basal degradation, the abundance of the SPARK peptide was ten-fold lower in SPARK-AID samples compared to the TIR1 control such that further depletion could not be measured (**Figure 3—figure supplement 1**). The SPARKEL peptide abundance was also reduced relative to the TIR1 control sample; however, it decreased further between 3 and 8 hours of IAA treatment (**Figure 3—figure supplement 1**). Because no other SPARKEL peptides were detected, it is not possible to determine whether this decrease is phosphosite-specific or due to a general decrease in SPARKEL protein abundance.

SPARK-regulated phosphopeptides may manifest in a strain-dependent or IAA-dependent manner. To account for basal downregulation, we ranked peptides by their $\log_2$-ratios of altered abundances in the SPARK-AID strain relative to the TIR1 parental strain (**Figure 3E**). When a cutoff of 3.5 modified Z-scores was used, 91 peptides (44 with >1 PSMs) and 69 peptides (19 with >1 PSMs) were down- or up-regulated, respectively. The aforementioned phosphosite belonging to SPARK was the most down-regulated peptide by this metric. A phosphatidylinositol 3- and 4-kinase (PI3,4K) was also strongly down-regulated (**Table 1**); however, the protein abundance of this enzyme was not quantified. To identify peptides most altered by IAA treatment, and hence SPARK depletion, we summed and ranked peptides by $\log_2$-ratios of abundances in the SPARK-AID strain relative to the untreated samples (**Figure 3F**). By this metric, 138 peptides (51 with >1 PSMs) and 93 peptides (36 with >1 PSMs) were down- or up-regulated by more than 3.5 modified Z-scores, respectively. Phosphoproteins belonging to this category are discussed in greater depth below.

To uncover the molecular pathways regulated by SPARK, we performed enrichment analysis of the peptides exhibiting the highest degree of altered abundance upon SPARK depletion (**Figure 3G**). Changes in SPARK function altered PTM cascades both directly and indirectly. SPARK depletion reduced the abundance of phosphopeptides belonging to cyclic nucleotide-regulated kinases, which was in part driven by a reduction in kinase abundance. SPARK depletion also coincided with a reduction

206 in phosphosites on several phosphatases (**Table 1**), including BCC6, PPM1, and an uncharacterized
207 dual-specificity phosphatase. By contrast, phosphorylation of other kinases and phosphatases
208 increased upon SPARK depletion, which may arise as an indirect consequence of SPARK function.
209 Upregulated phosphosites were found on pyruvate dehydrogenase and STE kinase, CDPK3, cyclin2-
210 related protein, and the kinases TGGT1_204280 and TGGT1_239885; as well as the protein
211 phosphatases PPM2B, calcineurin, and EFPP. Phosphosites belonging to proteins involved in ubiquitin
212 transfer and hydrolysis also increased in abundance upon SPARK depletion. Examples of this class
213 included UBP1, USP39, an RBR E3 ligase, CCR4-NOT subunit, and UBR box E3 ligase. To a lesser
214 degree, phosphosites on ubiquitin ligases were also down-regulated following SPARK depletion—for
215 example, a HECT E3 and putative E2 enzyme. Thus, SPARK function has large implications for PTM
216 cascades.
217
218 Additional functional categories enriched for SPARK-dependent regulation included nucleic acid–
219 binding proteins (**Figure 3G** and **Table 1**). A number of down-regulated phosphosites belong to proteins
220 involved in DNA accessibility and transcription—for example, TFIIS, SET1, NOC3p, and *Tg*SRCAP. RNA
221 modification enzymes also exhibited phosphoregulation, such as two PUS proteins, PRP8, SLU7, a FHA
222 protein, three KH proteins, and a DCP2 homolog. Other regulated phosphoproteins may function in
223 mRNA cap or untranslated region (UTR) binding, such as *Tg*PUF1, a MIF4G protein, CBP80, eIF3, and
224 GCN1. Some of these proteins have been linked to expression changes during stage conversion, with
225 PUF1 and SRCAP levels having been noted to increase during stress (Joyce et al., 2013; Liu et al., 2014;
226 Sullivan et al., 2003). Moreover, CBP80, eIF3, and the KH protein TGGT1_216670 co-purified with the
227 Alba complex (Gissot et al., 2013), which is necessary for bradyzoite differentiation. Regulation of these
228 proteins thus may be linked to the elevated expression of bradyzoite-stage proteins upon SPARK
229 depletion.
230
231 Several putative transporters also exhibited decreased phospho-abundance upon SPARK knockdown
232 (**Figure 3G**). Some of these phosphoproteins channel inorganic cations, such as *Tg*ZnT (Chasen et al.,
233 2019). Others likely transport small organic molecules—for example, a nucleoside and two ABC
234 transporters. In aggregate, these analyses implicate SPARK function in signaling, gene regulation, and
235 metabolic exchange.
236
237 **Clustering of phosphopeptide kinetics identifies seven response signatures**
238 Mammalian PDK1 phosphorylates numerous AGC kinases at activation loop threonines (Mora et al.,
239 2004; Pearce et al., 2010), as well as non-kinase substrates. We reasoned that SPARK-dependent
240 phosphopeptides depleted within 3 hours of IAA treatment may represent sites constitutively regulated
241 by the kinase. By contrast, phosphosites down-regulated only after 8 hours of SPARK depletion—in
242 excess of the length of the *T. gondii* cell cycle—may represent newly synthesized proteins dependent on
243 SPARK for activation. We sought to resolve the phosphoproteome into kinetically distinct clusters.
244 Gaussian mixture-model algorithms heuristically clustered peptides identified by more than one PSM
245 into seven classes on the basis of their response signatures following SPARK depletion (**Figure 3H**). Two
246 phosphopeptides in Cluster 1 were distinguished by their rapid and sustained depletion kinetics and
247 corresponded to CBP80 and eIF3, both of which function in mRNA and translational regulation. The

248 second cluster of phosphopeptides was largely down-regulated by 3 hours of IAA treatment and lacked
249 dynamics following this window. PKA and PKG phosphopeptides belonged to Cluster 3, which
250 decreased only after 8 hours of IAA treatment. The final cluster of depleted phosphopeptides, Cluster 4,
251 only exhibits down-regulation at 8h of IAA treatment and may reflect phosphoregulation specific to the
252 cell cycle.
253
254 Up-regulated phosphopeptides mirrored the dynamics of the down-regulated clusters. Cluster 5
255 phosphopeptides were elevated within 3 hours of IAA treatment and continued to increase thereafter.
256 Cluster 6 was up-regulated by 3 hours of IAA treatment and lacked dynamics following this window.
257 Cluster 7 increased gradually and predominantly after 8 hours of IAA treatment. Upregulated
258 phosphosites may arise from a number of mechanisms following SPARK depletion. For example,
259 SPARK activity may inhibit downstream kinases or activate downstream phosphatases; sterically block
260 access of serines/threonines to other enzymes; or give rise to crosstalk between PTMs. Approaches that
261 take into account subcellular proximity were required to distinguish direct substrates from pathways
262 downstream of SPARK function.
263
264 **Proximity labeling identifies putative SPARK targets *in situ***
265 To gain insight into proximal SPARK interactors in intracellular parasites, we tagged the endogenous C
266 terminus of SPARK with a TurboID domain and carried out proximity labeling experiments, as
267 previously described for SPARKEL. We observed overlap in the phosphoproteomics and proximity
268 labeling experiments. PKG was enriched (**Figure 3I**), while PKA C1 and PI4P5K only narrowly missed our
269 cutoffs. A putative HECT E3 ubiquitin ligase with two phosphosites down-regulated in the SPARK-
270 dependent phosphoproteome was a candidate interactor. We also detected enrichment of PKA C3.
271 PKA C3 is a coccidian-specific ortholog of the apicomplexan PKA catalytic subunit (Sugi et al., 2016);
272 however, no PKA C3 peptides were quantified in our depletion phosphoproteome experiments, likely
273 due to the low abundance of the protein. These integrated proteomics approaches hint that the
274 phenotypes associated with SPARK depletion may arise from the altered activity of AGC kinases
275 regulated by SPARK.
276
277 **SPARK functionally interacts with PKA and PKG**
278 Our proteomic data suggest SPARK controls the lytic cycle via activation of PKA C1 and PKG. SPARK
279 depletion reduced levels of PKA C1 T190—which corresponds to the kinase activation loop—more
280 rapidly than the corresponding protein levels (**Figure 4A**). Similarly, SPARK depletion triggered the
281 down-regulation of several phosphosites residing in the N terminus of PKA R (e.g. S17, S27, and S94)
282 more robustly than the changes in protein levels (**Figure 4B**). To confirm the depletion kinetics of PKA,
283 we tagged the kinase subunits with fluorophores in the SPARK-AID parasite strain (**Figure 4C**).
284 Prolonged SPARK depletion (24 hours) reduced PKA C1 and PKA R immunofluorescence signals in
285 intracellular parasites (**Figure 4D**). To monitor kinase levels kinetically, we performed flow cytometry at
286 several time points following the addition of IAA (**Figure 4E**). PKA C1 and PKA R fluorophore intensity
287 decreased predominantly after 8 hours of IAA treatment, consistent with proteomic results. In parallel
288 experiments, we tagged PKA C1 and PKA R in the SPARKEL-AID strain, revealing a comparable loss of
289 the two markers following SPARKEL depletion (**Figure 4F**).

290
291 We considered the possibility that the SPARK depletion phosphoproteome represents a convolution of
292 phosphoproteomes arising from broader AGC kinase down-regulation. We systematically tested this
293 possibility by generating phosphoproteomes of parasites depleted of PKA R and PKG (**Supplementary**
294 **File 4**). As association with PKA R inhibits PKA C1 activity (Jia et al., 2017), we reasoned that
295 phosphosites up-regulated after a short window of PKA R depletion represent candidate PKA C1
296 targets. Similarly, phosphosites down-regulated after PKG depletion represent candidate PKG
297 substrates (Brown et al., 2017). Peptides above two modified Z-scores were considered candidate
298 targets of each kinase.
299
300 Compared to the bulk phosphoproteome, the PKA C1-dependent phosphopeptides significantly
301 decreased in abundance between 8 and 24 hours of SPARK depletion (**Figure 4G**). When we applied the
302 same analysis to a similarly acquired PP1-dependent phosphoproteome (Herneisen et al., 2022), we
303 found no significant relationship to the SPARK phosphoproteome (**Figure 4–figure supplement 1**),
304 suggesting that the association with PKA C1 is specific. Several of the overlapping SPARK and PKA C1–
305 dependent phosphoproteins localized to the parasite periphery and apex (**Figure 4H**), for example,
306 IMC25, AC13, CIP1, CIP2, and AC3. Others are putatively involved in RNA-binding functions, such as
307 eIF4E and two KH proteins, including a component of the METTL3/METTL14 core (Farhat et al., 2021).
308 We also observed regulation of phosphoproteins involved in ubiquitin transfer, including the
309 aforementioned E2 and HECT E3 proteins (**Table 1**). Regulation of these proteins may account for both
310 the kinetic- and replicative-phase phenotypes attributed to perturbed PKA C1 activity (Jia et al., 2017;
311 Uboldi et al., 2018).
312
313 We carried out related experiments to validate that SPARK regulates PKG function. SPARK depletion
314 reduced levels of several PKG phosphopeptides more rapidly than the corresponding protein levels
315 (**Figure 5A**). Notably, T838 corresponds to the PKG activation loop. Attempts to tag PKG with a
316 fluorophore in a functional SPARK-AID background were unsuccessful. Global genetic screens have
317 indicated that parasites with hypomorphic PKG—as can arise through endogenous tagging—are rapidly
318 outcompeted by wildtype parasites (Fang et al., 2018; Smith et al., 2022). Therefore, we instead relied
319 on chemical-genetic interactions to validate the relationship between PKG and SPARK. We reasoned
320 that parasites with down-regulated PKG activity might be sensitized to the specific PKG inhibitor
321 Compound 1 (Donald et al., 2002). Previous studies had shown that SPARK was dispensable for A23187-
322 induced egress (Smith et al., 2022); however, PKG function is required for ionophore-induced egress
323 (Brown et al., 2017; Lourido et al., 2012). We performed egress assays using parasites depleted of
324 SPARK for 24 hours and treated with different concentrations of Compound 1. As anticipated, SPARK
325 depletion sensitized parasites to A23187-induced egress inhibition with Compound 1 (**Figure 5B–C**),
326 suggesting that PKG activity is decreased in the absence of SPARK.
327
328 As with PKA, we quantified the behavior of putative PKG substrates in the SPARK-AID
329 phosphoproteome. Compared to the bulk phosphoproteome, the PKG-dependent phosphopeptides
330 significantly decreased in abundance between 8 and 24 hours of SPARK depletion (**Figure 5D**). Several
331 overlapping SPARK and PKG-dependent phosphoproteins localized to the parasite periphery, including

332 an MFS transporter, *Tg*A1, MyoG, IMC18, IMC28, and IMC41. Other PKG/SPARK-dependent sites were
333 found in the apical proteins AAP3, AC5/TLAP3, AC13, and SPM1; while several other proteins localized
334 to the ER, including two TB2/DP1, HVA22 family proteins, a TPR protein, and an ABC transporter
335 (**Figure 5E**). Others function in the secretory or protein trafficking pathways, such as Sec7, COG6,
336 *Tg*TBC10, and *Tg*DHHC1. We also observed down-regulation of phosphosites belonging to proteins
337 involved in ubiquitin transfer, such as an E2 enzyme and a ubiquitin family protein with a C-terminal
338 extension. The precise pathways regulated by *Tg*PKG remain to be defined; however, recent studies
339 triggering PKG activity in *T. gondii* (Chan et al., 2023; Herneisen et al., 2022) or related *Plasmodium spp.*
340 (Alam et al., 2015; Balestra et al., 2021; Brochet et al., 2014) suggested that PKG substrates relevant for
341 egress reside at the parasite periphery and ER, as observed for the overlapping PKG and SPARK targets
342 here.
343
344 **Depletion of SPARK, SPARKEL, or PKA C3 promotes chronic differentiation**
345 Several pieces of evidence suggested that SPARK and SPARKEL depletion may prompt differentiation
346 from the tachyzoite to bradyzoite state through dysregulation of another AGC kinase, PKA C3. First,
347 down-regulation of SPARK and SPARKEL coincided with up-regulation of bradyzoite markers (**Figure**
348 **3A** and **3D**). Second, SPARK proximity labeling resulted in enrichment of PKA C3 (**Figure 3I**)—a
349 negative regulator of the bradyzoite stage (Sugi et al., 2016) and, to date, the only AGC kinase
350 characterized with a function in differentiation (Augusto et al., 2020). Prolonged SPARK and SPARKEL
351 depletion indeed elevated differentiation under normal culture conditions, as measured by staining of
352 the cyst walls with dolichos binding lectin, a characteristic of chronic-stage bradyzoite vacuoles (**Figure**
353 **6A–B**). N-terminal tagging of SPARKEL with AID similarly elevated differentiation upon IAA treatment
354 (**Figure 6–figure supplement 1**). Alkaline media in combination with serum starvation and low carbon
355 dioxide is commonly used to elevate bradyzoite transformation in cell culture, and SPARK and
356 SPARKEL down-regulation enhanced differentiation under such conditions (**Figure 6A** and **6B**).
357
358 To dissect the hypothesized PKA C3–dependent arm of SPARK regulation, we altered the PKA C3
359 genomic locus with a V5-mAID-mNG-Ty tagging payload. Addition of auxin to the culture medium
360 resulted in down-regulation of PKA C3 levels to below the detection limit within one hour (**Figure 6C–**
361 **D**). PKA C3 exhibited low expression levels in cytoplasmic puncta (**Figure 6C**), as previously reported
362 (Sugi et al., 2016). We confirmed that prolonged PKA C3 depletion led to elevated differentiation rates
363 under normal and alkaline-stress culture conditions (**Figure 6A–B**) and observed that the effect was
364 similar to SPARK or SPARKEL knock-down. Given that SPARK also regulates PKG and PKA C1, we
365 considered the possibility that differentiation may be linked to a block in motility. However, the
366 inability to egress is not sufficient for transformation, as conditional knockdown of PKG or CDPK1
367 (Brown et al., 2017; Chan et al., 2023; Shortt et al., 2022) failed to significantly enhance the frequency of
368 differentiation markers (**Figure 6A–B**). We did not assess differentiation in PKA C1 knockdown
369 parasites, as these mutants spontaneously egress from host cells (Jia et al., 2017; Uboldi et al., 2018).
370
371 The RH strain in which we generated mutants is reported to be refractory to differentiation into the
372 bradyzoite form (Dubey et al., 1999), like due to defects downstream of the pathways that lead to the
373 initial synthesis of the cyst wall. We generated SPARKEL- and PKA C3-AID strains in the ME49

374 background (**Figure 6–figure supplement 1**), which readily undergoes differentiation in tissue culture
375 and mice, and confirmed that depletion prompts spontaneous differentiation in tissue culture (**Figure**
376 **6E–F**). We did not assess alkaline-induced differentiation, as this stress treatment results in near-
377 complete differentiation in the ME49 strain (Waldman et al., 2020), and thus does not provide a
378 differential for mutants that enhance differentiation.
379
380 To assess whether differentiation in the RH-type strain is dependent on the master regulator of
381 differentiation, BFD1 (Waldman et al., 2020), we knocked out *BFD1* CDS with a sortable dTomato
382 cassette in the SPARK- and PKA C3-AID strains (**Figure 6–figure supplement 1**). The resulting Δ*bfd1*
383 mutants failed to undergo differentiation as measured by cyst wall staining (**Figure 6G–H**). We
384 additionally profiled transcriptomic remodeling in PKA C3-AID parasites that had been depleted of the
385 kinase for 24 hours and compared these changes to the chronic-stage transcriptome of parasites
386 overexpressing BFD1 (**Figure 6I** and (Waldman et al., 2020)). We observed up-regulation of several
387 chronic-stage proteins upon PKA C3 depletion, including the bradyzoite antigen BAG1, CST1, CST10,
388 MIC13; and *Tg*SPT2, which functions in ceramide synthesis and was recently reported to exhibit BFD2-
389 dependent abundance (Licon et al., 2023). PKA C3 mRNA abundance was down-regulated, suggesting
390 that the tagging payload may alter steady-state transcript levels. Together, these results suggest that
391 the bradyzoite stage conversion induced by knockdown of PKA C3 and SPARK proceeds through the
392 canonical transcriptional pathway.
393
394 **PKA C3 interacts with the SPARK complex**
395 Several AGC kinases, including PKA C3, share the activation loop motif TLC/VGTxxY, which displayed
396 SPARK-dependent phosphorylation in PKA C1 and PKG. PKA C3 was not detected in our SPARK
397 depletion proteomics experiments (**Figure 3**). To determine whether SPARK and PKA C3 interact, we
398 immunopurified PKA C3 lysates, using the mNG epitope as a handle. The immunoprecipitated PKA C3
399 was highly enriched for SPARK (**Figure 7A**), and to a lesser extent other protein kinases, including
400 TGGT1_205550, SRPK, and AMPK subunit beta. The latter has recently been characterized as a
401 safeguard of parasite cell cycle regulation that enhances differentiation when knocked out (Yang et al.,
402 2022). To a lesser extent, SPARKEL also significantly co-purified with PKA C3 (**Supplementary File 1**).
403 Our results are consistent with other reports that PKA C3 does not interact with the canonical PKA
404 regulatory subunit in *T. gondii (Jia et al., 2017; Uboldi et al., 2018)* and, in conjunction with TurboID data
405 presented in **Figure 3I**, provide support for a strong physical interaction between SPARK and PKA C3.
406
407 **SPARK down-regulation does not reduce PKA C3 protein levels**
408 To determine whether SPARK activity affects PKA C3 abundance, as for PKA C1 and PKG, we tagged
409 the endogenous PKA C3 C terminus with an mNG fluorophore in the SPARK-AID background. After 24
410 hours of IAA treatment, PKA C3 levels were unaltered or slightly elevated, as measured by immunoblot
411 (**Figure 7B–C**). Immunofluorescence and flow cytometry measuring mNG intensity after 0, 3, 8, and 24
412 hours of IAA treatment revealed a trend towards increasing PKA C3 abundance, although this
413 difference was not significant (**Figure 7D–F**). Thus, unlike PKA C1, PKA C3 does not exhibit down-
414 regulation following SPARK depletion. We considered the possibility that SPARK function could instead
415 alter PKA C3 activity levels.

416
417 **The PKA C3 phosphoproteome identifies candidates regulating the transition to the bradyzoite**
418 **state**
419 To pursue the functional consequences of PKA C3 inhibition, we performed a depletion
420 phosphoproteomics time course experiment with the PKA C3-AID strain following 1, 3, 8, and 24 hours
421 of IAA treatment. PKA C3-dependent phosphopeptides were identified as for the SPARK depletion
422 proteome (**Figure 7G**). The resulting proteome identified 4,792 proteins and 12,721 phosphopeptides,
423 of which 9,576 were quantified with more than one PSM. PCA separated the 24 hour IAA samples from
424 all others (**Figure 7–figure supplement 1**). Similar to the SPARK depletion proteome, several of the up-
425 regulated proteins were reported to be transcriptional signatures of the bradyzoite stage, including
426 BRP1, TGGT1_208740, two secreted cAMP-dependent protein kinases, and BFD2 (**Figure 7–figure**
427 **supplement 1**).
428
429 To identify peptides most altered by IAA treatment, we summed and ranked peptides by $\log_2$-ratios of
430 abundances in the PKA C3-AID strain relative to the untreated (0 h) samples (**Figure 7G**). By this metric,
431 129 peptides (94 with >1 PSMs) and 49 peptides (31 with >1 PSMs) were down- or up-regulated by more
432 than 3.5 in the modified Z-scores, respectively. Gaussian mixture-model algorithms heuristically
433 clustered peptides identified by more than one PSM into three classes (**Figure 7H**). Cluster 1 contained
434 12 peptides that rapidly decreased within 1–3 hours of PKA C3 depletion, and continued to decrease
435 thereafter. This cluster includes CBP80, a DEP domain protein, *Tg*ZnT, *Tg*ApiAT3-1, AC13, and FtsH1
436 (**Table 1**).
437
438 Cluster 2 comprised 82 peptides that also decreased within 1–3 hours of IAA treatment, after which
439 their abundances remained stable and decreased overall to a lesser extent than cluster 1 (**Figure 7H**).
440 Cluster 2 included genes putatively involved in gene regulation, including eIF4G1, NOC3p, a zinc finger
441 protein, a DNA repair protein, SET1, and a nucleotidyltransferase (**Table 1**). Several phosphosites
442 belonging to proteins involved in daughter cell biogenesis were also down-regulated, including AC13,
443 IAP2, BCC8, and condensin 2. We also observed down-regulation of transporters belonging to this
444 cluster–for example, TgApiAT2, ATP4, and a nucleoside transporter. The early events in bradyzoite
445 differentiation have not been extensively characterized but involve translational regulation of BFD1
446 enhanced by a BFD1/BFD2 feed-forward loop (Licon et al., 2023; Waldman et al., 2020). Down-
447 regulation of PKA C3 may enhance conditions that activate this loop, for example due to global down-
448 regulation of cap-dependent translation (CBP80, eIF4G1) or alteration of the replicative cycle (Radke et
449 al., 2003).
450
451 Cluster 2 also contains numerous proteins trafficking through secretory organelles, including the
452 micronemes, rhoptries, and dense granules. Modified phosphosites belonging to micronemal proteins
453 included CRMP-b, TGGT1_221180, and TGGT1_304490 (**Table 1**). The rhoptry proteins ROP1, ROP13,
454 ROP17, ROP40, and RON9 were also differentially regulated. Modified dense granule/parasitophorous
455 vacuole proteins included GRA3, GRA4, GRA6, GRA7, GRA8, GRA31, GRA57, GRA62, GRA70, SFP1, and
456 MAG1. Many of these proteins are lumenal within their respective organelles, and regulation by PKA C3
457 is therefore likely indirect. Nonetheless, each of the secretory organelles contain stage-specific

458 subproteomes with implications for metabolism and protein complex assembly in bradyzoites (Sinai et
459 al., 2020); the regulation observed here may reflect such early stages of proteomic remodeling.
460
461 The 31 phosphopeptides belonging to cluster 3 increased in abundance following PKA C3 depletion and
462 therefore are likely indirect targets of the kinase. This cluster contained phosphoproteins involved in
463 gene regulation (**Table 1**), such as AP2XII-9, an ISWI protein, CAF1, PLU-1, GCFC, and two zinc finger
464 proteins: TGGT1_223880 and BFD2. We also identified several candidates involved in proteostasis,
465 including HSP90, p23, CSN3, PSME4. Regulation of such proteins may be related to the transition and
466 maintenance of the bradyzoite state, albeit not as a direct consequence of PKA activity.
467
468 The protein phosphatase PP2A has recently been characterized as a regulator of bradyzoite
469 differentiation (Wang et al., 2022). We therefore analyzed proteins that exhibited both PKA C3- and
470 PP2A-dependent phosphoregulation. Several candidates in this category were identified as
471 differentially important in interferon-stimulated cells, including TGGT1_209500, GRA57, and GRA70.
472 Numerous phosphosites belonging to AC13 were differentially regulated in both phosphoproteomes.
473 Some proteins involved in endo- and exocytosis also exhibited dynamic phosphoregulation, including
474 CRMP-b and Kelch13. PKA R S^{27} was up-regulated upon PKA C3 depletion and was also up-regulated in
475 *Δpp2a* mutants. Finally, nucleic acid-binding proteins exhibited differential phosphoregulation,
476 including BFD2, a KH protein, eIF4G2, and AP2XII-1. Given the stage conversion phenotypes of
477 parasites lacking PKA C3 or PP2A, the phosphoregulation of overlapping targets may be functionally
478 important in the context of bradyzoite differentiation.
479
480 **The SPARK phosphoproteome shares signatures with the PKA C3–depletion phosphoproteome**
481 We anecdotally observed overlap between SPARK- and PKA C3-dependent phosphopeptides, and in
482 particular those with putative nucleic acid binding functions. We therefore systematically compared the
483 abundances of candidate PKA C3 targets (as defined above) to overlapping phosphosites in the SPARK
484 phosphoproteome. Compared to the bulk phosphoproteome, the PKA C3–dependent phosphopeptides
485 significantly decreased in abundance within three hours of SPARK depletion (**Figure 7I**). Several of
486 phosphoproteins found to be altered by both PKA C3 and SPARK depletion belonged to proteins
487 involved in gene regulation (**Figure 7J** and **Table 1**), including CBP80, eIF4G2, SET1, NOC3p, Spt5, a KH
488 protein, a nucleotidyltransferase, and PRP4. Some of these proteins associate with large transcription
489 factor assemblies, including the AP2IX4/MORC and GCN5-B complexes. Transporters also overlapped
490 between the two phosphoproteomes, including ZnT, TgApiAT2, and TgApiAT3-1. Several phosphosites
491 belonging to apical cap proteins were also shared between the phosphoproteomes, including numerous
492 AC13 peptides.
493
494 The SPARK and PKA C3 phosphoproteomes notably diverged with regards to regulation of dense
495 granule proteins, which was observed as a subpopulation of PKA C3–dependent peptides that increased
496 in abundance upon SPARK depletion (**Figure 7I** and **7K**). This effect was specific to the indicated
497 phosphopeptides, as corresponding protein levels of the dense granule proteins were not changed
498 (**Supplementary File 4**). The differentially regulated dense granule proteins include many of those
499 belonging to cluster 2 of the PKA C3 depletion proteome (**Figure 7H** and **7K**). The phosphoproteome of

500 SPARK shares signatures of reduced PKA C3 activity; however, due to concomitant down-regulation of
501 other AGC kinases, the phosphoproteomes of SPARK and PKA C3 depletion diverge in ways that
502 remain to be explored.
503
504 ## DISCUSSION
505 PDK1, the closest mammalian homolog to SPARK, is considered a key regulator of AGC kinases (Mora
506 et al., 2004; Pearce et al., 2010). These kinases are united by general structural features required for
507 activity and integrity, such as the activation segment (also known as the activation loop or T-loop), and
508 the C-terminal hydrophobic and turn motifs, which are common loci of regulation that can position the
509 kinase into an active conformation. In mammals, AGC kinases depend on PDK1 in various ways. For
510 example, phosphorylation of the Akt (PKB) activation loop by PDK1 leads to partial activation;
511 additional phosphorylation by the target of rapamycin (mTOR) complex produces maximal activity
512 (Pearce et al., 2010). Some protein kinase C (PKC) isoforms undergo ordered phosphorylation by
513 upstream enzymes—including PDK1—that prime PKC for activity and prevent kinase degradation
514 (Newton, 2010). PKA catalytic isoforms require T-loop phosphorylation for activity; however, whether
515 this modification is installed autocatalytically or by PDK1 depends on the cellular context (Cheng et al.,
516 1998; Moore et al., 2002; Williams et al., 2000). Consequently, PDK1 dysregulation provokes diverse
517 cellular consequences, including enhanced growth, migration, and cell survival—processes associated
518 with cancer in animals (Gagliardi et al., 2018; Mora et al., 2004; Raimondi and Falasca, 2011). In this
519 study, we characterize the diverse consequences of PDK1 dysregulation in the ubiquitous and divergent
520 eukaryotic parasite of such animals, *T. gondii.*
521
522 SPARK down-regulation coincides with reduced PKG and PKA C1 activity due to reduced protein levels.
523 From our own studies, multiple mass spectrometric and cell biological experiments support this
524 observation. Furthermore, PDK1 mutations in the related apicomplexan *Plasmodium falciparum* were
525 observed to act as suppressors of toxicity related to overexpression of *Pf*PKA (Hitz et al., 2021). Both
526 *Tg*PKG and *Tg*PKA C1 possess features of AGC kinases involved in PDK1 interaction, such as the PDK1-
527 interacting fragment FXXF. PKA C1 terminates in the sequence FTSW, whereas PKG has two non-
528 terminal FXXF motifs, FGDF and FLYF. Although these motifs are not strictly C-terminal, as in animals,
529 their position resembles that observed in some plant AGC kinases, up to 50 amino acids upstream of
530 the C-terminus (Rademacher and Offringa, 2012). The T-loop phosphorylation of each kinase—PKA C1
531 T190 and PKG T838—are down-regulated to a greater extent than corresponding protein levels
532 following SPARK knockdown (**Supplementary File 3**). Heterologous expression and activity assays of
533 PKA C1 and PKG may resolve the importance of activation loop phosphorylation for kinase function;
534 however, such biochemical assays are not currently available for the *T. gondii* kinases. The requirement
535 of T-loop threonine for PKG activity is unclear, as recombinant *Plasmodium* spp. PKG was still active
536 when this residue was mutated (Bakkouri et al., 2019). Conformational changes due to cGMP binding—
537 in particular, rearrangement of the N-terminal autoinhibitory segment otherwise adjacent to the
538 activation loop—appeared particularly important for PKG activity. Upon SPARK depletion, multiple
539 phosphorylation sites in the N-terminal and cyclic nucleotide-binding domains of PKG (S20, S22, T59,
540 S62, T96, T99, and S105) similarly decrease in abundance to a greater extent than protein levels, and

may function in the regulation of these domains. The cause for reduction of PKA C1 and PKG levels requires further study; in principle, active degradation or dilution mechanisms due to cell division are possible. In support of the latter, down-regulation of both kinases was only observed after 8 hours of SPARK depletion, a period in excess of the duration of the *T. gondii* cell cycle.

Independent of biochemical mechanisms, genetic evidence supports the hypothesis that SPARK phenotypes associated with kinetic transitions in the lytic cycle—such as motility, egress, and invasion—arise from dysregulated PKA C1 and PKG activity. In *T. gondii*, PKA negatively regulates egress and positively regulates the transition between invasion and the establishment of a replicative niche (Jia et al., 2017; Uboldi et al., 2018); by contrast, in *P. falciparum*, PKA mediates parasite invasion (Flueck et al., 2019; Patel et al., 2019; Wilde et al., 2019). PKG is more broadly required for apicomplexan motility, invasion, and egress and functions by mobilizing parasite intracellular calcium stores. Genetic pathway analysis of *T. gondii* PKA C1 and PKG inhibition supports a model in which PKG lies downstream of PKA (Jia et al., 2017). Increasingly, proteomic, genetic, and physiological studies implicate negative feedback mechanisms between cAMP and cGMP signaling pathways in apicomplexans (Alam et al., 2015; Bisio et al., 2019; Brochet et al., 2014; Moss et al., 2022; Nofal et al., 2022). In *T. gondii*, SPARK inhibition releases the breaks that PKA C1 holds on egress and jams the engine of PKG activity, resulting in parasite stasis. The PKA signaling circuit differs in *Plasmodium* spp., where a sole PKA C subunit is indispensable for invasion but not egress (Patel et al., 2019; Wilde et al., 2019). However, SPARK inhibition would lead to a similarly inhibitory effect on parasite proliferation, as has been suggested recently in studies employing altered *P. falciparum* PDK1 and PKA alleles (Hitz et al., 2021).

T. gondii has two additional paralogs of the PKA catalytic subunit, relative to *Plasmodium* spp., PKA C2 and PKA C3. PKA C2 expression levels are low outside of the parasite sexual stages (Ramakrishnan et al., 2019; Sugi et al., 2016). PKA C3 disruption was previously reported to increase conversion to the bradyzoite stage (Sugi et al., 2016). Our results using a PKA C3 conditional knockdown support this finding. Furthermore, PKA C3 and SPARK associate, as revealed through approaches that probe reciprocal interactions. PKA C3 possesses a canonical PDK1-interacting fragment (FDNF) and shares an activation loop motif with PKA C1. Although PKA C3 peptide levels were below the detection limit in our depletion phosphoproteome experiments, we propose that SPARK depletion leads to down-regulation of PKA C3 activity separately from a reduction in PKA C3 protein abundance. SPARK and PKA C3 depletion phenocopy each other with respect to *in vitro* differentiation. Candidates for the molecular targets responsible for differentiation may reside in the overlapping phosphosites in the SPARK and PKA C3 depletion phosphoproteomes.

The regulation of SPARK remains an open inquiry. Mammalian PDK1 is constitutively active due to auto-phosphorylation in *trans*. The PH domain triggers mammalian PDK1 homodimerization upon binding of phosphatidylinositol (3,4,5)-trisphosphate (Levina et al., 2022; Masters et al., 2010; Pearce et al., 2010). SPARK lacks the PH domain (Smith et al., 2022); therefore, apicomplexans have likely evolved alternative mechanisms for regulating PDK1. The complex of proteins interacting with SPARK—the elongin-like protein SPARKEL and the putative AGC kinase TGME49_205550—may

583 represent a means of modulating SPARK activity. Elongin C forms a component of multiprotein
584 complexes. E3 ubiquitin ligases are well-known examples; however, elongin C can affect steady-state
585 protein levels through mechanisms distinct from ubiquitination (Hyman et al., 2002). In metazoans,
586 PDK1 has been reported to associate with E3 ligases and exhibit monobiquitination (Jiang et al., 2021;
587 Uras et al., 2012). The anti-correlated cell cycle expression profiles of SPARK and SPARKEL suggest a
588 specific window of activity for the complex. However, given the co-depletion of the complex—as has
589 been reported for other tightly associated proteins studied with the AID system (Tosetti et al., 2020)—
590 further biochemical studies are required to discern the regulatory interactions between SPARK and
591 SPARKEL. *Plasmodium* spp. appear to have lost SPARKEL, which is otherwise conserved in the
592 apicomplexans, possibly requiring tight regulation of SPARK expression or other mechanism to control
593 its activity.
594 Our unbiased and integrative proteomic approaches uncovered ancient features of signaling networks
595 *de novo* and revealed how such relationships can be repurposed for parasitism. Apicomplexans are well-
596 adapted to transition between life stages in their hosts. Synthesizing genetic, proteomic, and
597 phenotypic data, we propose that SPARK fundamentally integrates the topology of cyclic nucleotide
598 signaling networks in apicomplexan parasites. In *T. gondii*, proper SPARK function preserves tachyzoite
599 physiology by activating PKG, PKA C1, and PKA C3, thus promoting cycling within the acute stages of
600 the infection in favor of differentiation into the chronic stage wherein AGC kinase activity is lower (Fu et
601 al., 2021). In principle, SPARK may serve as a central node for regulation of the asexual stages.
602
603 ## KEY RESOURCES TABLE

Reagent type (species) or resource	Designation	Source or reference	Identifiers	Additional information
Strain, strain background RH (T. gondii)	RH/TIR1	PMID: 28465425		RH/TIR1/ΔKU80/ΔHXGPRT. Mycoplasma negative.
Strain, strain background RH (T. gondii)	ME49/TIR1	PMID: 37081202		ME49/TIR1/ΔKU80/ΔHXGPRT. Mycoplasma negative.
Strain, strain background RH (T. gondii)	RH/TIR1/GCaMP6f	PMID: 35484233		RH/TIR1/pTUB1-GCaMP6f/ΔKU80/ΔHXGPR

				T. Mycoplasma negative.
Strain, strain background RH (T. gondii)	RH/TIR1/GCaMP6f	PMID: 35976251		RH/TIR1/pMIC2-MIC2-GLuc-myc-P2A-GCaMP6f/ΔKU80/ΔHXGPRT. Mycoplasma negative.
Strain, strain background RH (T. gondii)	RH/TIR1/mNG-TurboID	PMID: 36712004		RH/TIR1/mNG-TurboID-Ty/ΔKU80/ΔHXGPRT. Mycoplasma negative.
Strain, strain background RH (T. gondii)	RH/TIR1/PKG-AID	PMID: 28465425	TGGT1_311360	RH/TIR1/ΔKU80/ΔHXGPRT/PKG-mAID-HA/HXGPRT. Mycoplasma negative.
Strain, strain background RH (T. gondii)	RH/TIR1/CDPK1-AID	doi: https://doi.org/10.1101/2022.07.19.500742	TGGT1_301440	RH/TIR1/ΔKU80/ΔHXGPRT/CDPK1-V5-mNeonGreen-mAID-Ty. Mycoplasma negative.

Strain, strain background RH (T. gondii)	SPARK-mNG-AID	PMID: 35484233	TGGT1_268210	RH/TIR1/ΔKU80/ΔHXGPRT/SPARK-V5-mNG-mAID-Ty. Mycoplasma negative.
Strain, strain background RH (T. gondii)	SPARK-mNG	This paper	TGGT1_268210	RH/ΔKU80/ΔHXGPRT/SPARK-V5-mNG-Ty. Mycoplasma negative.
Strain, strain background RH (T. gondii)	SPARKEL-TurboID	This paper	TGGT1_291010	RH/TIR1/ΔKU80/ΔHXGPRT/SPARKEL-TurboID-Ty. Mycoplasma negative.
Strain, strain background RH (T. gondii)	TurboID-SPARKEL	This paper	TGGT1_291010	RH/TIR1/ΔKU80/ΔHXGPRT/3xHA-TurboID-SPARKEL. Mycoplasma negative.
Strain, strain background RH (T. gondii)	SPARKEL-Ty	This paper	TGGT1_291010	RH/TIR1/ΔKU80/ΔHXGPRT/SPARKEL-V5-mNG-Ty. Mycoplasma negative.

Strain, strain background RH (T. gondii)	SPARKEL-mNG/SPARK-mCherry	This paper	TGGT1_268210, TGGT1_291010	RH/TIR1/ΔKU80/ΔHXGPRT/SPARKEL-V5-mNG-Ty/SPARK-V5-mCherry-HA/HXGPRT. Mycoplasma negative.
Strain, strain background RH (T. gondii)	SPARKEL-AID	This paper	TGGT1_291010	RH/TIR1/ΔKU80/ΔHXGPRT/SPARKEL-V5-HaloTag-mAID-Ty. Mycoplasma negative.
Strain, strain background RH (T. gondii)	SPARKEL-AID/ME49	This paper	TGGT1_291010	ME49/TIR1/ΔKU80/ΔHXGPRT/SPARKEL-V5-HaloTag-mAID-Ty. Mycoplasma negative.
Strain, strain background RH (T. gondii)	SPARKEL-AID/GCaMP	This paper	TGGT1_291010	RH/TIR1/pMIC2-MIC2-GLuc-myc-P2A-GCaMP6f/ΔKU80/ΔHXGPRT/SPARKEL-V5-HaloTag-mAID-Ty.

				Mycoplasma negative.
Strain, strain background RH (T. gondii)	SPARKEL-AID/SPARK-mCherry	This paper	TGGT1_268210, TGGT1_291010	RH/TIR1/ΔKU80/ΔHXGPRT/SPARKEL-V5-HaloTag-mAID-Ty/SPARK-V5-mCherry-HA/HXGPRT. Mycoplasma negative.
Strain, strain background RH (T. gondii)	SPARK-AID	This paper	TGGT1_268210	RH/TIR1/ΔKU80/ΔHXGPRT/SPARK-V5-mAID-HA/HXGPRT. Mycoplasma negative.
Strain, strain background RH (T. gondii)	SPARK-AID/SPARKEL-mNG	This paper	TGGT1_268210, TGGT1_291010	RH/TIR1/ΔKU80/ΔHXGPRT/SPARKEL-V5-mNG-Ty/SPARK-V5-mAID-HA/HXGPRT. Mycoplasma

				negative.
Strain, strain background RH (T. gondii)	PKA R-AID	This paper	TGGT1_242070	RH/TIR1/ΔKU80/ΔHXGPRT/PKA R-V5-mAID-HA/HXGPRT. Mycoplasma negative.
Strain, strain background RH (T. gondii)	AID-SPARKEL	This paper	TGGT1_291010	RH/TIR1/ΔKU80/ΔHXGPRT/3xHA-mAID-SPARKEL. Mycoplasma negative.
Strain, strain background RH (T. gondii)	SPARK-TurboID	This paper	TGGT1_268210	RH/TIR1/ΔKU80/ΔHXGPRT/SPARK-TurboID-Ty. Mycoplasma negative.
Strain, strain background RH (T. gondii)	PKA C1-mNG/PKA R-mCherry	This paper	TGGT1_226030, TGGT1_242070	RH/TIR1/ΔKU80/ΔHXGPRT/PKA C1-mNG-3myc/PKA R-mCherry-Ty. Mycoplasma

				negative.
Strain, strain background RH (T. gondii)	SPARKEL-AID/PKA C1-mNG/PKA R-mCherry	This paper	TGGT1_291010, TGGT1_226030, TGGT1_242070	RH/TIR1/ΔKU80/ΔHXGPRT/PKA C1-mNG-3myc/PKA R-mCherry-Ty/SPARKEL-V5-HaloTag-mAID-Ty. Mycoplasma negative.
Strain, strain background RH (T. gondii)	SPARK-AID/PKA C1-mNG	This paper	TGGT1_268210, TGGT1_226030	RH/TIR1/ΔKU80/ΔHXGPRT/SPARK-V5-mAID-HA/HXGPRT/PKA C1-mNG-3myc. Mycoplasma negative.
Strain, strain background RH (T. gondii)	SPARK-AID/PKA C1-mNG/PKA R-mCherry	This paper	TGGT1_268210, TGGT1_226030, TGGT1_242070	RH/TIR1/ΔKU80/ΔHXGPRT/SPARK-V5-mAID-HA/HXGPRT/PKA C1-mNG-3myc/PKA R-

				mCherry-P2A-DHFR. Mycoplasma negative.
Strain, strain background RH (T. gondii)	PKA C3-AID	This paper	TGGT1_286470	RH/TIR1/ΔKU80/ΔHXGPRT/PKA C3-V5-mNG-mAID-Ty. Mycoplasma negative.
Strain, strain background RH (T. gondii)	PKA C3-AID/ME49	This paper	TGGT1_286470	ME49/TIR1/ΔKU80/ΔHXGPRT/PKA C3-V5-mNG-mAID-Ty. Mycoplasma negative.
Strain, strain background RH (T. gondii)	SPARK-AID/ΔBFD1	This paper	TGGT1_268210, TGGT1_200385	RH/TIR1/ΔKU80/ΔHXGPRT/ΔBFD1::dTomato/SPARK-V5-mAID-HA/HXGPRT. Mycoplasma negative.

Strain, strain background RH (T. gondii)	PKA C3-AID/ΔBFD1	This paper	TGGT1_286470, TGGT1_200385	RH/TIR1/ΔKU80/ΔHXGPRT/ΔBFD1::dTomato/PKA C3-V5-mNG-mAID-Ty. Mycoplasma negative.
Strain, strain background RH (T. gondii)	PKA C3-mNG/SPARK-AID	This paper	TGGT1_286470, TGGT1_268210	RH/TIR1/ΔKU80/ΔHXGPRT/PKA C3-mNG-P2A-DHFR/SPARK-V5-mAID-HA/HXGPRT. Mycoplasma negative.
Cell line (Homo sapiens)	Human Foreskin Fibroblasts (HFFs)	ATCC	SCRC-1041	Mycoplasma negative
Antibody	Rat monoclonal (16D7) anti-mCherry	Thermo Fisher		IFA (1/1,000)
Antibody	Mouse monoclonal (32F6) anti-mNG	ChromoTek		IFA (1/1,000) and WB (1/500)
Antibody	Guinea pig monoclonal anti-CDPK1	Covance	Custom antibody	WB (1/50,000)

Antibody	Rabbit polyclonal anti-GAP45	Lampire Biological Laboratory		Provided by R. Drew Etheridge Lab. IFA (1/1,000). Used for differentiation assays.
Antibody	Rabbit polyclonal anti-GAP45	PMID: 18312842		Provided by Dominique Soldati-Favre Lab. IFA (1/10,000)
Antibody	Mouse polyclonal anti-SAG1	PMID: 3183382		Provided by L. David Sibley Lab. IFA (1/1,000). Used for invasion assays.
Antibody	Mouse monoclonal anti-V5	Invitrogen	Invitrogen:R960-25	WB (1/1000)
Antibody	Mouse monoclonal anti-TUB1 (clone 12G10)	Developmental Studies Hybridoma Bank at the University of Iowa	RRID:AB_1157911	WB (1/5000)
Antibody	Rat monoclonal (3F10) anti-HA	Roche	RRID: AB_390919	IFA (1/1000)
Antibody	Mouse monoclonal (BB2) anti-Ty1		PMID: 8813669	Protein G crosslinking (60 µg/1 mg beads)
Antibody	Rabbit polyclonal clone WU1614 anti-ALD	PMID: 16923803		Provided by L. David Sibley Lab. WB (1/10,000)
Antibody	biotinylated dolichos	Vector labs B-1035		IFA (1/1000)
Chemical compound, drug	Hoechst 33342	Invitrogen	Invitrogen:H3570	IFA (1/20,000)

Chemical compound, drug	DAPI (4',6-Diamidino-2-Phenylindole, Dihydrochloride)	Invitrogen	Invitrogen: D1306	
Chemical compound, drug	Prolong Diamond	Thermo Fisher	Thermo Fisher: P36965	
Chemical compound, drug	Zaprinast	Calbiochem	Calbiochem:684500	Egress assay (500 µM)
Chemical compound, drug	A23187	Calbiochem	Calbiochem:100105	Egress assay (2 µM)
Chemical compound, drug	Compound 1	PMID: 12455981		Egress assay (as indicated)
Chemical compound, drug	Biotin	Sigma Aldrich	Sigma Aldrich: B4501-1G	TurboID (500 µM)
Commercial assay or kit	S-trap micro	Protifi	Protifi: C02-micro-80	
Commercial assay or kit	Pierce Quantitative Fluorometric Peptide Assay	Thermo Fisher Scientific	Thermo Fisher Scientific: 23290	
Commercial assay or kit	TMT10plex™ Label Reagent Set	Thermo Fisher Scientific	Thermo Fisher Scientific: 90111	
Commercial assay or kit	TMTpro™ 16plex Label Reagent Set	Thermo Fisher Scientific	Thermo Fisher Scientific: A44522	
Commercial assay or kit	EasyPep™ MS Sample Prep Kits - Maxi	Thermo Fisher Scientific	Thermo Fisher Scientific: A45734	
Commercial assay or kit	High-Select TiO_2 Phosphopeptide Enrichment Kit	Thermo Fisher Scientific	Thermo Fisher Scientific: A32993	

Commercial assay or kit	High-Select™ Fe-NTA Phosphopeptide Enrichment Kit	Thermo Fisher Scientific	Thermo Fisher Scientific: A32992	
Commercial assay or kit	Pierce High pH Reversed-Phase Peptide Fractionation Kit	Thermo Fisher Scientific	Thermo Fisher Scientific:84868	
Commercial assay or kit	Pierce™ Streptavidin Magnetic Beads	Thermo Scientific	Thermo Scientific: 88817	
Commercial assay or kit	Sep-Pak C18 Plus Short Cartridge, 360 mg Sorbent per Cartridge, 55-105 µm	Waters	Waters: WAT020515	
Commercial assay or kit	Pierce Protein G Magnetic Beads	Thermo Fisher	Thermo-Fisher:88847	
Commercial assay or kit	mNeonGreen-Trap Magnetic Agarose	ChromoTek	ChromoTek:ntma-20	
Commercial assay or kit	NEXTFLEX® Poly(A) Beads 2.0 Kit	Perkin Elmer	NOVA-512993	
Recombinant DNA reagent	All plasmids used in this study are listed in Supplementary File 5	This paper		

Sequence-based reagent	All plasmids used in this study are listed in Supplementary File 5	This paper		
Software, algorithm	Proteome Discoverer 4.2	Thermo Fisher		
Software, algorithm	R version 4.0	R Foundation for Statistical Computing		
Software, algorithm	Prism 8	GraphPad		
Software, algorithm	HHPRED	PMID:29258817		
Software, algorithm	MEGA	PMID: 33892491		
Software, algorithm	ClustalW	PMID: 17846036		
Software, algorithm	TrimGalore version 0.6.7	doi:10.5281/zenodo.7598955		
Software, algorithm	STAR version 2.7.1a	PMID: 23104886		
Software, algorithm	featureCounts version 1.6.2	PMID: 24227677		
Software, algorithm	DESeq2 version 1.30.1	PMID: 25516281		

MATERIALS & METHODS

Reagents and cell culture

T. gondii parasites of the type I RH strain Δ*ku80*/Δ*hxgprt* genetic background (ATCC PRA-319, (Huynh and Carruthers, 2009)) or the type II ME49 strain Δ*ku80*/Δ*hxgprt* background (Waldman et al., 2020) were grown in human foreskin fibroblasts (HFFs, ATCC SCRC-1041) maintained in DMEM (GIBCO) supplemented with 3% calf serum and 10 µg/mL gentamicin (Thermo Fisher Scientific). When noted, DMEM was supplemented with 10% inactivated fetal calf serum and 10 µg/mL gentamicin. HFFs and parasites were tested routinely for mycoplasma using the ATCC Universal Mycoplasma Detection Kit (30-1012K).

Oligonucleotide sequences are listed in **Supplementary File 5**.

617 **Parasite transfection and strain construction**

618 *Genetic background of established parasite strains*

619 This study used the following strains that have been characterized in other publications:
620 RHΔku80Δhxgprt/TIR1 (Brown et al., 2017), ME49Δku80Δhxgprt/TIR1 (Licon et al., 2023)
621 RHΔku80Δhxgprt/TIR1/pTUB1-GCaMP6f (Smith et al., 2022), RHΔku80Δhxgprt/TIR1/pMIC2-MIC2-
622 Gluc-myc-P2A-GCaMP6f (Herneisen et al., 2022), PKG-mAID-HA/RHΔku80/TIR1 (Brown et al., 2017),
623 CDPK1-mNG-mAID-Ty/RHΔku80Δhxgprt/TIR1 (Shortt et al., 2022; Smith et al., 2022), SPARK-mNG-
624 mAID-Ty/RHΔku80Δhxgprt/TIR1 (Smith et al., 2022), SPARK-mCherry-mAID-
625 HA/RHΔku80Δhxgprt/TIR1/pTUB1-GCaMP6f (Smith et al., 2022), and pMIC2-mNG-TurboID-
626 Ty/RHΔku80Δhxgprt/TIR1 (Chan et al., 2023). The strains described below were derived from these
627 parental lines.
628
629
630 *SPARK-V5-mNG-Ty/RHΔku80Δhxgprt*

631 The HiT vector cutting unit gBlock described for SPARK in (Smith et al., 2022) was cloned into the
632 pALH193 HiT empty vector, which is based on the pGL015 cloning vector (GenBank: OM640005) but
633 possesses the XTEN-V5-mNG-Ty-3'CDPK3/DHFR tagging unit. The vector was linearized with BsaI and
634 co-transfected with the pSS014 Cas9 expression plasmid (GenBank: OM640002) into RHΔku80Δhxgprt
635 parasites. Clones were selected with 1 µM pyrimethamine and isolated via limiting dilution. Clones were
636 verified by immunofluorescence microscopy and immunoprecipitation and mass spectrometry.
637
638 *SPARKEL-V5-mNG-Ty/SPARK-V5-mCherry-HA/RHΔku80Δhxgprt/TIR1*

639 The HiT vector cutting unit gBlock for SPARKEL (P1) was cloned into the pALH193 HiT empty vector.
640 The vector was linearized with BsaI and co-transfected with the pSS014 Cas9 expression plasmid into
641 RHΔku80Δhxgprt/TIR1 parasites. Clones were selected with 1 µM pyrimethamine and isolated via
642 limiting dilution to generate the *SPARKEL-V5-mNG-Ty/RHΔku80Δhxgprt/TIR1* strain. The HiT vector
643 cutting unit gBlock described for SPARK in (Smith et al., 2022) was cloned into the pALH142 HiT empty
644 vector, which is based on the pALH052 cloning vector (GenBank: OM863784) but possesses the XTEN-
645 V5-mCherry-HA-3'CDPK3/HXGPRT tagging unit. The BsaI-linearized template was co-transfected with
646 pSS014 into the *SPARKEL-V5-mNG-Ty/RHΔku80Δhxgprt/TIR1* strain. Clones were selected with
647 25 µg ml^{-1} mycophenolic acid and 50 µg ml^{-1} xanthine and isolated via limiting dilution. Clones were
648 verified by immunofluorescence microscopy.
649
650 *SPARKEL-V5-HaloTag-mAID-Ty/RHΔku80Δhxgprt/TIR1, SPARKEL-V5-HaloTag-mAID-*
651 *Ty/ME49Δku80Δhxgprt/TIR1, SPARKEL-V5-HaloTag-mAID-Ty/RHΔku80Δhxgprt/TIR1/pMIC2-MIC2-Gluc-*
652 *myc-P2A-GCaMP6f* and *SPARKEL-V5-HaloTag-mAID-Ty/SPARK-V5-mCherry-HA/RHΔku80Δhxgprt/TIR1*

653 The HiT vector cutting unit gBlock for SPARKEL was cloned into the pALH076 HiT empty vector, which
654 is based on the pGL015 cloning vector (GenBank: OM640005) but possesses the XTEN-V5-HaloTag-
655 mAID-Ty-3'CDPK3/DHFR tagging unit. The vector was linearized with BsaI and co-transfected with the

656 pSS014 Cas9 expression plasmid into RHΔku80Δhxgprt/TIR1, RHΔku80Δhxgprt/TIR1/pMIC2-MIC2-
657 Gluc-myc-P2A-GCaMP6f, or ME49Δku80Δhxgprt/TIR1 parasites. Clones were selected with 1 µM
658 pyrimethamine and isolated via limiting dilution to generate the *SPARKEL-V5-HaloTag-mAID-*
659 *Ty/RHΔku80Δhxgprt/TIR1* strain. The linearized SPARK-V5-mCherry-HA HiT vector described above was
660 co-transfected with pSS014 into the *SPARKEL-V5-HaloTag-mAID-Ty/RHΔku80Δhxgprt/TIR1* strain.
661 Clones were selected with 25 µg ml^{-1} mycophenolic acid and 50 µg ml^{-1} xanthine and isolated via
662 limiting dilution. Clones were verified by PCR amplification and sequencing of the junction between the
663 3′ end of SPARKEL (5′-GGGAGGCCACAACGGCGC-3′) and 5′ end of the protein tag (5′-
664 gggggtcggtcatgttacgt-3′), immunoblotting, and immunoprecipitation and mass spectrometry.
665
666 *SPARK-V5-mAID-HA and PKA R-V5-mAID-HA/RHΔku80Δhxgprt/TIR1*

667 HiT cutting units previously described for SPARK (Smith et al., 2022) and PKA R (P2) were cloned into
668 HiT empty vector pALH086 (XTEN-V5-mAID-HA-3′CDPK3/HXGPRT; GenBank ON312869). In the case
669 of the PKA R vector, the CDPK3 3′UTR was exchanged for the sequence 1092 base pairs downstream of
670 the PKA R stop codon. The vectors were linearized and co-transfected with the Cas9 plasmid pSS014
671 into the *RHΔku80Δhxgprt/TIR1* strain. Clones were selected with 25 µg ml^{-1} mycophenolic acid and
672 50 µg ml^{-1} xanthine and isolated via limiting dilution. In-frame tagging of PKA R was notably rare.
673 Clones were verified by PCR amplification and sequencing of the junction between the 5′ end of the
674 protein tag (5′-gggggtcggtcatgttacgt-3′) and 3′ end of SPARK (5′-GACGCAAAACTGGCAAGACG-3′) or
675 the 5′UTR of the DHFR selection cassette (5′-tcgacaacgaatgacacaca-3′) and 3′ end of PKA R (5′-
676 GTGCGCATCTTGGAAGACATGGATC-3′).
677
678 *3HA-mAID-SPARKEL/RHΔku80Δhxgprt/TIR1*

679 An N-terminal HiT cutting unit designed for SPARKEL (P3) was cloned into HiT empty vector pALH460,
680 which is based on the pTUB1-DD HiT vector described in (Licon et al., 2023) but with the 5′DHFR-DHFR-
681 T2A-3HA-mAID-XTEN tagging unit. The vector was linearized and co-transfected with the Cas9
682 plasmid pSS014 into the *RHΔku80Δhxgprt/TIR1* strain. Clones were selected with 1 µm pyrimethamine
683 and isolated via limiting dilution. Clones were verified for in-frame tagging via immunofluorescence
684 microscopy.
685
686 *PKA C1-mNG-3myc/PKA R-mCherry-Ty/RHΔku80Δhxgprt/TIR1 and SPARKEL-V5-HaloTag-mAID-Ty/PKA*
687 *C1-mNG-3myc/PKA R-mCherry-Ty*

688 The HiT cutting unit for PKA C1 (P4) was cloned into the HiT empty vector pALH4052, which is based on
689 the pGL015 cloning vector (GenBank: OM640005) but possesses the XTEN-mNG-3myc-3′CDPK3
690 tagging unit. The HiT cutting unit for PKA R (P3) was cloned into the HiT empty vector pALH4082,
691 which is based on the pGL015 cloning vector (GenBank: OM640005) but possesses the XTEN-mCherry-
692 Ty-3′CDPK3 tagging unit. The vectors were linearized and co-transfected with the Cas9 plasmid pSS014
693 into the *RHΔku80Δhxgprt/TIR1* strain. Clones were sorted on the basis of mNG and mCherry
694 fluorescence and were isolated via limiting dilution. Clones were verified by live microscopy and flow
695 cytometry. The linearized *SPARKEL-V5-HaloTag-mAID-Ty* HiT vector described above was transfected

696 into the *PKA C1-mNG-3myc/PKA R-mCherry-Ty/RHΔku80Δhxgprt/TIR1* strain with pSS014. Clones were
697 selected with 1 µM pyrimethamine and isolated via limiting dilution.
698
699 *SPARK-V5-mAID-HA/PKA C1-mNG-3myc/PKA R-V5-mCherry-2A-DHFR*

700 The PKA C1-mNG-3myc HiT vector described above was co-transfected with pSS014 into the SPARK-
701 V5-mAID-HA/RHΔku80/TIR1 strain. Clones were sorted on the basis of mNG fluorescence and were
702 isolated via limiting dilution. Clones were verified by live microscopy. The HiT cutting unit described for
703 PKA R above was cloned into the HiT empty vector pALH5292, which is based on the pGL015 cloning
704 vector (GenBank: OM640005) but possesses the XTEN-V5-mCherry-P2A-DHFR tagging unit. This
705 vector was linearized with BsaI and was transfected with pSS014 into the SPARK-V5-mAID-HA/PKA C1-
706 mNG-3myc/RHΔku80/TIR1 strain. Clones were selected with 1 µM pyrimethamine and isolated via
707 limiting dilution. Clones were verified by live microscopy.
708
709 *PKA C3-V5-mNG-mAID-Ty/RHΔku80Δhxgprt/TIR1 and PKA C3-V5-mNG-mAID-*
710 *Ty/ME49Δku80Δhxgprt/TIR1*

711 The HiT vector cutting unit gBlock for PKA C3 (P5) was cloned into the pGL015 HiT empty vector
712 (XTEN-V5-mNG-mAID-Ty-3′CDPK3/DHFR; GenBank OM640005). The vector was linearized with BsaI
713 and co-transfected with the pSS014 Cas9 expression plasmid into RHΔku80Δhxgprt/TIR1 or
714 ME49Δku80Δhxgprt/TIR1 parasites. Clones were selected with 1 µM pyrimethamine and isolated via
715 limiting dilution. Clones were verified by PCR amplification and sequencing of the junction between the
716 3′ end of PKA C3 (5′-CGGGGTCATGGGCTACCTG-3′) and 5′ end of the protein tag (5′-
717 gggggtcggtcatgttacgt-3′), immunofluorescence microscopy, immunoblotting, and
718 immunoprecipitation and mass spectrometry.
719
720 *PKA C3-V5-mNG-mAID-Ty/Δbfd1::dTomato/RHΔku80Δhxgprt/TIR1 and SPARK-V5-mAID-*
721 *HA/Δbfd1::dTomato/RHΔku80/TIR1*

722 The sequences 5′GGGGGGCTTGATGTAACAGA-3′ and 5′-cacacacttaagtacgggga-3′, which target
723 upstream of the BFD1 transcription start site (Markus et al., 2020; Waldman et al., 2020) and
724 downstream of its last exon, respectively, were cloned as small guide RNAs into the Cas9 plasmid
725 pSS013 pU6-Universal (Sidik et al., 2016a). A repair template sequence with 40 bases of homology
726 upstream to each of these guides was amplified from a pTUB1-dTomato-3'DHFR plasmid using the
727 oligos 5′-caacctgcaggggtcacctctacagtgtttcgcaccatccgtgtcatgtagcctgccaga-3′ and 5′-
728 cgactctacacggggaggaaggacgtcaacagaccctcttCATGCATGTCCCGCGTTCGT-3′. This repair template was
729 co-transfected with the two sgRNA plasmids described above into *PKA C3-V5-mNG-mAID-*
730 *Ty/RHΔku80Δhxgprt/TIR1* and *SPARK-V5-mAID-HA/RHΔku80Δhxgprt/TIR1*. Clones were sorted on the
731 basis of dTomato fluorescence and were isolated via limiting dilution. Clones were verified by live
732 microscopy and PCR amplification of the junctions spanning upstream of the BFD1 transcription start
733 site and in the first exon of BFD1 or the 3′ sequence of dTomato. The oligos used for this amplification
734 are included in **Supplementary File 5**.
735

736

737 *PKA C3-mNG-P2A-DHFR/SPARK-V5-mAID-HA/RHΔku80/TIR1*

738 The HiT vector cutting unit gBlock for PKA C3 described above was cloned into the pALH459 HiT empty
739 vector, which is based on the pGL015 cloning vector (GenBank: OM640005) but possesses the XTEN-
740 mNG-P2A-DHFR tagging unit. The vector was linearized with BsaI and co-transfected with the pSS014
741 Cas9 expression plasmid into SPARK-V5-mAID-HA/RHΔku80/TIR1 parasites (described above). Clones
742 were selected with 1 µM pyrimethamine and isolated via limiting dilution. Clones were verified by PCR
743 amplification and sequencing of the junction between the 3′ end of PKA C3 (5′-
744 CGGGGTCATGGGCTACCTG-3′) and 3′ end of the DHFR selection cassette (5′-gggcagcttctgtatttccg-3′),
745 immunofluorescence microscopy, immunoblotting, and flow cytometry.

746

747 *SPARK-TurboID-Ty and SPARKEL-TurboID-Ty/RHΔku80Δhxgprt/TIR1*

748 The HiT vector cutting unit gBlocks for SPARK and SPARKEL described above were cloned into the
749 pALH173 HiT empty vector with the XTEN-TurboID-Ty-3′CDPK3/DHFR tagging payload (Chan et al.,
750 2023). The vectors were linearized with BsaI and co-transfected with the pSS014 Cas9 expression
751 plasmid into *RHΔku80Δhxgprt/TIR1* parasites. Clones were selected with 1 µM pyrimethamine and
752 isolated via limiting dilution. Clones were verified by PCR amplification and sequencing of the junction
753 between the 3′ end of SPARK and SPARKEL (using oligos described above) and the 5′ end of the
754 protein tag (5′-gggggtcggtcatgttacgt-3′) as well as mass spectrometry.

755

756 *3HA-TurboID-SPARKEL/RHΔku80Δhxgprt/TIR1*

757 An N-terminal HiT cutting unit designed for SPARKEL (P3) was cloned into HiT empty vector pALH461,
758 which is based on the pTUB1-DD HiT vector described in (Licon et al., 2023) but with the 5′DHFR-
759 DHFR-T2A-3HA-TurboID-XTEN tagging unit. The vector was linearized and co-transfected with the
760 Cas9 plasmid pSS014 into the *RHΔku80Δhxgprt/TIR1* strain. Parasites selected with 1 µm
761 pyrimethamine. Integration of the construct was verified by immunofluorescence microscopy.

762

763 **Immunoprecipitation and mass spectrometry**

764 *SPARK-mNG-mAID, SPARK-mNG, and PKA C3-mNG IPs*

765 Approximately 2×10^8 extracellular SPARK-mNG/SPARK-mNG-mAID or *Δku80Δhxgprt/* TIR1
766 tachyzoites were concentrated by spinning and resuspended in a volume of 400 µl lysis buffer (5 mM
767 NaCl, 142 mM KCl, 1 mM $MgCl_2$, 5.6 mM glucose, 25 mM HEPES pH 7.2 with 0.8% IGEPAL CA-630, 1X
768 Halt Protease Inhibitors, and 250 U/ml benzonase). After 20 minutes on ice, the parasite lysates were
769 combined with mNeonGreen-Trap Magnetic Agarose (ChromoTek) and were incubated with rotation at
770 4°C for 1 hour. The beads were washed three times with lysis buffer. Bound proteins were eluted with
771 5% SDS in 50 mM TEAB pH 8.5 for 10 minutes at 70°C. The eluates were reduced with 5 mM TCEP for
772 20 minutes at 50°C. Alkylation was performed with 20 mM MMTS at room temperature for 10 minutes.
773 The samples were then precipitated, washed, and digested with 1 µg trypsin/LysC using the S-trap mini

774 columns (Protifi) according to the manufacturer's protocol. Eluted peptides were lyophilized and stored
775 at -80°C until analysis. PKA C3-mNG samples were harvested and processed in the same way, except
776 the corresponding control strain was mNG-TurboID-Ty/*Δku80Δhxgprt.*
777
778 *SPARKEL-Ty IPs*

779 Approximately 2 ×10^8 extracellular SPARKEL-mNG-Ty or *Δku80Δhxgprt* tachyzoites were concentrated
780 by spinning and resuspended in a volume of 400 µl lysis buffer (10 mM Tris-HCl pH 7.5, 140 mM NaCl,
781 1% IGEPAL CA-630, 0.1% sodium deoxycholate, 0.1% SDS, Halt protease inhibitors, and Pierce
782 universal nuclease). After 20 minutes on ice, the parasite lysates were combined with anti-Ty (BB2)
783 conjugated Protein G beads and were incubated with rotation at 4°C for 1 hour (Huet et al., 2018). The
784 beads were washed three times with lysis buffer. Bound proteins were eluted with 5% SDS in 50 mM
785 TEAB pH 8.5 for 10 minutes at 70°C. The eluates were reduced with 5 mM TCEP for 20 minutes at 50°C.
786 Alkylation was performed with 20 mM MMTS at room temperature for 10 minutes. The samples were
787 then precipitated, washed, and digested with 1 µg trypsin/LysC using the S-trap mini columns (Protifi)
788 according to the manufacturer's protocol. Eluted peptides were lyophilized and stored at -80°C until
789 analysis.
790

791 *Mass spectrometry data acquisition and analysis*

792 The lyophilized peptides were resuspended in 10-20 µl of 0.1% formic acid for MS analysis and were
793 analyzed on an Exploris 480 Orbitrap mass spectrometer equipped with a FAIMS Pro source (Bekker-
794 Jensen et al., 2020) connected to an EASY-nLC chromatography system using 0.1% formic acid in water
795 as Buffer A and 0.1% formic acid in 80% acetonitrile as Buffer B. SPARK-mNG and PKA C3-mNG IP
796 samples were separated at 300 nl/min on a 60-minute gradient of 1-2% B for 1 minute, 2-25% B for 41
797 minutes, 25-40% B for 6 minutes, and 40-100% B for 12 minutes. SPARKEL-Ty IP samples were
798 separated at 300 nl/min on a 90-minute gradient of 1-6% B for 1 minute, 6-21% B for 41 minutes, 21-
799 36% B for 21 minutes, 36-50% B for 10 minutes, and 50-100% B for 14 minutes. Both methods ended
800 with a seesaw gradient of 2% B for 6 minutes and 98% B for 6 minutes.
801

802 The orbitrap and FAIMS were operated in positive ion mode with a positive ion voltage of 1800V; with
803 an ion transfer tube temperature of 270°C; using standard FAIMS resolution and compensation
804 voltages of -50 and -65V. Peptides were filtered for a charge state of 2–6, and a dynamic exclusion of 20
805 seconds was applied. Full scan spectra were acquired in profile mode with 1 microscan at a resolution of
806 60,000, with a scan range of 350-1400 m/z, fill time of 25 milliseconds, normalized AGC target of 300%,
807 intensity threshold of 5×10^3. The top 15 MS2 spectra were acquired. MS2 spectra were generated with
808 a HCD collision energy of 30 at a resolution of 15,000 with a first mass at 110 m/z, an isolation window of
809 1.3 m/z, AGC target of 200%, and auto injection time.
810

811 Raw mass spectrometry files were processed with the Proteome Discoverer 2.4 software (Thermo).
812 Spectra were searched against the ToxoDB release49 GT1 protein database using Sequest HT (Thermo
813 Fisher Scientific). The search included the following post-translational modifications: dynamic
814 oxidation (+15.995 Da; M), dynamic acetylation (+42.011 Da; N-Terminus), dynamic phosphorylation

815 (+79.966 Da; S, T, Y), and static methylthio (+45.988 Da; C) with a mass tolerance of 10 ppm for
816 precursor ions and 0.2 Da for fragment ions. Enzymatic cleavage was set to trypsin, with 2 allowed
817 missed cleavages per peptide. False discovery was assessed using Percolator with a concatenated
818 target/decoy strategy using a strict FDR of 0.01, relaxed FDR of 0.05, and maximum Delta CN of 0.05.
819 Protein abundance values were calculated using default workflows. Only unique peptide quantification
820 values were used. Protein abundances were calculated from summation of peptide abundances.
821 Sample ratios were calculated based on protein abundances. Hypothesis testing was performed by t-
822 test on the background population of proteins and peptides. Protein abundances and statistical tests
823 are reported in **Supplementary File 1**. The mass spectrometry proteomics data have been deposited to
824 the ProteomeXchange Consortium via the PRIDE partner repository (Perez-Riverol et al., 2022) with
825 the following dataset identifiers: SPARK-mNG-mAID IPs, PXD039922; SPARK-mNG IPs, PXD039919;
826 SPARKEL-Ty IPs, PXD039979; PKA C3 IPs, PXD039896.

827

828 **Proximity labeling of intracellular TurboID strains and mass spectrometry**

829 *Parasite treatment and harvest*

830 Parasites freshly egressed from host cell monolayers and expressing SPARK-TurboID-Ty, SPARKEL-
831 TurboID-Ty, or mNG-TurboID-Ty were infected onto a 15-cm dish confluent with HFFs (approximately
832 1-4 × 10^7 parasites per dish). The parasites invaded and replicated in host cells for approximately 32
833 hours, at which point the media was aspirated and replaced with 10 ml of Ringer's solution (155 mM
834 NaCl, 2 mM $CaCl_2$, 3 mM KCl, 1mM $MgCl_2$, 3 mM NaH_2PO_4, 10 mM HEPES, 10 mM glucose) with 1% IFS
835 and 500 µM biotin. The dishes were incubated at 37°C and ambient CO_2 for 30 minutes to allow
836 equilibration of biotin across the host and parasite plasma membranes. The monolayers were then
837 scraped, and parasites were mechanically released by passage through a 27-gauge syringe into a
838 conical tube. The parasite suspension was diluted with phosphate-buffered saline (PBS) and was spun
839 at 1,500 x *g* for 5 minutes at ambient temperature. The supernatant was decanted. The parasite pellet
840 was resuspended in 1 ml PBS and transferred to a 1.5 ml protein low-bind tube. The tubes were spun at
841 4°C and 21,000 x *g* for 1 minute, after which the supernatant was discarded and the parasite pellet was
842 resuspended in 1 ml PBS. This spin and wash cycle was repeated twice more, for three washes total to
843 remove excess biotin and serum. After the final wash, the parasite pellet was resuspended in 500 µl lysis
844 buffer (140 mM NaCl, 1% IGEPAL CA-630, 0.1% sodium deoxycholate, 0.1% SDS, 10 mM Tris-HCl, pH
845 7.5 supplemented with Pierce protease inhibitors and benzonase), was snap-frozen in liquid nitrogen,
846 and was stored at –80°C until sample processing.

847

848 *Biotinylated protein enrichment and MS*

849 The frozen lysates were thawed and combined with 30 µl of Pierce magnetic streptavidin beads. The
850 samples were rotated for 1 hour at room temperature. The beads were magnetically separated and
851 were washed with 1 ml lysis buffer, 1 ml 1M KCl, 0.1 M NaCO3, 2M urea/10 mM Tris pH 8.0, and 1 ml
852 lysis buffer. Elution of bound proteins was performed with two incubations of 10 minutes at 37 or 70°C
853 in 5% SDS, 50 mM TEAB pH 8.5 with 2.5 mM biotin. The eluates were immediately reduced, alkylated,
854 and digested as described in the immunoprecipitation methods. TurboID samples were analyzed by MS
855 as were IP samples. The mass spectrometry proteomics data have been deposited to the
856 ProteomeXchange Consortium via the PRIDE partner repository (Perez-Riverol et al., 2022) with the

857 following dataset identifiers: SPARK-TurboID, PXD039983; SPARKEL-TurboID, PXD039985; TurboID-
858 SPARKEL, PXD039986.
859

860 **Immunofluorescence microscopy**

861 Where indicated, parasites were infected onto confluent HFFs and were allowed to grow for 24 hours.
862 Coverslips or coverglass were fixed in 4% formaldehyde in PBS unless otherwise noted. Following three
863 washes in PBS, the fixed cells were permeabilized with 0.25% triton for 10 minutes at room
864 temperature followed by three washes with PBS. The coverslips were incubated in blocking solution
865 (2% BSA in PBS) for 10 minutes at room temperature, followed by a 60-minute incubation in primary
866 antibody solution. After three washes with PBS, the coverslips were incubated in blocking solution at
867 room temperature for 5 minutes, followed by a 60-minute incubation in secondary antibody solution.
868 The coverslips were washed three times in PBS and once in water. Coverslips were mounted with
869 Prolong Diamond and were set for 30 minutes at 37°C. Imaging was performed with the Nikon Ti
870 Eclipse and NIS Elements software package.
871

872 **Immunoblotting**

873 *SPARK/SPARKEL co-depletion immunoblotting*

874 HFFs were infected with parasites of the TIR1, SPARKEL-HaloTag-mAID-Ty/TIR1, or SPARK-V5-
875 mCherry-HA/SPARKEL-V5-HaloTag-mAID-Ty/TIR1 strains. Approximately 16 hours later, IAA was
876 added to a final concentration of 500 µM to initiate the 24-hour depletion period. The following day,
877 IAA was added to the 3- and 1-hour treatment samples. The host cell monolayers were scraped and
878 harvested with spinning for 7 minutes at 1,500 x g. The parasite pellet was resuspended in 1 ml of HHE
879 and was spun again for 10 minutes at 2,000 x g and 4°C. The pellet was resuspended to 2×10^7 parasite
880 equivalents per 10 µl in lysis buffer (5 mM NaCl, 142 mM KCl, 1 mM $MgCl_2$, 5.6 mM glucose, 25 mM
881 HEPES pH 7.2 with 0.8% IGEPAL CA-630, 1X Halt Protease Inhibitors, 1X PMSF, and 250 U/ml
882 benzonase). The lysates were diluted with 5x laemmli buffer (10% SDS, 50% glycerol, 300 mM Tris HCl
883 pH 6.8, 0.05% bromophenol blue) and were boiled at 95°C for 5 minutes. Samples were run with 1×10^7
884 parasite equivalents per lane on a precast 4-15% SDS-PAGE gel. The gel was incubated in 20% ethanol
885 for 10 minutes and subsequently transfer buffer (25 mM TrisHCl, 192 mM glycine, 20% methanol) for 10
886 minutes. Samples were transferred onto a nitrocellulose membrane at 4°C for 1h at 100V. The
887 membrane was blocked for 1h in 5% milk in TBS-T and incubated overnight in primary antibody
888 solution (mouse anti-V5 at 1:1,000 dilution or mouse anti-TUB1 at 1:5,000 dilution) in 5% milk/TBS-T at
889 4°C. The membrane was incubated in secondary antibody solution (1:10,000 Goat anti-Mouse IgG
890 IRDye 800 or 680) in 5% milk/TBS-T for 1h at room temperature and was visualized by LI-COR Odyssey
891 CLx. Three 5-minute washes were performed between incubations in antibodies.
892

893 *PKA C3-AID immunoblotting*

894 HFFs were infected with parasites of the TIR1 and PKA C3-V5-mNG-mAID-Ty/TIR1 strains.
895 Approximately 16 hours later, IAA was added to a final concentration of 500 µM to initiate the 24-hour
896 depletion period. The following day, IAA was added to the 3- and 1-hour treatment samples. The host
897 cell monolayers were scraped and harvested with spinning for 7 minutes at 1,500 x g. The parasite pellet

898 was resuspended in 1 ml of HHE and was spun again for 10 minutes at 2,000 x g and 4°C. The pellet was
899 resuspended to 1×10^7 parasite equivalents per 10 µl in lysis buffer (5 mM NaCl, 142 mM KCl, 1 mM
900 $MgCl_2$, 5.6 mM glucose, 25 mM HEPES pH 7.2 with 0.8% IGEPAL CA-630, 1X Halt Protease Inhibitors, 1X
901 PMSF, and 250 U/ml benzonase). The lysates were diluted with 5x laemmli buffer (10% SDS, 50%
902 glycerol, 300 mM Tris HCl pH 6.8, 0.05% bromophenol blue) and were boiled at 95°C for 5 minutes.
903 Samples were run with 2×10^7 parasite equivalents per lane on a precast 4-15% SDS-PAGE gel. The gel
904 was incubated in 20% ethanol for 10 minutes and subsequently transfer buffer (25 mM TrisHCl, 192 mM
905 glycine, 20% methanol) for 10 minutes. Samples were transferred onto a nitrocellulose membrane at
906 4°C for 1h at 100V. The membrane was blocked for 1h in 5% milk in TBS-T and incubated overnight in
907 primary antibody solution (mouse anti-V5 at 1:1,000 dilution or mouse anti-TUB1 at 1:5,000 dilution) in
908 5% milk/TBS-T at 4°C. The membrane was incubated in secondary antibody solution (1:10,000 Goat
909 anti-Mouse IgG IRDye 800 or 680) in 5% milk/PBS for 1h at room temperature and was visualized by LI-
910 COR Odyssey CLx. Three 5-minute washes with TBS-T or PBS were performed between incubations in
911 primary and secondary antibodies, respectively. The expected molecular weight of PKA C3-V5-mNG-
912 mAID-Ty is 97.4 kDa, from the 40.2 kDa tagging payload (Smith et al., 2022) and 57.2 kDa protein
913 sequence.
914

915 **Plaque assays**

916 500 parasites of the indicated strain were inoculated into 12-well plates of HFFs maintained in D10 and
917 allowed to grow undisturbed for 7 days. IAA or vehicle (PBS) was added to a final concentration of 500
918 µM. Plates were washed with PBS and fixed for 10 min at room temperature with 70% ethanol. Staining
919 was performed for 5 min at room temperature with crystal violet solution, followed by two washes with
920 PBS, one wash with water, and drying.

921

922 **Replication assays**

923 Parasites recently egressed from host cells were allowed to invade coverslips confluent with HFFs for 1
924 hour, after which the media was aspirated and replaced with media containing 500 µM IAA or vehicle.
925 After 24 hours, coverslips were fixed with 4% formaldehyde for 10 minutes at room temperature. The
926 samples were prepared for immunofluorescence microscopy as described above, using anti-GAP45 as a
927 parasite counterstain. The number of parasites per vacuole was enumerated from three fields of view
928 acquired using a 40x objective. Significance was assessed using ANOVA and Tukey's test in R (4.0.4).

929

930 **Flow cytometry**

931 Parasites were infected into 6-well dishes. Eight hours later, the media was replaced. IAA was added to
932 wells at the appropriate time periods prior to sample harvest. The monolayers were scraped, and
933 parasites were mechanically released from host cells by passage through a 27-gauge syringe. Parasites
934 were then passed through a 5 µm filter. The samples were concentrated for 5 minutes via spinning at
935 1,000 x g. The media was replaced with 1 ml PBS. The parasite solutions were analyzed by flow
936 cytometry with a Miltenyi MACSQuant VYB. Histograms are representative of two biological replicates.

937

938 **Invasion assays**

939 Parasites expressing SPARKEL-AID and SPARK-AID (Smith et al., 2022) were grown in HFFs for 40h
940 with 24, 3, or 0h of treatment with 500 µM IAA. Extracellular parasites or parasites mechanically
941 released from the host cells were spun at 1,500 x *g* for 5 minutes and were resuspended in invasion
942 media (HEPES-buffered DMEM without phenol red) supplemented with 1% IFS. The parasite
943 suspension was normalized to 1×10^6 cells/ml, and 2×10^5 parasites were added to three wells of a 96-
944 well clear-bottom plate with confluent HFFs. The plate was spun at 290 x g for 5 minutes to distribute
945 parasites over the host cells. Parasites were allowed to invade for 20 minutes at 37°C and 5% CO_2. The
946 plate was washed once with PBS to remove unattached parasites and was fixed with 4% formaldehyde
947 in PBS for 15 minutes. Extracellular parasites were stained with mouse anti-SAG1 for 30 minutes at
948 room temperature. Following permeabilization with 0.25% triton-X100 for 10 minutes, all parasites
949 were stained with guinea-pig anti-CDPK1 for 30 minutes at room temperature. The wells were
950 incubated with a secondary antibody solution containing Hoechst for 30 minutes. The plate was imaged
951 at 20x magnification using a Nikon Ti Eclipse epifluorescence scope. The number of parasites invaded
952 was calculated by normalizing the number of intracellular, invaded parasites to host cell nuclei. Assays
953 were performed in biological triplicate. Mean invasion efficiencies for each biological replicate were
954 calculated from technical triplicates. Plotting and statistical tests were performed with ggplot2 and the
955 compare_means() function with a one-sided t-test.

956

957 **Zaprinast egress assays and GCaMP6f measurements**

958 Parasites expressing SPARKEL-AID and pMIC2-MIC2-Gluc-P2A-GCaMP6f at a defined genomic locus
959 (Herneisen et al., 2022) were grown in HFFs in glass-bottom dishes (35 mm, 1.5, Ibidi) for 25h with 24, 3,
960 or 0h of treatment with 500 µM IAA. The dishes were washed once with one volume of Ringer's buffer
961 (155 mM NaCl, 2 mM $CaCl_2$, 3 mM KCl, 1mM $MgCl_2$, 3 mM NaH_2PO_4, 10 mM HEPES, 10 mM glucose),
962 and the media was replaced with 500 µl of Ringer's solution. Imaging was recorded every 2s for 300
963 using an Eclipse Ti microscope (Nikon) with an enclosure maintained at 37 °C. After approximately 10s
964 of imaging, 1 ml of 750 µM zaprinast was added to the dish, for a final compound concentration of 500
965 µM. The same procedure was used to measure calcium mobilization in parasites expressing SPARK-AID
966 and GCaMP6f (Smith et al., 2022). GCaMP6f intensity was measured in regions of interest around
967 vacuoles containing two or more parasites using FIJI. Assays were performed on different days in
968 biological triplicate. Vacuoles were manually scored for time to egress. Plotting and statistical tests
969 were performed with ggplot2 and the scale_compare_means() function with a one-sided t-test.

970

971 **Compound 1 treatment egress assays**

972 HFF monolayers in a clear-bottomed 96-well plate were infected with 1×10^5 parasites of the TIR1 or
973 SPARK-AID strains in fluorobrite media supplemented with 10% calf serum. IAA or PBS were added to a
974 final concentration of 500 µM 24 hours before the start of the assay. The media on the wells was
975 aspirated, and wells were washed once with PBS to remove extracellular parasites. A fluorobrite
976 solution containing a 3x concentration of compound 1 was added to each well, and the plate was
977 incubated at 37°C and 5% CO_2 for 10 minutes. Ringer's solution with 2 µM A23187 was added to each
978 well, resulting in dilution of compound 1 to a 1x concentration. The plate was incubated at 37°C and 5%
979 CO_2 for 10 minutes, after which 16% formaldehyde was added to each well, resulting in a final
980 concentration of 4% formaldehyde in each well. Fixation occurred for 10 minutes. The plate was
981 washed with PBS three times. Wells were permeabilized with 0.25% Triton X-100 followed by three

982 washes with PBS. Parasites were stained with guinea pig anti-CDPK1 (Waldman et al., 2020) for 1 hour
983 at room temperature. After three washes with PBS, the wells were incubated in a secondary antibody
984 solution (Alexa Fluor 594 goat anti-guinea pig) for 30 minutes. The wells were washed three times with
985 PBS and were imaged using a BioTek Cytation 3; four fields were acquired at 20x magnification per
986 well. Percent egress was calculated as the ratio of liberated parasites to intact vacuoles. Curves were fit
987 to the percent egress data in Prism using a sigmoidal dose-response model and difference between the
988 TIR1 and SPARK-AID response curves was assessed with an extra sum of squares F-test. IC_{50} values
989 from individual replicates were assessed for difference using a paired t-test in Prism.

990

991 **Differentiation assays**

992 *Plate-based differentiation assays*

993 HFFs in black glass-bottom 96-well plates were infected with three dilutions ranging from 5×10^3–$2 \times$
994 10^4 tachyzoites. The plates were spun for 5 minutes at 290 x *g*. After a four-hour invasion period at 37°C
995 and 5% CO_2, the media was exchanged for DMEM supplemented with 10% FBS for spontaneous
996 differentiation assays or RPMI with 1% FBS for alkaline stress differentiation assays. Spontaneous and
997 alkaline stress differentiation assay samples were incubated at 37°C/5%CO_2 or 37°C/0% CO_2 for 48
998 hours, respectively, before fixation in 100% cold methanol for 2 minutes. The assays were incubated for
999 10 minutes at room temperature in blocking solution (1% bovine serum albumin in PBS). The wells were
1000 then incubated in a primary antibody blocking solution containing rabbit anti-GAP45 or biotinylated
1001 dolichos (Vector labs B-1035) for 30 minutes at room temperature. Secondary staining was performed
1002 with streptavidin-APC and goat anti-rabbit Alexa fluor 488 in blocking solution for 30 minutes at room
1003 temperature. Three PBS washes were performed between antibody incubations. Images were acquired
1004 with a widefield Nikon Ti epifluorescence scope. The percentage of DBL+ vacuoles was determined by
1005 manual quantification of vacuoles with DBL staining as a proportion of vacuoles with GAP45 staining.
1006 Images included in figure panels were false-colored in FIJI.

1007

1008 *Coverglass-based differentiation assays*

1009 HFFs confluent on coverglass were infected with 1×10^4–5×10^4 tachyzoites. After a four-hour invasion
1010 period at 37°C and 5% CO_2, the media was exchanged for DMEM supplemented with 10% FBS for
1011 spontaneous differentiation assays or RPMI with 1% FBS for alkaline stress differentiation assays.
1012 Spontaneous and alkaline stress differentiation assay samples were incubated at 37°C/5%CO_2 or
1013 37°C/0% CO_2 for 48 hours, respectively, before fixation in 4% formaldehyde in PBS for 10 minutes. The
1014 assays were incubated for 10 minutes at room temperature in blocking solution (1% bovine serum
1015 albumin in PBS). The wells were then incubated in a primary antibody blocking solution containing
1016 rabbit anti-GAP45 or guinea pig anti-CDPK1 or biotinylated dolichos (Vector labs B-1035) for 60
1017 minutes at room temperature. Secondary staining was performed with streptavidin-APC and goat anti-
1018 rabbit Alexa fluor 488 or goat anti-guinea pig Alexa fluor 488 in blocking solution for 60 minutes at
1019 room temperature. Three PBS washes were performed between antibody incubations. Images were
1020 acquired with a widefield Nikon Ti epifluorescence scope with 20x objective, with 3 images per
1021 coverslip. The percentage of DBL+ vacuoles was determined by manual quantification of vacuoles with
1022 DBL staining as a proportion of vacuoles with GAP45 staining. Images included in figure panels were
1023 false-colored in FIJI.

1024

1025 **SPARK 24h depletion proteome**

1026 *Parasite treatment and harvest*

1027 HFF monolayers were infected with parasites expressing SPARK-mNG-mAID. Eight hours later,
1028 uninvaded parasites were washed away. The replacement media contained 500 µM IAA or PBS vehicle.
1029 After 24 hours, the host cell monolayers were scraped, and parasites were mechanically released by
1030 passage through syringes with 27-gauge needles. The suspension was passed through 5 µm filters and
1031 collected into conical tubes, which were spun for 7 minutes at 1,000 x *g*. The supernatant was decanted,
1032 and the parasite pellet was resuspended in 1 ml Fluorobrite DMEM lacking serum. The suspension was
1033 spun for 1,000 x *g* for 5 minutes. The supernatant was aspirated, and an additional wash in Fluorobrite
1034 DMEM followed by a spin at 1,000 *x* g for 5 minutes was performed. The parasite pellet was resupended
1035 in 250 µl, and four technical replicates of 50 µl were combined with 50 µl of 2x lysis buffer (10% SDS, 4
1036 mM $MgCl_2$, 100 mM TEAB pH 7.55 with 2X Halt Protease and Phosphatase Inhibitors and 500 U/ml
1037 benzonase). The experiment was performed in biological duplicate.

1038

1039 *Proteomics sample preparation and TMT labeling*

1040 Samples were prepared as previously described (Herneisen et al., 2022). Lysates were reduced 5 mM
1041 TCEP at 55°C for 15 minutes. Alkylation was performed with 20 mM MMTS for 10 minutes at room
1042 temperature. After the lysates were acidified to a final concentration of 2.5% v/v phosphoric acid, a 6X
1043 volume of S-trap binding buffer (90% methanol, 100 mM TEAB pH 7.55) was added. The solution was
1044 loaded onto S-trap mini columns (Protifi) and spun at 4,000 x *g* until all of the solution had been passed
1045 through the column. The columns were washed four times with 150 µl S-trap binding buffer, followed
1046 by a 30 second spin at 4,000 x g. Proteins were digested overnight in 20 µl of 50 mM TEAB pH 8.5
1047 containing 2 µg of trypsin/LysC mix (Thermo Fisher Scientific) at 37°C in a humidified incubator.
1048 Peptides were eluted in three 40 µl washes with 50 mM TEAB, 0.2% formic acid, and 50%
1049 acetonitrile/0.2% formic acid. The eluted peptides were snap-frozen and lyophilized.

1050

1051 The dried peptides were resuspended in 50 µl 100 mM TEAB 8.5. The peptide concentrations of 1/50
1052 dilutions of the samples were quantified using the Pierce Fluorometric Peptide Assay according to
1053 manufacturer's instructions. Sample abundances were normalized to 50 µg peptides in 50 µl 100 mM
1054 TEAB pH 8.5. Each sample was combined with TMTpro reagents at a 5:1 label:peptide weight/weight
1055 ratio. Labeling reactions proceeded for 1 hour at room temperature with shaking at 350 rpm. Unreacted
1056 TMT reagent was quenched with 0.2% hydroxylamine. The samples were pooled, acidified to 3% with
1057 formic acid, and were loaded onto an EasyPep Maxi Sample Prep column. The samples were washed
1058 and eluted according to the manufacturer's instructions. The eluted peptides were snap-frozen and
1059 lyophilized until dry. Samples were fractionated with the Pierce High pH Reversed-Phase Peptide
1060 Fractionation Kit according to the manufacturer's instructions for TMT-labeled peptides.

1061

1062 *LC-MS data acquisition*

1063 The fractions were lyophilized and resuspended in 10-20 µl of 0.1% formic acid for MS analysis and were
1064 analyzed on an Exploris 480 Orbitrap mass spectrometer equipped with a FAIMS Pro source (Bekker-
1065 Jensen et al., 2020) connected to an EASY-nLC chromatography system. Peptides were separated at
1066 300 nl/min on a gradient of 5–20% B for 110 minutes, 20–28% B for 10 minutes, 28–95% B for 10
1067 minutes, 95% B for 10 minutes, and a seesaw gradient of 95–2% B for 2 minutes, 2% B for 2 minutes, 2–

98% B for 2 minutes, 98% B for 2 minutes, 98–2% B for 2 minutes, and 2% B for 2 minutes. The orbitrap and FAIMS were operated in positive ion mode with a positive ion voltage of 1800V; with an ion transfer tube temperature of 270°C; using FAIMS user defined mode with compensation voltages of -50 and -65V, an inner electrode temperature of 100°C, an outer electrode temperature of 85°C, with 4.6 ml/min carrier gas and a default charge state of 2. Full scan spectra were acquired in profile mode at a resolution of 60,000, with a scan range of 400-1400 m/z, automatically determined maximum fill time, 300% AGC target, intensity threshold of 5×10^4, 2-5 charge state, and dynamic exclusion of 30 seconds with a cycle time of 1.5 seconds between master scans. MS2 spectra were generated with a HCD collision energy of 32 at a resolution of 45,000 with a first mass at 110 m/z, an isolation window of 0.7 m/z, 200% AGC target, and 120 ms injection time.

Data analysis

Raw files were analyzed by Proteome Discoverer 4.2. Peak lists were generated using the Sequest HT search engine and ToxoDB GT1 version 49 sequence database. Trypsin was specified as the digestion enzyme, with a maximum of two missed cleavages. Modifications included dynamic oxidation (+15.995 Da; M), dynamic acetylation (+42.011 Da; N-terminus), static TMT6plex (+229.163 Da; N-terminus), static TMTpro (+304.207 Da; K), and static methylthio (+45.988 Da; C). The enriched sample analysis additionally searched for dynamic phosphorylation (+79.966 Da; S, T, Y). The allowed mass tolerance for precursor and fragment ions was 10 ppm and 0.02 Da, respectively. False discovery was assessed using Percolator with a concatenated target/decoy strategy using a strict FDR of 0.01, relaxed FDR of 0.05, and maximum Delta CN of 0.05. Protein abundance values were calculated using default workflows. Only unique peptide quantification values were used. Co-isolation and signal-to-noise thresholds were set to 50% and 10, respectively. Protein abundances were calculated from summation of peptide abundances. Normalization was performed according to total peptide amount. Sample ratios were calculated based on protein abundances. Hypothesis testing was performed by ANOVA against individual proteins. Protein abundances are reported in **Supplementary File 3**. The mass spectrometry proteomics data have been deposited to the ProteomeXchange Consortium via the PRIDE partner repository (Perez-Riverol et al., 2022) with the dataset identifier PXD040598.

SPARK, SPARKEL, and PKA C3 depletion time course proteomes

Parasite treatment and harvest

HFF monolayers were infected with parasites expressing SPARK-mNG-mAID, SPARKEL-HaloTag-mAID, or PKA C3-mNG-mAID. Eight hours later, uninvaded parasites were washed away. IAA was added to 500 µM for the indicated periods of time before the samples were harvested together 32 hours post-infection. The host cell monolayers were scraped, and parasites were mechanically released by passage through syringes with 27-gauge needles. The suspension was passed through 5 µm filters and collected into conical tubes, which were spun for 7 minutes at 1,000 x *g*. The supernatant was decanted, and the parasite pellet was resuspended in 1 ml Fluorobrite DMEM lacking serum. The suspension was spun for 1,000 x *g* for 5 minutes. The supernatant was aspirated, and an additional wash in Fluorobrite DMEM followed by a spin at 1,000 *x* g for 5 minutes was performed. The parasite pellet was resupended in 50 µl of 1x lysis buffer (5% SDS, 2 mM $MgCl_2$, 100 mM TEAB pH 7.55 with 1X Halt Protease and Phosphatase Inhibitors and 500 U/ml benzonase). The experiment was performed in biological duplicate.

1112 *Proteomics sample preparation and TMT labeling*

1113 Samples were reduced, alkylated, and digested as described for the SPARK 24h depletion proteome.
1114 The lyophilized peptides were quantified using a Pierce fluorometric peptide assay. Samples destined
1115 for phosphopeptide enrichment were normalized to 100 µg of peptides per channel and were labeled
1116 with 200 µg of TMT10plex reagents according to the manufacturer's protocol, with the following
1117 modifications. The eluates were combined with 200 µg of TMT10plex reagent in 15 µl of acetonitrile, for
1118 an estimated 1:2 w/w peptide:tag labeling reaction. The labeling proceeded for 1 hour at room
1119 temperature and was quenched for 15 minutes with 5% hydroxylamine. The samples were then pooled,
1120 flash-frozen, and lyophilized to dryness. The SPARKEL-AID proteome, which was not phospho-
1121 enriched, contained only 7 µg per channel and was labeled with 15 µg of TMT10plex reagent.

1122

1123 *Phosphopeptide enrichment*

1124 Phosphopeptide enrichment was performed as previously described (Herneisen et al., 2022) using the
1125 SMOAC protocol (Tsai et al., 2014). Resuspended TMT10plex-labeled samples were enriched with the
1126 High-Select™ TiO2 Phosphopeptide Enrichment Kit (Thermo Fisher Scientific A32993). The flow-
1127 through and the eluate from IMAC enrichment were immediately snap-frozen and lyophilized. The
1128 flow-through was resuspended and enriched with the High-Select™ Fe-NTA Phosphopeptide
1129 Enrichment Kit (Thermo Fisher Scientific A32992) according to the manufacturer's instructions. The
1130 eluted phosphopeptides were immediately snap-frozen and lyophilized. Unenriched and enriched
1131 proteome samples were fractionated with the Pierce High pH Reversed-Phase Peptide Fractionation Kit
1132 according to the manufacturer's instructions for TMT-labeled peptides. The phosphopeptides enriched
1133 with the TiO2 and Fe-NTA methods were combined prior to fractionation.

1134

1135

1136 *LC-MS data acquisition*

1137 The fractions were lyophilized and resuspended in 10-20 µl of 0.1% formic acid for MS analysis and were
1138 analyzed on an Exploris 480 Orbitrap mass spectrometer equipped with a FAIMS Pro source (Bekker-
1139 Jensen et al., 2020) connected to an EASY-nLC chromatography system as described above. Peptides
1140 were separated at 300 nl/min on a gradient of 6–21% B for 41 minutes, 21–36% B for 20 minutes, 36–
1141 50% B for 10 minutes, and 50 to 100% B over 15 minutes. The orbitrap and FAIMS were operated in
1142 positive ion mode with a positive ion voltage of 1800V; with an ion transfer tube temperature of 270°C;
1143 using standard FAIMS resolution and compensation voltages of -50 and -65V (injection 1) or -40 and -60
1144 (injection 2). Full scan spectra were acquired in profile mode at a resolution of 120,000, with a scan
1145 range of 350-1200 m/z, automatically determined maximum fill time, standard AGC target, intensity
1146 threshold of 5×10^3, 2-5 charge state, and dynamic exclusion of 30 seconds with a cycle time of 2
1147 seconds between master scans. MS2 spectra were generated with a HCD collision energy of 36 at a
1148 resolution of 30,000 using TurboTMT settings with a first mass at 110 m/z, an isolation window of 0.7
1149 m/z, standard AGC target, and auto injection time.

1150

1151 *Data analysis*

1152 Raw files were analyzed in Proteome Discoverer 2.4 (Thermo Fisher Scientific) to generate peak lists
1153 and protein and peptide IDs using Sequest HT (Thermo Fisher Scientific) and the ToxoDB GT1 version
1154 49 sequence database. The unenriched sample search included the following post-translational

1155 modifications: dynamic oxidation (+15.995 Da; M), dynamic acetylation (+42.011 Da; N-terminus), static
1156 TMT6plex (+229.163 Da; any N-terminus), static TMT6plex (+229.163 Da; K), and static methylthio
1157 (+45.988 Da; C). The enriched sample search included the same post-translational modifications, but
1158 with the addition of dynamic phosphorylation (+79.966 Da; S, T, Y). The mass spectrometry proteomics
1159 datasets have been deposited to the ProteomeXchange Consortium via the PRIDE partner repository
1160 (Perez-Riverol et al., 2022) with the following dataset identifiers: SPARK-AID phosphoproteomics,
1161 PXD040602; SPARKEL-AID proteomics, PXD040635; PKA C3-AID phosphoproteomics, PXD042989.

1162

1163 Exported peptide and protein abundance files from Proteome Discoverer 2.4 were loaded into R
1164 (version 4.0.4). The normalized abundance values of all peptides were used as input for a principal
1165 component analysis using the R stats package (version 3.6.2). The strain basal downregulation score
1166 was determined for the SPARK-AID phosphoproteome by calculating the modified z-score of the $\log_2$-
1167 ratios of altered abundances in the SPARK-AID strain with no IAA treatment relative to the TIR1
1168 parental strain. The IAA score was calculated by summing the $\log_2$-ratios of altered abundances in the
1169 SPARK-AID strain relative to the SPARK-AID untreated samples, followed by transformation into a
1170 modified z-score. Clustering analysis was performed with the mclust package (Scrucca et al., 2016)
1171 (version 5.4.7) using the $\log_2$ ratios of relative to the vehicle-treated SPARK-AID samples. Cluster
1172 assignments are reported in **Supplementary File X**. The PKA C3-AID phosphoproteome IAA score was
1173 calculated as described above; a strain basal downregulation score was not calculated because the
1174 experiment did not include a TIR1 parental sample.

1175

1176 **Enrichment Analysis**

1177 Gene ontology enrichment analysis was performed as described (Herneisen et al., 2022). Sets of gene
1178 ontology terms from the differentially regulated (SPARK-dependent) and background proteome (all
1179 proteins with quantification values in the SPARK-AID mass spectrometry experiment) were
1180 downloaded from ToxoDB.org (Molecular Function, Computed evidence, P-Value cutoff set to 1). Gene
1181 ontology terms were tested for enrichment across all gene ontology terms identified in the background
1182 proteome. A p-value for the likelihood of a given enrichment to have occurred by chance was obtained
1183 using a hypergeometric test.

1184

1185 **PKA R depletion phosphoproteome**

1186

1187 *Parasite treatment and harvest*

1188 HFF monolayers were infected with parasites expressing PKA R-V5-mAID-3HA. The next morning, IAA
1189 was added to 500 µM one hour prior to sample harvest. The host cell monolayers were scraped, and
1190 parasites were mechanically released by passage through syringes with 27-gauge needles. The
1191 suspension was passed through 5 µm filters and collected into conical tubes, which were spun for 7
1192 minutes at 1,000 x *g*. The supernatant was decanted, and the parasite pellet was resuspended in 1 ml
1193 Fluorobrite DMEM lacking serum. The suspension was spun for 1,000 x *g* for 5 minutes. The supernatant
1194 was aspirated, and an additional wash in Fluorobrite DMEM followed by a spin at 1,000 *x* g for 5 minutes
1195 was performed. The parasite pellet was resuspended in 250 µl Fluorobrite DMEM containing 500 µM
1196 zaprinast, and 50 µl of this suspension was combined at 0, 10, 30, and 60 seconds post-treatment with
1197 50 µl of 2x lysis buffer for a final composition of 5% SDS, 2 mM $MgCl_2$, 100 mM TEAB pH 7.55 with 1X

1198 Halt Protease and Phosphatase Inhibitors and 500 U/ml benzonase. The experiment was performed in
1199 biological duplicate.

1200

1201 *Proteomics sample preparation and TMT labeling*

1202 Samples were reduced, alkylated, and digested as described previously (Herneisen et al., 2022). In brief,
1203 the eluates were reduced with 5 mM TCEP for 20 minutes at 50°C. Alkylation was performed with 20
1204 mM MMTS at room temperature for 10 minutes. The samples were then precipitated, washed, and
1205 digested with 1 µg trypsin/LysC using the S-trap mini columns (Protifi) according to the manufacturer's
1206 protocol. The lyophilized peptides were quantified using a Pierce fluorometric peptide assay. Samples
1207 destined for phosphopeptide enrichment were normalized to 50 µg of peptides per channel at a
1208 concentration of 1 µg/µl and were labeled with 250 µg of TMTpro reagents according to the
1209 manufacturer's protocol, with volumes adjusted accordingly. The labeling proceeded for 1 hour at room
1210 temperature and was quenched for 15 minutes with 5% hydroxylamine. The samples were pooled,
1211 acidified to 3% with formic acid, and were loaded onto an EasyPep Maxi Sample Prep column. The
1212 samples were washed and eluted according to the manufacturer's instructions. The eluted peptides
1213 were snap-frozen and lyophilized until dry.

1214

1215 *Phosphopeptide enrichment*

1216 Phosphopeptide enrichment was performed as previously described (Herneisen et al., 2022) using the
1217 SMOAC protocol (Tsai et al., 2014). Resuspended TMTpro-labeled samples were enriched with the
1218 High-Select™ TiO2 Phosphopeptide Enrichment Kit (Thermo Fisher Scientific A32993). The flow-
1219 through and the eluate from IMAC enrichment were immediately snap-frozen and lyophilized. The
1220 flow-through was resuspended and enriched with the High-Select™ Fe-NTA Phosphopeptide
1221 Enrichment Kit (Thermo Fisher Scientific A32992) according to the manufacturer's instructions. The
1222 eluted phosphopeptides were immediately snap-frozen and lyophilized. Unenriched proteome samples
1223 were fractionated with the Pierce High pH Reversed-Phase Peptide Fractionation Kit according to the
1224 manufacturer's instructions for TMT-labeled peptides. The phosphopeptides enriched with the TiO2
1225 and Fe-NTA methods were combined prior to fractionation. Enriched proteome samples were
1226 fractionated with the Pierce High pH Reversed-Phase Peptide Fractionation Kit using the following
1227 gradients (% acetonitrile/0.1%triethylamine): 1.5, 3, 5, 7.5, 10, 15, 50. Samples were immediately flash-
1228 frozen and lyophilized to dryness.

1229

1230

1231 *LC-MS data acquisition*

1232 The fractions were lyophilized and resuspended in 5-15 µl of 0.1% formic acid for MS analysis and were
1233 analyzed on an Exploris 480 Orbitrap mass spectrometer equipped with a FAIMS Pro source (Bekker-
1234 Jensen et al., 2020) connected to an EASY-nLC chromatography system with a 15 cm column with 75
1235 µm diameter (Thermo Fisher ES900). Peptides were separated at 300 nl/min on a gradient of 5–20% B
1236 for 110 minutes, 20–28% B for 10 minutes, 28–95% B for 10 minutes, 95% B for 10 minutes, and a
1237 seesaw gradient of 95–2% B for 2 minutes, 2% B for 2 minutes, 2–98% B for 2 minutes, 98% B for 2
1238 minutes, 98–2% B for 2 minutes, and 2% B for 2 minutes. The orbitrap and FAIMS were operated in
1239 positive ion mode with a positive ion voltage of 1800V; with an ion transfer tube temperature of 270°C;
1240 using standard FAIMS resolution and compensation voltages of -50 and -65V, an inner electrode

1241 temperature of 100°C, and outer electrode temperature of 80°C with 4.6 ml/min carrier gas. Full scan
1242 spectra were acquired in profile mode at a resolution of 60,000, with a scan range of 400-1400 m/z,
1243 automatically determined maximum fill time, 300% AGC target, intensity threshold of 5×10^4, 2-5
1244 charge state, and dynamic exclusion of 30 seconds with a cycle time of 1.5 seconds between master
1245 scans. MS2 spectra were generated with a HCD collision energy of 32 at a resolution of 45,000 using
1246 TurboTMT settings with a first mass at 110 m/z, an isolation window of 0.7 m/z, 200% AGC target, and
1247 120 ms injection time.

1248

1249 *Data analysis*

1250 Raw files were analyzed in Proteome Discoverer 2.4 (Thermo Fisher Scientific) to generate peak lists
1251 and protein and peptide IDs using Sequest HT as described for the SPARK 24h depletion proteome. The
1252 mass spectrometry proteomics datasets have been deposited to the ProteomeXchange Consortium via
1253 the PRIDE partner repository (Perez-Riverol et al., 2022) with the dataset identifier PXD044398.

1254

1255 Exported peptide and protein abundance files from Proteome Discoverer 2.4 were loaded into R
1256 (version 4.0.4). Ratios relative to the vehicle-treated timepoint were standardized by a modified Z-
1257 score. Peptides with the same site phosphorylations were matched across the PKA R and SPARK
1258 depletion phosphoproteomes. We defined basally PKA C1-dependent phosphorylation sites as
1259 phosphopeptides that were up-regulated by more than two modified Z-scores when PKA R was
1260 depleted for one hour. The distributions of all phosphopeptides identified in both the SPARK and PKA R
1261 phosphoproteomes were compared with the distributions of PKA C1-dependent sites using a
1262 Kolmogorov-Smirnov test.

1263

1264 **PKG depletion phosphoproteome**

1265 *Parasite treatment and harvest*

1266 HFF monolayers were infected with parasites expressing PKG-mAID-3HA or the parental strain
1267 expressing TIR1. The next morning, IAA was added to 500 µM four hours prior to sample harvest. The
1268 host cell monolayers were scraped, and parasites were mechanically released by passage through
1269 syringes with 27-gauge needles. The suspension was passed through 5 µm filters and collected into
1270 conical tubes, which were spun for 7 minutes at 1,000 x *g*. The supernatant was decanted, and the
1271 parasite pellet was resuspended in 1 ml Fluorobrite DMEM lacking serum. The suspension was spun for
1272 1,000 x *g* for 5 minutes. The supernatant was aspirated, and an additional wash in Fluorobrite DMEM
1273 followed by a spin at 1,000 *x* g for 5 minutes was performed. The parasite pellet was resuspended in 250
1274 µl Fluorobrite DMEM containing 500 µM zaprinast, and 50 µl of this suspension was combined at 0, 10,
1275 30, and 60 seconds post-treatment with 50 µl of 2x lysis buffer for a final composition of 5% SDS, 2 mM
1276 $MgCl_2$, 100 mM TEAB pH 7.55 with 1X Halt Protease and Phosphatase Inhibitors and 500 U/ml
1277 benzonase. The experiment was performed in biological duplicate.

1278

1279 *Proteomics sample preparation and TMT labeling*

1280 Samples were reduced, alkylated, and digested as described previously (Herneisen et al., 2022). In brief,
1281 the eluates were reduced with 5 mM TCEP for 20 minutes at 50°C. Alkylation was performed with 20
1282 mM MMTS at room temperature for 10 minutes. The samples were then precipitated, washed, and
1283 digested with 1 µg trypsin/LysC using the S-trap mini columns (Protifi) according to the manufacturer's
1284 protocol. The lyophilized peptides were quantified using a Pierce fluorometric peptide assay. Samples

destined for phosphopeptide enrichment were normalized to 50 µg of peptides per channel at a concentration of 1 µg/µl and were labeled with 250 µg of TMTpro reagents according to the manufacturer's protocol, with volumes adjusted accordingly. The labeling proceeded for 1 hour at room temperature and was quenched for 15 minutes with 5% hydroxylamine. The samples were then pooled, flash-frozen, and lyophilized to dryness. The dry pooled sample was resuspended in 1 ml of 5% formic acid and was desalted using the EasyPep Maxi Kit (Thermo Scientific) according to the manufacturer's instructions. The eluted peptides were flash-frozen and lyophilized to dryness.

Phosphopeptide enrichment

Phosphopeptide enrichment was performed as previously described (Herneisen et al., 2022) using the SMOAC protocol (Tsai et al., 2014). Resuspended TMTpro-labeled samples were enriched with the High-Select™ TiO2 Phosphopeptide Enrichment Kit (Thermo Fisher Scientific A32993). The flow-through and the eluate from IMAC enrichment were immediately snap-frozen and lyophilized. The flow-through was resuspended and enriched with the High-Select™ Fe-NTA Phosphopeptide Enrichment Kit (Thermo Fisher Scientific A32992) according to the manufacturer's instructions. The eluted phosphopeptides were immediately snap-frozen and lyophilized. Unenriched proteome samples were fractionated with the Pierce High pH Reversed-Phase Peptide Fractionation Kit according to the manufacturer's instructions for TMT-labeled peptides. The phosphopeptides enriched with the TiO2 and Fe-NTA methods were combined prior to fractionation. Enriched proteome samples were fractionated with the Pierce High pH Reversed-Phase Peptide Fractionation Kit using the following gradients (% acetonitrile/0.1%triethylamine): 1.5, 3, 5, 7.5, 10, 15, 50. Samples were immediately flash-frozen and lyophilized to dryness.

LC-MS data acquisition

The fractions were lyophilized and resuspended in 5-15 µl of 0.1% formic acid for MS analysis and were analyzed on an Exploris 480 Orbitrap mass spectrometer equipped with a FAIMS Pro source (Bekker-Jensen et al., 2020) connected to an EASY-nLC chromatography system with a 25 cm column with 75 µm diameter (Thermo Fisher ES902). Peptides were separated at 300 nl/min on a gradient of 5–20% B for 110 minutes, 20–28% B for 10 minutes, 28–95% B for 10 minutes, 95% B for 10 minutes, and a seesaw gradient of 95–2% B for 2 minutes, 2% B for 2 minutes, 2–98% B for 2 minutes, 98% B for 2 minutes, 98–2% B for 2 minutes, and 2% B for 2 minutes. The orbitrap and FAIMS were operated in positive ion mode with a positive ion voltage of 1800V; with an ion transfer tube temperature of 270°C; using standard FAIMS resolution and compensation voltages of -50 and -65V, an inner electrode temperature of 100°C, and outer electrode temperature of 85°C with 4.6 ml/min carrier gas. Full scan spectra were acquired in profile mode at a resolution of 60,000, with a scan range of 400-1400 m/z, automatically determined maximum fill time, 300% AGC target, intensity threshold of 5×10^4, 2-5 charge state, and dynamic exclusion of 30 seconds with a cycle time of 1.5 seconds between master scans. MS2 spectra were generated with a HCD collision energy of 32 at a resolution of 45,000 using TurboTMT settings with a first mass at 110 m/z, an isolation window of 0.7 m/z, 200% AGC target, and 120 ms injection time.

1327 *Data analysis*

1328 Raw files were analyzed in Proteome Discoverer 2.4 (Thermo Fisher Scientific) to generate peak lists
1329 and protein and peptide IDs using Sequest HT as described for the SPARK 24h depletion proteome. The
1330 mass spectrometry proteomics datasets have been deposited to the ProteomeXchange Consortium via
1331 the PRIDE partner repository (Perez-Riverol et al., 2022) with the dataset identifier PXD044361.

1332

1333 Exported peptide and protein abundance files from Proteome Discoverer 2.4 were loaded into R
1334 (version 4.0.4). Ratios relative to the vehicle-treated timepoint were standardized by a modified Z-
1335 score. Peptides with the same site phosphorylations were matched across the PKG and SPARK
1336 depletion phosphoproteomes. We defined basally PKG-dependent phosphorylation sites as
1337 phosphopeptides that were down-regulated by more than two modified Z-scores when PKG was
1338 depleted for four hours. The distributions of all phosphopeptides identified in both the SPARK and PKG
1339 phosphoproteomes were compared with the distributions of PKG-dependent sites using a Kolmogorov-
1340 Smirnov test.

1341

1342 **PKA C3 depletion transcriptomics**

1343 *Parasite Harvest*

1344 TIR1/RH and PKA C3-mAID parasites were inoculated onto 15 cm dishes of HFF monolayers. After ~6-8
1345 hours, auxin was added to a final concentration of 500 uM. 24 hours after addition of auxin, dishes were
1346 placed on ice and washed twice with PBS containing 100 µg/mL cycloheximide. Lysis buffer (20 mM
1347 HEPES pH 7.5, 100 mM KCl, 5 mM $MgCl_2$, 1% Triton X-100, 2 mM DTT, 100 ug/mL cycloheximide, 500
1348 U/mL RNasIn Plus, and cOmplete, Mini Protease Inhibitor Cocktail) was added to the dish, the
1349 monolayer was scraped, and lysate was transferred to an eppendorf tube to incubate for 10 minutes on
1350 ice. Lysate was passed through a 27-gauge needle 6 times to facilitate lysis. Lysate was then
1351 centrifuged for 10 minutes at 1300xg, and the supernatant was flash-frozen and stored at -80℃ 3
1352 biological replicates of each strain were collected, and each sample was split into 2 technical replicates
1353 for downstream library preparation.

1354

1355 *RNA-sequencing and Analysis*

1356 Lysates were thawed on ice and a spike-in of D. melanogaster mRNA was added to each sample before
1357 Trizol extraction of RNA. RNA was polyA selected using the NEXTFLEX® Poly(A) Beads 2.0 Kit, and
1358 sequencing libraries were prepared according to the manufacturer's protocol with the NEXTFLEX®
1359 Rapid Directional RNA-Seq Kit 2.0 and NEXTFLEX® RNA-Seq 2.0 Unique Dual Index barcodes for
1360 multiplexing. Libraries were sequenced on one lane of a NovaSeq S4 with 150x150 paired-end reads at
1361 the Whitehead Institute Genome Technology Core.

1362

1363 Reads adapters were trimmed with TrimGalore (version 0.6.7). A metagenome of *T. gondii, H. sapiens,*
1364 and *D. melanogaster* was prepared using STAR (version 2.7.1a) from genome FASTA files and gff
1365 annotation files downloaded from VEuPathDb Release 59. Trimmed reads were aligned to the
1366 metagenome using STAR, and mapped reads were quantified using featureCounts (version 1.6.2).

Differential expression analysis of *T. gondii* genes with at least 10 reads across all samples was performed using DESeq2 (version 1.30.1) in R.

SPARKEL phylogenetic analysis

SPARKEL (TGGT1_291010) homologs were identified from representative apicomplexan and metazoan (outgroup) genomes. The Skp1 domain sequences were extracted based on annotation with Interpro domain IPR011333 or PFam domain PF03931. Domain alignment was performed in MEGA using ClustalW with a gap opening penalty of 3, gap extension penalty of 1.8, and remaining default parameters. A Neighbor-Joining Tree was generated and visualized with MEGA using the bootstrap method with 1000 replications as a test of phylogeny and a Jones-Taylor-Thornton model and remaining default parameters.

ACKNOWLEDGEMENTS

We thank Faye Harling for assistance with cell culture, Emily Shortt for the CDPK1-mNG-mAID strain, L. David Sibley for ALD1 antibody and RH TIR1 strain, Dominique Soldati-Favre and Drew Etheridge for the GAP45 antibodies, Marc-Jan Gubbels for the TUB1 antibody, Kevin Brown for the PKG-AID strain, and members of the Lourido laboratory for helpful discussions. Aditi Shukla developed the BFD1 knockout strategy. The Whitehead Institute Genome Technology Core assisted in nucleic acid sequencing, and the Whitehead Flow Cytometry Core assisted with sorting of fluorescent parasite strains. This work relied extensively on VEuPathDB.org and we thank all contributors to this resource. This research was supported by funds from R01AI144369 to S.L. and a National Science Foundation Graduate Research Fellowship to A.L.H. (174530) and T.A.S. (2018259980).

AUTHOR DETAILS

Alice L Herneisen
Whitehead Institute for Biomedical Research, Cambridge, MA, USA
Biology Department, Massachusetts Institute of Technology, Cambridge, MA, USA
Contribution: Conceptualization, Methodology, Validation, Formal analysis, Investigation, Writing - original draft, Visualization
Competing interests: No competing interests declared
ORCID: 0000-0003-3368-0893

Michelle L Peters
Whitehead Institute for Biomedical Research, Cambridge, MA, USA
Biology Department, Massachusetts Institute of Technology, Cambridge, MA, USA
Contribution: Methodology, Formal analysis, Investigation
Competing interests: No competing interests declared
ORCID: 0000-0002-2919-2523

Tyler A Smith

Whitehead Institute for Biomedical Research, Cambridge, MA, USA
Biology Department, Massachusetts Institute of Technology, Cambridge, MA, USA
Contribution: Resources, Investigation
Competing interests: No competing interests declared
ORCID: 0000-0002-3399-4043

Sebastian Lourido
Whitehead Institute for Biomedical Research, Cambridge, MA, USA
Biology Department, Massachusetts Institute of Technology, Cambridge, MA, USA
Contribution: Conceptualization, Resources, Supervision, Funding acquisition, Methodology, Writing - review and editing
For correspondence: lourido@wi.mit.edu
Competing interests: Reviewing editor, eLife
ORCID: 0000-0002-5237-1095

COMPETING INTERESTS

The authors declare no additional competing interests.

SUPPLEMENTARY FILES

Supplementary File 1. Protein quantification and statistical tests for immunoprecipitation-mass spectrometry experiments (SPARK, SPARKEL, and PKA C3-tagged strains), exported from the Proteome Discoverer 2.4 software.

Supplementary File 2. Protein quantification and statistical tests for TurboID mass spectrometry experiments (SPARKEL and SPARK TurboID-tagged strains), exported from the Proteome Discoverer 2.4 software.

Supplementary File 3. Protein and peptide quantification and statistical tests for SPARK, SPARKEL, and PKA C3 depletion proteomes, exported from the Proteome Discoverer 2.4 software.

Supplementary File 4. Peptide ratios quantified in the PKA R-AID, and PKG-AID, and SPARK-AID depletion phosphoproteomes. Ratios are reported relative to the vehicle-treated sample within each experiment. Modified Z-scores were calculated by standardizing each value with respect to the median and median absolute deviation within each ratio.

Supplementary File 5. Oligonucleotides and DNA sequences used in this study.

SOURCE DATA

Figure 2—source data 1. This file contains source data that was used to generate the blot in Figure 2B. V5, LICOR.

Figure 2—source data 2. This file contains source data that was used to generate the blot in Figure 2B. TUB1, LICOR.

Figure 2—source data 3. This file contains source data that was used to generate the blot in Figure 2C. V5, LICOR.

Figure 2—source data 4. This file contains source data that was used to generate the blot in Figure 2C. CDPK1, LICOR.

Figure 2—figure supplement 1 source data 1. This file contains source data that was used to generate the blot in Figure 2—figure supplement 1B. V5, LICOR.

Figure 2—figure supplement 1 source data 2. This file contains source data that was used to generate the blot in Figure 2—figure supplement 1B. ALD1, LICOR.

Figure 6—source data 1. This file contains source data that was used to generate the blot in Figure 6D. V5, LICOR.

Figure 6—source data 2. This file contains source data that was used to generate the blot in Figure 6D. ALD1, LICOR.

Figure 7—source data 1. This file contains source data that was used to generate the blot in Figure 7D. mNG, LICOR.

Figure 7—source data 2. This file contains source data that was used to generate the blot in Figure 7D. V5, LICOR.

Figure 7—source data 3. This file contains source data that was used to generate the blot in Figure 7D. ALD1, LICOR.

MATERIALS AVAILABILITY STATEMENT

All mass spectrometry proteomics data have been deposited to the ProteomeXchange Consortium via the PRIDE partner repository with the accession numbers PXD039896, PXD039919, PXD039922, PXD039979, PXD039983, PXD039985, PXD039986, PXD040598, PXD040602, PXD040635, PXD042989, PXD044361, PXD044398. Sequences of cloning vectors generated for this study are listed in **Supplementary File 5**. Strains and plasmids generated for this study can be obtained by emailing the corresponding author.

REFERENCES

Alam MM, Solyakov L, Bottrill AR, Flueck C, Siddiqui FA, Singh S, Mistry S, Viskaduraki M, Lee K, Hopp CS, Chitnis CE, Doerig C, Moon RW, Green JL, Holder AA, Baker DA, Tobin AB. 2015. Phosphoproteomics reveals malaria parasite Protein Kinase G as a signalling hub regulating egress and invasion. *Nat Commun* **6**:7285.

Anderson MZ, Brewer J, Singh U, Boothroyd JC. 2009. A pseudouridine synthase homologue is critical to cellular differentiation in Toxoplasma gondii. *Eukaryot Cell* **8**:398–409.

Antunes AV, Shahinas M, Swale C, Farhat DC, Ramakrishnan C, Bruley C, Cannella D, Corrao C, Cout Y, Hehl AB, Bougdour A, Coppens I, Hakimi M-A. 2023. In vitro production of cat-restricted Toxoplasma pre-sexual stages by epigenetic reprogramming. *bioRxiv*.

1490 doi:10.1101/2023.01.16.524187
1491 Augusto L, Wek RC, Sullivan WJ Jr. 2020. Host sensing and signal transduction during Toxoplasma
1492 stage conversion. *Mol Microbiol*. doi:10.1111/mmi.14634
1493 Back PS, Moon AS, Pasquarelli RR, Bell HN, Torres JA, Chen AL, Sha J, Vashisht AA, Wohlschlegel JA,
1494 Bradley PJ. 2023. IMC29 Plays an Important Role in Toxoplasma Endodyogeny and Reveals New
1495 Components of the Daughter-Enriched IMC Proteome. *MBio* **14**:e0304222.
1496 Baker DA, Stewart LB, Large JM, Bowyer PW, Ansell KH, Jiménez-Díaz MB, El Bakkouri M, Birchall K,
1497 Dechering KJ, Bouloc NS, Coombs PJ, Whalley D, Harding DJ, Smiljanic-Hurley E, Wheldon MC,
1498 Walker EM, Dessens JT, Lafuente MJ, Sanz LM, Gamo F-J, Ferrer SB, Hui R, Bousema T, Angulo-
1499 Barturén I, Merritt AT, Croft SL, Gutteridge WE, Kettleborough CA, Osborne SA. 2017. A potent
1500 series targeting the malarial cGMP-dependent protein kinase clears infection and blocks
1501 transmission. *Nat Commun* **8**:430.
1502 Bakkouri ME, Kouidmi I, Wernimont AK, Amani M, Hutchinson A, Loppnau P, Kim JJ, Flueck C, Walker
1503 JR, Seitova A, Senisterra G, Kakihara Y, Kim C, Blackman MJ, Calmettes C, Baker DA, Hui R. 2019.
1504 Structures of the cGMP-dependent protein kinase in malaria parasites reveal a unique structural
1505 relay mechanism for activation. *Proceedings of the National Academy of Sciences* **116**:14164–14173.
1506 Balestra AC, Koussis K, Klages N, Howell SA, Flynn HR, Bantscheff M, Pasquarello C, Perrin AJ, Brusini
1507 L, Arboit P, Sanz O, Castaño LP-B, Withers-Martinez C, Hainard A, Ghidelli-Disse S, Snijders AP,
1508 Baker DA, Blackman MJ, Brochet M. 2021. Ca2+ signals critical for egress and gametogenesis in
1509 malaria parasites depend on a multipass membrane protein that interacts with PKG. *Sci Adv* **7**.
1510 doi:10.1126/sciadv.abe5396
1511 Behnke MS, Radke JB, Smith AT, Sullivan WJ Jr, White MW. 2008. The transcription of bradyzoite
1512 genes in Toxoplasma gondii is controlled by autonomous promoter elements. *Mol Microbiol*
1513 **68**:1502–1518.
1514 Bekker-Jensen DB, Martínez-Val A, Steigerwald S, Rüther P, Fort KL, Arrey TN, Harder A, Makarov A,
1515 Olsen JV. 2020. A Compact Quadrupole-Orbitrap Mass Spectrometer with FAIMS Interface
1516 Improves Proteome Coverage in Short LC Gradients. *Mol Cell Proteomics* **19**:716–729.
1517 Bisio H, Lunghi M, Brochet M, Soldati-Favre D. 2019. Phosphatidic acid governs natural egress in
1518 Toxoplasma gondii via a guanylate cyclase receptor platform. *Nat Microbiol* **4**:420–428.
1519 Blader IJ, Coleman BI, Chen C-T, Gubbels M-J. 2015. Lytic Cycle of Toxoplasma gondii : 15 Years Later.
1520 *Annu Rev Microbiol* **69**:463–485.
1521 Branon TC, Bosch JA, Sanchez AD, Udeshi ND, Svinkina T, Carr SA, Feldman JL, Perrimon N, Ting AY.
1522 2018. Efficient proximity labeling in living cells and organisms with TurboID. *Nat Biotechnol*
1523 **36**:880–887.
1524 Braun L, Brenier-Pinchart M-P, Yogavel M, Curt-Varesano A, Curt-Bertini R-L, Hussain T, Kieffer-
1525 Jaquinod S, Coute Y, Pelloux H, Tardieux I, Sharma A, Belrhali H, Bougdour A, Hakimi M-A. 2013. A
1526 Toxoplasma dense granule protein, GRA24, modulates the early immune response to infection by
1527 promoting a direct and sustained host p38 MAPK activation. *J Exp Med* **210**:2071–2086.
1528 Brochet M, Collins MO, Smith TK, Thompson E, Sebastian S, Volkmann K, Schwach F, Chappell L,
1529 Gomes AR, Berriman M, Rayner JC, Baker DA, Choudhary J, Billker O. 2014. Phosphoinositide
1530 Metabolism Links cGMP-Dependent Protein Kinase G to Essential Ca2+ Signals at Key Decision
1531 Points in the Life Cycle of Malaria Parasites. *PLoS Biol* **12**:e1001806.
1532 Brown KM, Long S, Sibley LD. 2017. Plasma Membrane Association by N- Acylation Governs PKG
1533 Function in Toxoplasma gondii. *MBio* **8**:1–14.
1534 Brown KM, Lourido S, Sibley LD. 2016. Serum Albumin Stimulates Protein Kinase G-dependent
1535 Microneme Secretion in Toxoplasma gondii. *J Biol Chem* **291**:9554–9565.
1536 Brown KM, Tonkin CJ, Billker O, Sibley LD. 2020. Chapter 13 - Calcium and cyclic nucleotide signaling
1537 networks in Toxoplasma gondii In: Weiss LM, Kim K, editors. Toxoplasma Gondii (Third Edition).

1538 Academic Press. pp. 577–605.
1539 Chan AW, Broncel M, Haseley NR, Chakladar S, Andree E, Herneisen AL, Shortt E, Treeck M, Lourido S.
1540 2023. Analysis of CDPK1 targets identifies a trafficking adaptor complex that regulates microneme
1541 exocytosis in Toxoplasma. *bioRxiv*. doi:10.1101/2023.01.11.523553
1542 Chasen NM, Stasic AJ, Asady B, Coppens I, Moreno SNJ. 2019. The Vacuolar Zinc Transporter TgZnT
1543 Protects Toxoplasma gondii from Zinc Toxicity. *mSphere* **4**. doi:10.1128/mSphere.00086-19
1544 Chen AL, Kim EW, Toh JY, Vashisht AA, Rashoff AQ, Van C, Huang AS, Moon AS, Bell HN, Bentolila LA,
1545 Wohlschlegel JA, Bradley PJ. 2015. Novel components of the Toxoplasma inner membrane
1546 complex revealed by BioID. *MBio* **6**:e02357–14.
1547 Chen AL, Moon AS, Bell HN, Huang AS, Vashisht AA, Toh JY, Lin AH, Nadipuram SM, Kim EW, Choi CP,
1548 Wohlschlegel JA, Bradley PJ. 2017. Novel insights into the composition and function of the
1549 Toxoplasma IMC sutures. *Cell Microbiol* **19**. doi:10.1111/cmi.12678
1550 Cheng X, Ma Y, Moore M, Hemmings BA, Taylor SS. 1998. Phosphorylation and activation of cAMP-
1551 dependent protein kinase by phosphoinositide-dependent protein kinase. *Proc Natl Acad Sci U S A*
1552 **95**:9849–9854.
1553 Cygan AM, Jean Beltran PM, Mendoza AG, Branon TC, Ting AY, Carr SA, Boothroyd JC. 2021.
1554 Proximity-Labeling Reveals Novel Host and Parasite Proteins at the Toxoplasma Parasitophorous
1555 Vacuole Membrane. *MBio* **12**:e0026021.
1556 Donald RGK, Allocco J, Singh SB, Nare B, Salowe SP, Wiltsie J, Liberator PA. 2002. Toxoplasma gondii
1557 cyclic GMP-dependent kinase: chemotherapeutic targeting of an essential parasite protein kinase.
1558 *Eukaryot Cell* **1**:317–328.
1559 Donald RGK, Zhong T, Wiersma H, Nare B, Yao D, Lee A, Allocco J, Liberator PA. 2006. Anticoccidial
1560 kinase inhibitors: Identification of protein kinase targets secondary to cGMP-dependent protein
1561 kinase. *Mol Biochem Parasitol* **149**:86–98.
1562 Dos Santos Pacheco N, Tosetti N, Krishnan A, Haase R, Maco B, Suarez C, Ren B, Soldati-Favre D. 2021.
1563 Revisiting the Role of Toxoplasma gondii ERK7 in the Maintenance and Stability of the Apical
1564 Complex. *MBio* **12**:e0205721.
1565 Dubey JP, Shen SK, Kwok OC, Frenkel JK. 1999. Infection and immunity with the RH strain of
1566 Toxoplasma gondii in rats and mice. *J Parasitol* **85**:657–662.
1567 Engelberg K, Bechtel T, Michaud C, Weerapana E, Gubbels M-J. 2022. Proteomic characterization of
1568 the Toxoplasma gondii cytokinesis machinery portrays an expanded hierarchy of its assembly and
1569 function. *Nat Commun* **13**:4644.
1570 Engelberg K, Chen C-T, Bechtel T, Sánchez Guzmán V, Drozda AA, Chavan S, Weerapana E, Gubbels M-
1571 J. 2020. The apical annuli of Toxoplasma gondii are composed of coiled-coil and signalling proteins
1572 embedded in the inner membrane complex sutures. *Cell Microbiol* **22**:e13112.
1573 Fang H, Gomes AR, Klages N, Pino P, Maco B, Walker EM, Zenonos ZA, Angrisano F, Baum J, Doerig C,
1574 Baker DA, Billker O, Brochet M. 2018. Epistasis studies reveal redundancy among calcium-
1575 dependent protein kinases in motility and invasion of malaria parasites. *Nat Commun* **9**:4248.
1576 Farhat DC, Bowler MW, Communie G, Pontier D, Belmudes L, Mas C, Corrao C, Couté Y, Bougdour A,
1577 Lagrange T, Hakimi M-A, Swale C. 2021. A plant-like mechanism coupling m6A reading to
1578 polyadenylation safeguards transcriptome integrity and developmental gene partitioning in
1579 Toxoplasma. *Elife* **10**. doi:10.7554/eLife.68312
1580 Ferrarini MG, Nisimura LM, Girard RMBM, Alencar MB, Fragoso MSI, Araújo-Silva CA, Veiga A de A,
1581 Abud APR, Nardelli SC, Vommaro RC, Silber AM, France-Sagot M, Ávila AR. 2021. Dichloroacetate
1582 and Pyruvate Metabolism: Pyruvate Dehydrogenase Kinases as Targets Worth Investigating for
1583 Effective Therapy of Toxoplasmosis. *mSphere* **6**. doi:10.1128/mSphere.01002-20
1584 Flueck C, Drought LG, Jones A, Patel A, Perrin J, Walker EM, Nofal SD, Snijders AP, Blackman J, Baker
1585 DA, Perrin AJ, Walker EM, Nofal SD, Snijders AP, Blackman MJ, Baker DA. 2019.

1586 Phosphodiesterase beta is the master regulator of cAMP signalling during malaria parasite
1587 invasion. *PLoS Biol* **17**:1–32.
1588 Frénal K, Jacot D, Hammoudi P-M, Graindorge A, Maco B, Soldati-Favre D. 2017. Myosin-dependent
1589 cell-cell communication controls synchronicity of division in acute and chronic stages of
1590 Toxoplasma gondii. *Nat Commun* **8**:15710.
1591 Frénal K, Tay CL, Mueller C, Bushell ES, Jia Y, Graindorge A, Billker O, Rayner JC, Soldati-Favre D. 2013.
1592 Global analysis of apicomplexan protein S-acyl transferases reveals an enzyme essential for
1593 invasion. *Traffic* **14**:895–911.
1594 Fritz HM, Bowyer PW, Bogyo M, Conrad PA, Boothroyd JC. 2012. Proteomic analysis of fractionated
1595 Toxoplasma oocysts reveals clues to their environmental resistance. *PLoS One* **7**:e29955.
1596 Fu Y, Brown KM, Jones NG, Moreno SN, Sibley LD. 2021. Toxoplasma bradyzoites exhibit physiological
1597 plasticity of calcium and energy stores controlling motility and egress. *Elife* **10**.
1598 doi:10.7554/eLife.73011
1599 Gagliardi PA, Puliafito A, Primo L. 2018. PDK1: At the crossroad of cancer signaling pathways. *Semin*
1600 *Cancer Biol* **48**:27–35.
1601 Gissot M, Walker R, Delhaye S, Alayi TD, Huot L, Hot D, Callebaut I, Schaeffer-Reiss C, Van Dorsselaer
1602 A, Tomavo S. 2013. Toxoplasma gondii Alba proteins are involved in translational control of gene
1603 expression. *J Mol Biol* **425**:1287–1301.
1604 Harding CR, Sidik SM, Petrova B, Gnädig NF, Okombo J, Herneisen AL, Ward KE, Markus BM, Boydston
1605 EA, Fidock DA, Lourido S. 2020. Genetic screens reveal a central role for heme metabolism in
1606 artemisinin susceptibility. *Nat Commun* **11**:4813.
1607 Herneisen AL, Li Z-H, Chan AW, Moreno SNJ, Lourido S. 2022. Temporal and thermal profiling of the
1608 Toxoplasma proteome implicates parasite Protein Phosphatase 1 in the regulation of Ca2+-
1609 responsive pathways. *Elife* **11**. doi:10.7554/eLife.80336
1610 Hitz E, Wiedemar N, Passecker A, Graça BAS, Scheurer C, Wittlin S, Brancucci NMB, Vakonakis I, Mäser
1611 P, Voss TS. 2021. The 3-phosphoinositide-dependent protein kinase 1 is an essential upstream
1612 activator of protein kinase A in malaria parasites. *PLoS Biol* **19**:e3001483.
1613 Holmes MJ, Bastos MS, Dey V, Severo V, Wek RC, Sullivan WJ. 2023. mRNA cap-binding protein eIF4E1
1614 is a novel regulator of Toxoplasma gondii latency. *bioRxiv*. doi:10.1101/2023.10.09.561274
1615 Huet D, Rajendran E, van Dooren GG, Lourido S, Van Dooren GG, Lourido S. 2018. Identification of
1616 cryptic subunits from an apicomplexan ATP synthase. *Elife* **e38097**:1–24.
1617 Huynh MH, Carruthers VB. 2009. Tagging of endogenous genes in a Toxoplasma gondii strain lacking
1618 Ku80. *Eukaryot Cell* **8**:530–539.
1619 Hyman LE, Kwon E, Ghosh S, McGee J, Chachulska AMB, Jackson T, Baricos WH. 2002. Binding to
1620 Elongin C inhibits degradation of interacting proteins in yeast. *J Biol Chem* **277**:15586–15591.
1621 Jiang Q, Zheng N, Bu L, Zhang X, Zhang X, Wu Y, Su Y, Wang L, Zhang X, Ren S, Dai X, Wu D, Xie W,
1622 Wei W, Zhu Y, Guo J. 2021. SPOP-mediated ubiquitination and degradation of PDK1 suppresses
1623 AKT kinase activity and oncogenic functions. *Mol Cancer* **20**:100.
1624 Jia Y, Marq J, Bisio H, Jacot D, Mueller C, Yu L, Choudhary J, Brochet M, Soldati-Favre D. 2017. Crosstalk
1625 between PKA and PKG controls pH-dependent host cell egress of Toxoplasma gondii. *EMBO J*
1626 **36**:e201796794.
1627 Jones JL, Parise ME, Fiore AE. 2014. Neglected parasitic infections in the United States: toxoplasmosis.
1628 *Am J Trop Med Hyg* **90**:794–799.
1629 Joyce BR, Tampaki Z, Kim K, Wek RC, Sullivan WJ Jr. 2013. The unfolded protein response in the
1630 protozoan parasite Toxoplasma gondii features translational and transcriptional control. *Eukaryot*
1631 *Cell* **12**:979–989.
1632 Koreny L, Mercado-Saavedra BN, Klinger CM, Barylyuk K, Butterworth S, Hirst J, Rivera-Cuevas Y,
1633 Zaccai NR, Holzer VJC, Klingl A, Dacks JB, Carruthers VB, Robinson MS, Gras S, Waller RF. 2023.

1634 Stable endocytic structures navigate the complex pellicle of apicomplexan parasites. *Nat Commun*
1635 **14**:2167.
1636 Krishnamurthy S, Maru P, Wang Y, Bitew MA, Mukhopadhyay D, Yamaryo-Botté Y, Paredes-Santos TC,
1637 Sangaré LO, Swale C, Botté CY, Saeij JPJ. 2023. CRISPR Screens Identify Toxoplasma Genes That
1638 Determine Parasite Fitness in Interferon Gamma-Stimulated Human Cells. *MBio* **14**:e0006023.
1639 Laplante M, Sabatini DM. 2012. mTOR signaling in growth control and disease. *Cell* **149**:274–293.
1640 Levina A, Fleming KD, Burke JE, Leonard TA. 2022. Activation of the essential kinase PDK1 by
1641 phosphoinositide-driven trans-autophosphorylation. *Nat Commun* **13**:1874.
1642 Liang Q-L, Nie L-B, Li T-T, Elsheikha HM, Sun L-X, Zhang Z-W, Zhao D-Y, Zhu X-Q, Wang J-L. 2021.
1643 Functional Characterization of 17 Protein Serine/Threonine Phosphatases in Toxoplasma gondii
1644 Using CRISPR-Cas9 System. *Front Cell Dev Biol* **9**:738794.
1645 Licon MH, Giuliano CJ, Chan AW, Chakladar S, Eberhard JN, Shallberg LA, Chandrasekaran S, Waldman
1646 BS, Koshy AA, Hunter CA, Lourido S. 2023. A positive feedback loop controls Toxoplasma chronic
1647 differentiation. *Nat Microbiol* **8**:889–904.
1648 Liu J, Wetzel L, Zhang Y, Nagayasu E, Ems-McClung S, Florens L, Hu K. 2013. Novel thioredoxin-like
1649 proteins are components of a protein complex coating the cortical microtubules of Toxoplasma
1650 gondii. *Eukaryot Cell* **12**:1588–1599.
1651 Liu M, Miao J, Liu T, Sullivan WJ Jr, Cui L, Chen X. 2014. Characterization of TgPuf1, a member of the
1652 Puf family RNA-binding proteins from Toxoplasma gondii. *Parasit Vectors* **7**:141.
1653 Lockyer EJ, Torelli F, Butterworth S, Song O-R, Howell S, Weston A, East P, Treeck M. 2023. A
1654 heterotrimeric complex of Toxoplasma proteins promotes parasite survival in interferon gamma-
1655 stimulated human cells. *PLoS Biol* **21**:e3002202.
1656 Long S, Anthony B, Drewry LL, Sibley LD. 2017. A conserved ankyrin repeat-containing protein
1657 regulates conoid stability, motility and cell invasion in Toxoplasma gondii. *Nat Commun* **8**:2236.
1658 Lourido S. 2019. Toxoplasma gondii. *Trends in Parasitology*. doi:10.1016/j.pt.2019.07.001
1659 Lourido S, Tang K, Sibley LD. 2012. Distinct signalling pathways control Toxoplasma egress and host-
1660 cell invasion. *EMBO J* **31**:4524–4534.
1661 Markus BM, Waldman BS, Lorenzi HA, Lourido S. 2020. High-Resolution Mapping of Transcription
1662 Initiation in the Asexual Stages of Toxoplasma gondii. *Front Cell Infect Microbiol* **10**:617998.
1663 Marsilia C, Batra M, Pokrovskaya ID, Wang C, Chaput D, Naumova DA, Lupashin VV, Suvorova ES.
1664 2023. Essential role of the Conserved Oligomeric Golgi complex in Toxoplasma gondii. *bioRxiv*.
1665 doi:10.1101/2023.05.30.542952
1666 Masters TA, Calleja V, Armoogum DA, Marsh RJ, Applebee CJ, Laguerre M, Bain AJ, Larijani B. 2010.
1667 Regulation of 3-phosphoinositide-dependent protein kinase 1 activity by homodimerization in live
1668 cells. *Sci Signal* **3**:ra78.
1669 Moore MJ, Kanter JR, Jones KC, Taylor SS. 2002. Phosphorylation of the catalytic subunit of protein
1670 kinase A. Autophosphorylation versus phosphorylation by phosphoinositide-dependent kinase-1. *J*
1671 *Biol Chem* **277**:47878–47884.
1672 Mora A, Komander D, van Aalten DMF, Alessi DR. 2004. PDK1, the master regulator of AGC kinase
1673 signal transduction. *Semin Cell Dev Biol* **15**:161–170.
1674 Moss WJ, Patterson CE, Jochmans AK, Brown KM. 2022. Functional Analysis of the Expanded
1675 Phosphodiesterase Gene Family in Toxoplasma gondii Tachyzoites. *mSphere* **7**:e0079321.
1676 Nadipuram SM, Kim EW, Vashisht AA, Lin AH, Bell HN, Coppens I, Wohlschlegel JA, Bradley PJ. 2016. In
1677 Vivo Biotinylation of the Toxoplasma Parasitophorous Vacuole Reveals Novel Dense Granule
1678 Proteins Important for Parasite Growth and Pathogenesis. *MBio* **7**. doi:10.1128/mBio.00808-16
1679 Nadipuram SM, Thind AC, Rayatpisheh S, Wohlschlegel JA, Bradley PJ. 2020. Proximity biotinylation
1680 reveals novel secreted dense granule proteins of Toxoplasma gondii bradyzoites. *PLoS One*
1681 **15**:e0232552.

1682 Newton AC. 2010. Protein kinase C: poised to signal. *Am J Physiol Endocrinol Metab* **298**:E395–402.
1683 Nofal SD, Dominicus C, Broncel M, Katris NJ, Flynn HR, Arrizabalaga G, Botté CY, Invergo BM, Treeck
1684 M. 2022. A positive feedback loop mediates crosstalk between calcium, cyclic nucleotide and lipid
1685 signalling in calcium-induced Toxoplasma gondii egress. *PLoS Pathog* **18**:e1010901.
1686 Nyonda MA, Kloehn J, Sosnowski P, Krishnan A, Lentini G, Maco B, Marq J-B, Hannich JT, Hopfgartner
1687 G, Soldati-Favre D. 2022. Ceramide biosynthesis is critical for establishment of the intracellular
1688 niche of Toxoplasma gondii. *Cell Rep* **40**:111224.
1689 Pace DA, Moreno SNJ, Lourido S. 2020. Calcium storage and homeostasis in Toxoplasma gondii.
1690 *Toxoplasma gondii*. doi:10.1016/b978-0-12-815041-2.00012-8
1691 Parmley SF, Yang S, Harth G, Sibley LD, Sucharczuk A, Remington JS. 1994. Molecular characterization
1692 of a 65-kilodalton Toxoplasma gondii antigen expressed abundantly in the matrix of tissue cysts.
1693 *Mol Biochem Parasitol* **66**:283–296.
1694 Patel A, Perrin AJ, Flynn HR, Bisson C, Withers-Martinez C, Treeck M, Flueck C, Nicastro G, Martin SR,
1695 Ramos A, Gilberger TW, Snijders AP, Blackman MJ, Baker DA. 2019. Cyclic AMP signalling controls
1696 key components of malaria parasite host cell invasion machinery. *PLoS Biol* **17**:e3000264.
1697 Paul AS, Saha S, Engelberg K, Jiang RHY, Coleman BI, Kosber AL, Chen C-T, Ganter M, Espy N,
1698 Gilberger TW, Gubbels M-J, Duraisingh MT. 2015. Parasite Calcineurin Regulates Host Cell
1699 Recognition and Attachment by Apicomplexans. *Cell Host Microbe* **18**:49–60.
1700 Pearce LR, Komander D, Alessi DR. 2010. The nuts and bolts of AGC protein kinases. *Nat Rev Mol Cell*
1701 *Biol* **11**:9–22.
1702 Perez-Riverol Y, Bai J, Bandla C, García-Seisdedos D, Hewapathirana S, Kamatchinathan S, Kundu DJ,
1703 Prakash A, Frericks-Zipper A, Eisenacher M, Walzer M, Wang S, Brazma A, Vizcaíno JA. 2022. The
1704 PRIDE database resources in 2022: a hub for mass spectrometry-based proteomics evidences.
1705 *Nucleic Acids Res* **50**:D543–D552.
1706 Quan JJ, Nikolov LA, Sha J, Wohlschlegel JA, Bradley PJ. 2023. Toxoplasma gondii encodes an array of
1707 TBC-domain containing proteins including an essential regulator that targets Rab2 in the secretory
1708 pathway. *bioRxiv*. doi:10.1101/2023.05.28.542599
1709 Rademacher EH, Offringa R. 2012. Evolutionary Adaptations of Plant AGC Kinases: From Light
1710 Signaling to Cell Polarity Regulation. *Front Plant Sci* **3**:250.
1711 Radke JR, Guerini MN, Jerome M, White MW. 2003. A change in the premitotic period of the cell cycle is
1712 associated with bradyzoite differentiation in Toxoplasma gondii. *Mol Biochem Parasitol* **131**:119–
1713 127.
1714 Raimondi C, Falasca M. 2011. Targeting PDK1 in cancer. *Curr Med Chem* **18**:2763–2769.
1715 Ramakrishnan C, Maier S, Walker RA, Rehrauer H, Joekel DE, Winiger RR, Basso WU, Grigg ME, Hehl
1716 AB, Deplazes P, Smith NC. 2019. An experimental genetically attenuated live vaccine to prevent
1717 transmission of Toxoplasma gondii by cats. *Sci Rep* **9**:1474.
1718 Roumégous C, Abou Hammoud A, Fuster D, Dupuy J-W, Blancard C, Salin B, Robinson DR, Renesto P,
1719 Tardieux I, Frénal K. 2022. Identification of new components of the basal pole of *Toxoplasma gondii*
1720 provides novel insights into its molecular organization and functions. *Front Cell Infect Microbiol*
1721 **12**:1010038.
1722 Schwarz JA, Fouts AE, Cummings CA, Ferguson DJP, Boothroyd JC. 2005. A novel rhoptry protein in
1723 Toxoplasma gondii bradyzoites and merozoites. *Mol Biochem Parasitol* **144**:159–166.
1724 Scrucca L, Fop M, Murphy TB, Raftery AE. 2016. mclust 5: Clustering, Classification and Density
1725 Estimation Using Gaussian Finite Mixture Models. *R J* **8**:289–317.
1726 Shortt E, Hackett CG, Stadler RV, Ward GE, Lourido S. 2022. CDPK2A and CDPK1 form a signaling
1727 module upstream of Toxoplasma motility. *bioRxiv*. doi:10.1101/2022.07.19.500742
1728 Sidik SM, Huet D, Ganesan SM, Huynh M-H, Wang T, Nasamu AS, Thiru P, Saeij JPJ, Carruthers VB,
1729 Niles JC, Lourido S. 2016a. A Genome-wide CRISPR Screen in Toxoplasma Identifies Essential

1730 Apicomplexan Genes. *Cell* **166**:1423–1435.e12.
1731 Sidik SM, Triana MAH, Paul AS, El Bakkouri M, Hackett CG, Tran F, Westwood NJ, Hui R, Zuercher WJ,
1732 Duraisingh MT, Moreno SNJ, Lourido S. 2016b. Using a genetically encoded sensor to identify
1733 inhibitors of toxoplasma gondii Ca2+signaling. *J Biol Chem* **291**:9566–9580.
1734 Sinai AP, Knoll LJ, Weiss LM. 2020. Chapter 18 - Bradyzoite and sexual stage development In: Weiss
1735 LM, Kim K, editors. Toxoplasma Gondii (Third Edition). Academic Press. pp. 807–857.
1736 Singer M, Simon K, Forné I, Meissner M. 2023. A central CRMP complex essential for invasion in
1737 Toxoplasma gondii. *PLoS Biol* **21**:e3001937.
1738 Smith TA, Lopez-Perez GS, Herneisen AL, Shortt E, Lourido S. 2022. Screening the Toxoplasma kinome
1739 with high-throughput tagging identifies a regulator of invasion and egress. *Nat Microbiol*.
1740 doi:10.1038/s41564-022-01104-0
1741 Sparvoli D, Delabre J, Penarete-Vargas DM, Kumar Mageswaran S, Tsypin LM, Heckendorn J, Theveny
1742 L, Maynadier M, Mendonça Cova M, Berry-Sterkers L, Guérin A, Dubremetz J-F, Urbach S,
1743 Striepen B, Turkewitz AP, Chang Y-W, Lebrun M. 2022. An apical membrane complex for
1744 triggering rhoptry exocytosis and invasion in Toxoplasma. *EMBO J* **41**:e111158.
1745 Sugi T, Ma YF, Tomita T, Murakoshi F, Eaton MS, Yakubu R, Han B, Tu V, Kato K, Kawazu S-I, Gupta N,
1746 Suvorova ES, White MW, Kim K, Weiss LM. 2016. Toxoplasma gondii Cyclic AMP-Dependent
1747 Protein Kinase Subunit 3 Is Involved in the Switch from Tachyzoite to Bradyzoite Development.
1748 *MBio* **7**:e00755–16.
1749 Sullivan WJ Jr, Monroy MA, Bohne W, Nallani KC, Chrivia J, Yaciuk P, Smith CK 2nd, Queener SF. 2003.
1750 Molecular cloning and characterization of an SRCAP chromatin remodeling homologue in
1751 Toxoplasma gondii. *Parasitol Res* **90**:1–8.
1752 Swale C, Bellini V, Bowler MW, Flore N, Brenier-Pinchart M-P, Cannella D, Belmudes L, Mas C, Couté Y,
1753 Laurent F, Scherf A, Bougdour A, Hakimi M-A. 2022. Altiratinib blocks *Toxoplasma gondii* and
1754 *Plasmodium falciparum* development by selectively targeting a spliceosome kinase. *Sci Transl Med*
1755 **14**:eabn3231.
1756 Talevich E, Mirza A, Kannan N. 2011. Structural and evolutionary divergence of eukaryotic protein
1757 kinases in Apicomplexa. *BMC Evol Biol* **11**:321.
1758 Tomita T, Bzik DJ, Ma YF, Fox BA, Markillie LM, Taylor RC, Kim K, Weiss LM. 2013. The Toxoplasma
1759 gondii cyst wall protein CST1 is critical for cyst wall integrity and promotes bradyzoite persistence.
1760 *PLoS Pathog* **9**:e1003823.
1761 Tosetti N, Dos Santos Pacheco N, Bertiaux E, Maco B, Bournonville L, Hamel V, Guichard P, Soldati-
1762 Favre D. 2020. Essential function of the alveolin network in the subpellicular microtubules and
1763 conoid assembly in Toxoplasma gondii. *Elife* **9**. doi:10.7554/eLife.56635
1764 Tran JQ, Li C, Chyan A, Chung L, Morrissette NS. 2012. SPM1 stabilizes subpellicular microtubules in
1765 Toxoplasma gondii. *Eukaryot Cell* **11**:206–216.
1766 Tsai C-F, Hsu C-C, Hung J-N, Wang Y-T, Choong W-K, Zeng M-Y, Lin P-Y, Hong R-W, Sung T-Y, Chen Y-
1767 J. 2014. Sequential phosphoproteomic enrichment through complementary metal-directed
1768 immobilized metal ion affinity chromatography. *Anal Chem* **86**:685–693.
1769 Tu V, Tomita T, Sugi T, Mayoral J, Han B, Yakubu RR, Williams T, Horta A, Ma Y, Weiss LM. 2020. The
1770 Toxoplasma gondii Cyst Wall Interactome. *MBio* **11**. doi:10.1128/mBio.02699-19
1771 Uboldi AD, Wilde M-L, McRae EA, Stewart RJ, Dagley LF, Yang L, Katris NJ, Hapuarachchi SV, Coffey
1772 MJ, Lehane AM, Botte CY, Waller RF, Webb AI, McConville MJ, Tonkin CJ. 2018. Protein kinase A
1773 negatively regulates Ca2+ signalling in Toxoplasma gondii. *PLoS Biol* **16**:e2005642.
1774 Uras IZ, List T, Nijman SMB. 2012. Ubiquitin-specific protease 4 inhibits mono-ubiquitination of the
1775 master growth factor signaling kinase PDK1. *PLoS One* **7**:e31003.
1776 Waldman BS, Schwarz D, Wadsworth MH 2nd, Saeij JP, Shalek AK, Lourido S. 2020. Identification of a
1777 Master Regulator of Differentiation in Toxoplasma. *Cell* **180**:359–372.e16.

1778 Wang J, Dixon SE, Ting L-M, Liu T-K, Jeffers V, Croken MM, Calloway M, Cannella D, Hakimi MA, Kim K,
1779 Sullivan WJ Jr. 2014. Lysine acetyltransferase GCN5b interacts with AP2 factors and is required for
1780 Toxoplasma gondii proliferation. *PLoS Pathog* **10**:e1003830.
1781 Wang J-L, Li T-T, Elsheikha HM, Liang Q-L, Zhang Z-W, Wang M, Sibley LD, Zhu X-Q. 2022. The protein
1782 phosphatase 2A holoenzyme is a key regulator of starch metabolism and bradyzoite
1783 differentiation in Toxoplasma gondii. *Nat Commun* **13**:7560.
1784 Wang K, Peng ED, Huang AS, Xia D, Vermont SJ, Lentini G, Lebrun M, Wastling JM, Bradley PJ. 2016.
1785 Identification of Novel O-Linked Glycosylated Toxoplasma Proteins by Vicia villosa Lectin
1786 Chromatography. *PLoS One* **11**:e0150561.
1787 Wan W, Dong H, Lai D-H, Yang J, He K, Tang X, Liu Q, Hide G, Zhu X-Q, Sibley LD, Lun Z-R, Long S.
1788 2023. The Toxoplasma micropore mediates endocytosis for selective nutrient salvage from host
1789 cell compartments. *Nat Commun* **14**:977.
1790 Wiersma HI, Galuska SE, Tomley FM, Sibley LD, Liberator PA, Donald RGK. 2004. A role for coccidian
1791 cGMP-dependent protein kinase in motility and invasion. *Int J Parasitol* **34**:369–380.
1792 Wilde M-L, Triglia T, Marapana D, Thompson JK, Kouzmitchev AA, Bullen HE, Gilson PR, Cowman AF,
1793 Tonkin CJ. 2019. Protein Kinase A Is Essential for Invasion of Plasmodium falciparum into Human
1794 Erythrocytes. *MBio* **10**. doi:10.1128/mBio.01972-19
1795 Williams MR, Arthur JS, Balendran A, van der Kaay J, Poli V, Cohen P, Alessi DR. 2000. The role of 3-
1796 phosphoinositide-dependent protein kinase 1 in activating AGC kinases defined in embryonic stem
1797 cells. *Curr Biol* **10**:439–448.
1798 Yang C, Arrizabalaga G. 2017. The serine/threonine phosphatases of apicomplexan parasites. *Mol*
1799 *Microbiol* **106**:1–21.
1800 Yang C, Broncel M, Dominicus C, Sampson E, Blakely WJ, Treeck M, Arrizabalaga G. 2019. A plasma
1801 membrane localized protein phosphatase in Toxoplasma gondii, PPM5C, regulates attachment to
1802 host cells. *Sci Rep* **9**:5924.
1803 Yang J, Yang X, Liu A, Li Y, Niu Z, Lyu C, Liang X, Xia N, Cui J, Li M, Wu P, Peng C, Shen B. 2022. The
1804 beta subunit of AMP-activated protein kinase is critical for cell cycle progression and parasite
1805 development in Toxoplasma gondii. *Cell Mol Life Sci* **79**:532.
1806 Young JC, Broncel M, Teague H, Russell MRG, McGovern OL, Renshaw M, Frith D, Snijders AP,
1807 Collinson L, Carruthers VB, Ewald SE, Treeck M. 2020. Phosphorylation of Toxoplasma gondii
1808 Secreted Proteins during Acute and Chronic Stages of Infection. *mSphere* **5**.
1809 doi:10.1128/mSphere.00792-20

1810

1811 ## TABLES

1812 **Table 1.** Proteins discussed in the text.

Gene ID	Description	Context in text	Modifications	Reference	Dataset
TGGT1_268210	AGC kinase	SPARK		(Smith et al., 2022)	
TGGT1_291010	hypothetical protein	SPARKEL			SPARK IP-MS
TGGT1_205550	AGC kinase	AGC kinase			SPARK TurboID, SPARKEL TurboID

TGGT1_310220	hypothetical protein	BCC10		(Engelberg et al., 2022)	SPARKEL IP-MS
TGGT1_269460	Ser/Thr phosphatase family protein	EFPP/BCC5	S550	(Engelberg et al., 2022; Liang et al., 2021; Roumégous et al., 2022)	SPARKEL IP-MS, SPARK depletion timecourse phosphoproteome
TGGT1_311360	protein kinase G AGC kinase family member PKG	PKG		(Brown et al., 2017)	24h SPARK depletion proteome, SPARK depletion timecourse phosphoproteome
TGGT1_226030	AGC kinase	PKA C1		(Jia et al., 2017; Uboldi et al., 2018)	24h SPARK depletion proteome, SPARK depletion timecourse phosphoproteome
TGGT1_242070	cAMP-dependent protein kinase regulatory subunit	PKA R	S27	(Jia et al., 2017; Uboldi et al., 2018)	24h SPARK depletion proteome, SPARK depletion timecourse phosphoproteome, PKA C3 depletion proteome
TGGT1_270240	MAG1 protein	MAG1	S238	(Parmley et al., 1994)	24h SPARK depletion proteome, PKA C3 depletion phosphoproteome
TGGT1_314250	bradyzoite rhoptry protein	BRP1		(Schwarz et al., 2005)	24h SPARK depletion proteome, 24h PKA C3 depletion proteome

TGGT1_208740	putative microneme protein			(Waldman et al., 2020)	24h SPARK depletion proteome, 24h PKA C3 depletion proteome
TGGT1_264660	SAG-related sequence SRS44	CST1		(Tomita et al., 2013)	24h SPARK depletion proteome, PKA C3 depletion transcriptome
TGGT1_312330	hypothetical protein	CST10		(Tu et al., 2020; Waldman et al., 2020)	24h SPARK depletion proteome, PKA C3 depletion transcriptome
TGGT1_260190	microneme protein MIC13	MIC13		(Fritz et al., 2012)	24h SPARK depletion proteome, PKA C3 depletion transcriptome
TGGT1_311100	zinc finger (CCCH type) motif-containing protein	BFD2	S183	(Licon et al., 2023)	24h SPARK depletion proteome, 24h PKA C3 depletion proteome, PKA C3 depletion phosphoproteome
TGGT1_266010	phosphatidylinositol 3- and 4-kinase	PI3/4K	S1439		SPARK depletion timecourse phosphoproteome
TGGT1_202550	NLI interacting factor family phosphatase	CTD3/BCC6	T384 and T386	(Engelberg et al., 2022)	SPARK depletion timecourse phosphoproteome
TGGT1_224240	protein phosphatase 2C domain-containing protein	PPM1	S557	(Yang and Arrizabalaga, 2017)	SPARK depletion timecourse phosphoproteome

TGGT1_268770	dual specificity phosphatase, catalytic domain-containing protein	phosphosite down-regulated with SPARK depletion	S11		SPARK depletion timecourse phosphoproteome
TGGT1_219682	putative pyruvate dehydrogenase kinase		S633	(Ferrarini et al., 2021)	SPARK depletion timecourse phosphoproteome
TGGT1_225960	STE kinase		S2905		SPARK depletion timecourse phosphoproteome
TGGT1_305860	calcium-dependent protein kinase 3	CDPK3	T40		SPARK depletion timecourse phosphoproteome
TGGT1_267580	cyclin2-related protein		S491		SPARK depletion timecourse phosphoproteome
TGGT1_204280	cell-cycle-associated protein kinase DYRK		T642, S645, and S649	(Smith et al., 2022)	SPARK depletion timecourse phosphoproteome
TGGT1_239885	hypothetical protein		S933 and S936	(Smith et al., 2022)	SPARK depletion timecourse phosphoproteome
TGGT1_267100	protein phosphatase 2C domain-containing protein	PPM2B	S/T778-788	(Yang et al., 2019)	SPARK depletion timecourse phosphoproteome
TGGT1_311310	protein phosphatase 2B catalytic subunit, calcineurin family phosphatse superfamily protein	CnA	S104	(Paul et al., 2015)	SPARK depletion timecourse phosphoproteome

TGGT1_277895	ubiquitin carboxyl-terminal hydrolase	UBP1	S44, S52, S1691, and S1695	(Koreny et al., 2023; Wan et al., 2023)	SPARK depletion timecourse phosphoproteome
TGGT1_294360	putative ubiquitin specific protease 39 isoform 2	USP39	S20		SPARK depletion timecourse phosphoproteome
TGGT1_226050	hypothetical protein	RBR E3 ligase	S319 and S322		SPARK depletion timecourse phosphoproteome
TGGT1_239410	hypothetical protein	putative CCR4-NOT complex subunit	S80		SPARK depletion timecourse phosphoproteome
TGGT1_295658	zinc finger in N-recognin protein	UBR box E3 ligase	S3335		SPARK depletion timecourse phosphoproteome
TGGT1_295710	HECT-domain (ubiquitin-transferase) domain-containing protein	HECT E3	S2166, S4313		SPARK depletion timecourse phosphoproteome, PKA R depletion timecourse phosphoproteome
TGGT1_216130	putative ubiquitin conjugating enzyme E2	putative E2 enzyme	S193		SPARK depletion timecourse phosphoproteome, PKA R depletion timecourse phosphoproteome
TGGT1_293670	transcription elongation factor A TFIIS	TFIIS	S356		SPARK depletion timecourse phosphoproteome

TGGT1_226810	histone lysine methyltransferase SET1	SET1	S1780 and S1781		PKA C3 and SPARK depletion timecourse phosphoproteome
TGGT1_218070	hypothetical protein	NOC3p	S1343		PKA C3 and SPARK depletion timecourse phosphoproteome
TGGT1_280800	SWI2/SNF2 SRCAP/Ino80	TgSRCAP	S635 and S638	(Sullivan et al., 2003)	SPARK depletion timecourse phosphoproteome
TGGT1_306660	RNA pseudouridine synthase superfamily protein	PUS1	S506	(Anderson et al., 2009)	SPARK depletion timecourse phosphoproteome
TGGT1_312370	RNA pseudouridine synthase superfamily protein	PUS protein	S951		SPARK depletion timecourse phosphoproteome
TGGT1_231970	pre-mRNA processing splicing factor PRP8	PRP8	T820		SPARK depletion timecourse phosphoproteome
TGGT1_310820	putative SLU7 splicing factor	SLU7	S[516-519]		SPARK depletion timecourse phosphoproteome
TGGT1_267600	FHA domain-containing protein	a FHA protein	S406 and S413		SPARK depletion timecourse phosphoproteome
TGGT1_216670	FUSE-binding protein 2 / KH-type splicing regulatory protein	KH protein	S8		PKA R, PKA C3, and SPARK depletion phosphoproteome

TGGT1_241170	hypothetical protein	KH protein	S362, S368, and S665		SPARK depletion timecourse phosphoproteome
TGGT1_235930	domain K- type RNA binding proteins family protein	KH protein	S58 and S59	(Farhat et al., 2021)	SPARK depletion timecourse phosphoproteome
TGGT1_227450	hydrolase, NUDIX family protein	DCP2 homolog	T1982 and S1985		SPARK depletion timecourse phosphoproteome
TGGT1_260600	Pumilio-family RNA binding repeat-containing protein	PUF1	S225	(Joyce et al., 2013; Liu et al., 2014)	SPARK depletion timecourse phosphoproteome
TGGT1_246040	MIF4G domain-containing protein	MIF4G domain protein	S341 and S383		SPARK depletion timecourse phosphoproteome
TGGT1_249610	hypothetical protein	CBP80	S851 and S853	(Gissot et al., 2013)	PKA C3 and SPARK depletion timecourse phosphoproteome
TGGT1_317720	putative eukaryotic translation initiation factor 3 subunit 7	eIF3	S587		SPARK depletion timecourse phosphoproteome
TGGT1_231480	putative GCN1	GCN1	S1100		SPARK depletion timecourse phosphoproteome
TGGT1_251630	slc30a2 protein	TgZnT	S448	(Chasen et al., 2019)	PKA C3 and SPARK depletion timecourse phosphoproteome

TGGT1_288540	nucleoside transporter protein	nucleoside transporter			SPARK depletion timecourse phosphoproteome
TGGT1_260310	ATP-binding cassette transporter ABC.B1	ABC transporter			SPARK depletion timecourse phosphoproteome
TGGT1_318710	ATP-binding cassette sub-family F member 1	ABC transporter			SPARK depletion timecourse phosphoproteome
TGGT1_280660	HECT-domain (ubiquitin-transferase) domain-containing protein	putative HECT-domain E3 ubiquitin ligase	S5275 and S5279		SPARK TurboID, SPARK depletion timecourse phosphoproteome
TGGT1_286470	AGC kinase	PKA C3		(Sugi et al., 2016)	SPARK TurboID
TGGT1_218240	hypothetical protein	IMC25	S1231	(Wang et al., 2016)	PKA R and SPARK depletion phosphoproteome
TGGT1_220900	hypothetical protein	AC13	S101, S220, S659	(Back et al., 2023)	PKA R, PKG, PKA C3, and SPARK depletion phosphoproteome
TGGT1_225690	hypothetical protein	CIP1	S850 and S851	(Long et al., 2017)	PKA R and SPARK depletion phosphoproteome
TGGT1_257300	hypothetical protein	CIP2	S26	(Long et al., 2017)	PKA R and SPARK depletion phosphoproteome
TGGT1_308860	hypothetical protein	AC3	S216	(Chen et al., 2015)	PKA R and SPARK depletion phosphoproteome

TGGT1_315150	putative eukaryotic initiation factor-4E	eIF4E	S1231		PKA R and SPARK depletion phosphoproteome
TGGT1_235930	domain K- type RNA binding proteins family protein	KH protein	S58 and S59	(Farhat et al., 2021)	PKA R and SPARK depletion phosphoproteome
TGGT1_251640	ubiquitin-conjugating enzyme subfamily protein	E2 protein	S23		PKA R and SPARK depletion phosphoproteome
TGGT1_253700	transporter, major facilitator family protein	MFS transporter	S144, S1287, S1288		PKG and SPARK depletion phosphoproteome
TGGT1_312100	plasma membrane-type Ca(2+)-ATPase A1 PMCAA1	TgA1	S444 and S445		PKG and SPARK depletion phosphoproteome
TGGT1_314780	myosin G	MyoG	T1300	(Frénal et al., 2017)	PKG and SPARK depletion phosphoproteome
TGGT1_295360	hypothetical protein	IMC18	S159, S161, and S165	(Chen et al., 2015)	PKG and SPARK depletion phosphoproteome
TGGT1_239400	hypothetical protein	IMC28	S1081 and S1082	(Chen et al., 2017)	PKG and SPARK depletion phosphoproteome
TGGT1_225560	hypothetical protein	IMC41	S440	(Back et al., 2023)	PKG and SPARK depletion phosphoproteome
TGGT1_313480	hypothetical protein	AAP3	S178	(Engelberg et al., 2020)	PKG and SPARK depletion phosphoproteome

TGGT1_235380	hypothetical protein	AC5/TLAP3	S463	(Chen et al., 2015; Liu et al., 2013)	PKG and SPARK depletion phosphoproteome
TGGT1_263520	microtubule associated protein SPM1	SPM1	S54 and S57	(Tran et al., 2012)	PKG and SPARK depletion phosphoproteome
TGGT1_211710	TB2/DP1, HVA22 family protein	TB2/DP1, HVA22 family proteins	S155 and S177		PKG and SPARK depletion phosphoproteome
TGGT1_257040	TB2/DP1, HVA22 family protein	TB2/DP1, HVA22 family proteins	S32		PKG and SPARK depletion phosphoproteome
TGGT1_229490	tetratricopeptide repeat-containing protein	TPR protein TGGT1_229490	S456, S570 and S575		PKG and SPARK depletion phosphoproteome
TGGT1_246600	ABC1 family protein	ER ABC transporter	T1278		PKG and SPARK depletion phosphoproteome
TGGT1_232190	Sec7 domain-containing protein	Sec7 protein	S180		PKG and SPARK depletion phosphoproteome
TGGT1_224150	hypothetical protein	TgCOG6	T533 and T673	(Marsilia et al., 2023)	PKG and SPARK depletion phosphoproteome
TGGT1_203910	TBC domain-containing protein	TgTBC10	T254 and S256	(Quan et al., 2023)	PKG and SPARK depletion phosphoproteome
TGGT1_250870	DHHC zinc finger domain-containing protein	TgDHHC1	S345 and S348	(Frénal et al., 2013)	PKG and SPARK depletion phosphoproteome

TGGT1_212820	ubiquitin family protein	ubiquitin family protein with a C-terminal extension	S368		PKG and SPARK depletion phosphoproteome
TGGT1_290970	8-amino-7-oxononanoate synthase	TgSPT2		(Nyonda et al., 2022)	PKA C3 depletion transcriptome
TGGT1_259020	bradyzoite antigen BAG1	BAG1		(Behnke et al., 2008)	PKA C3 depletion transcriptome
TGGT1_253440	cell-cycle-associated protein kinase SRPK, putative	SRPK		(Talevich et al., 2011)	PKA C3 IP-MS
TGGT1_268960	putative 5'-AMP-activated protein kinase subunit beta-1 family protein	AMPK subunit beta		(Yang et al., 2022)	PKA C3 IP-MS
TGGT1_209985	cAMP-dependent protein kinase	secreted cAMP-dependent protein kinases			PKA C3 depletion proteome
TGGT1_356400	cAMP-dependent protein kinase	secreted cAMP-dependent protein kinases			PKA C3 depletion proteome
TGGT1_277790	hypothetical protein	DEP domain protein	S586-600		PKA C3 depletion phosphoproteome
TGGT1_318150	transporter, major facilitator family protein	TgApiAT3-1	S54		PKA C3 and SPARK depletion phosphoproteomes
TGGT1_259260	membrane protein FtsH1	FtsH1	S553		PKA C3 depletion phosphoproteome
TGGT1_227280	dense granule protein GRA3	GRA3	S120, T145, S197		PKA C3 depletion phosphoproteome

TGGT1_312420	hypothetical protein	GRA38	S457	(Nadipuram et al., 2016)	PKA C3 depletion phosphoproteome
TGGT1_204340	hypothetical protein	CST8	T601	(Tu et al., 2020)	PKA C3 depletion phosphoproteome
TGGT1_230180	hypothetical protein	GRA24	T144	(Braun et al., 2013)	PKA C3 depletion phosphoproteome
TGGT1_269180	MIF4G domain-containing protein	eIF4G1	S1312	(Holmes et al., 2023)	PKA C3 depletion phosphoproteome
TGGT1_218300	zinc finger (CCCH type) motif-containing protein	zinc finger protein	S663		PKA C3 depletion phosphoproteome
TGGT1_209500	hypothetical protein	DNA repair protein	S619		PKA C3 depletion phosphoproteome
TGGT1_310450	putative myosin heavy chain	IAP2	T1269		PKA C3 depletion phosphoproteome
TGGT1_273050	hypothetical protein	BCC8		(Liang et al., 2021)	PKA C3 depletion phosphoproteome
TGGT1_287240	hypothetical protein	condensin 2			PKA C3 depletion phosphoproteome
TGGT1_278660	putative P-type ATPase4	ATP4	S83 and T166		PKA C3 depletion phosphoproteome

TGGT1_233130	nucleoside transporter protein	nucleoside transporter	S6		PKA C3 depletion phosphoproteome
TGGT1_292020	GCC2 and GCC3 domain-containing protein	CRMP-b	S7300, S7303, S7363, and S7365	(Singer et al., 2023; Sparvoli et al., 2022)	PKA C3 depletion phosphoproteome
TGGT1_221180	hypothetical protein	microneme protein	S788		PKA C3 depletion phosphoproteome
TGGT1_304490	hypothetical protein	microneme protein	S10		PKA C3 depletion phosphoproteome
TGGT1_309590	rhoptry protein ROP1	ROP1	T248		PKA C3 depletion phosphoproteome
TGGT1_211290	rhoptry protein ROP15	ROP13	S312		PKA C3 depletion phosphoproteome
TGGT1_258580	rhoptry protein ROP17	ROP17	T51		PKA C3 depletion phosphoproteome
TGGT1_291960	rhoptry kinase family protein ROP40 (incomplete catalytic triad)	ROP40	S98		PKA C3 depletion phosphoproteome
TGGT1_308810	rhoptry neck protein RON9	RON9	S190, S239, S327, and S375		PKA C3 depletion phosphoproteome
TGGT1_310780	dense granule protein GRA4	GRA4	S248		PKA C3 depletion phosphoproteome

TGGT1_275440	dense granule protein GRA6	GRA6	S133 and S134		PKA C3 depletion phosphoproteome
TGGT1_203310	dense granule protein GRA7	GRA7	S62, S72, S77, S135, S153		PKA C3 depletion phosphoproteome
TGGT1_254720	dense granule protein GRA8	GRA8	S198, T202, T262		PKA C3 depletion phosphoproteome
TGGT1_220240	hypothetical protein	GRA31	S420	(Nadipuram et al., 2020; Young et al., 2020)	PKA C3 depletion phosphoproteome
TGGT1_217680	hypothetical protein	GRA57	S806	(Krishnamurthy et al., 2023; Nadipuram et al., 2020; Young et al., 2020)	PKA C3 depletion phosphoproteome
TGGT1_215360	hypothetical protein	GRA62	S319	(Cygan et al., 2021)	PKA C3 depletion phosphoproteome
TGGT1_249990	hypothetical protein	GRA70	S436	(Krishnamurthy et al., 2023; Lockyer et al., 2023)	PKA C3 depletion phosphoproteome
TGGT1_289540	hypothetical protein	SFP1	S897	(Young et al., 2020)	PKA C3 depletion phosphoproteome
TGGT1_251740	AP2 domain transcription factor AP2XII-9	AP2XII-9	S1697		PKA C3 depletion phosphoproteome
TGGT1_273870	SWI2/SNF2 ISWI-like (AT hook)	ISWI protein	T765		PKA C3 depletion phosphoproteome

TGGT1_260240	hypothetical protein	CAF1	S272		PKA C3 depletion phosphoproteome
TGGT1_253750	PLU-1 family protein	PLU-1	S3874 and S3877	(Wang et al., 2014)	PKA C3 depletion phosphoproteome
TGGT1_300330	hypothetical protein	GCFC	S27		PKA C3 depletion phosphoproteome
TGGT1_223880	zinc finger, C3HC4 type (RING finger) domain-containing protein	zinc finger protein	S3701		PKA C3 depletion phosphoproteome
TGGT1_288380	heat shock protein HSP90	HSP90	S600		PKA C3 depletion phosphoproteome
TGGT1_321520	hypothetical protein	p23	S109		PKA C3 depletion phosphoproteome
TGGT1_225450	hypothetical protein	CSN3	S509 and S517		PKA C3 depletion phosphoproteome
TGGT1_242890	hypothetical protein	PSME4	S3127		PKA C3 depletion phosphoproteome
TGGT1_218960	AP2 domain transcription factor AP2XII-1	AP2XII-1	T1697, S1702, T1667, T1703	(Antunes et al., 2023)	PKA C3 depletion phosphoproteome

TGGT1_262150	kelch repeat and K+ channel tetramerisation domain containing protein	Kelch13	S139	(Harding et al., 2020; Koreny et al., 2023; Wan et al., 2023)	PKA C3 depletion phosphoproteome
TGGT1_254940	MIF4G domain-containing protein	eIF4G2	S985 and S989	(Holmes et al., 2023)	PKA C3 and SPARK depletion phosphoproteomes
TGGT1_320020	transporter, major facilitator family protein	TgApiAT2	S316 and T318		PKA C3 and SPARK depletion phosphoproteomes
TGGT1_233000	KOW motif domain-containing protein	Spt5	S1011 and S1014		PKA C3 and SPARK depletion phosphoproteomes
TGGT1_279320	hypothetical protein	nucleotidyltransferase	S4010		PKA C3 and SPARK depletion phosphoproteomes
TGGT1_313180	putative cell-cycle-associated protein kinase PRP4	PRP4	S316	(Swale et al., 2022)	
TGGT1_214140	hypothetical protein	associates with AP2IX4/MORC complex	S205 and S212		
TGGT1_309250	hypothetical protein	associates with GCN5-B complex	PMID: 31381949 and 24391497		

1813
1814

1815 ## FIGURE LEGENDS

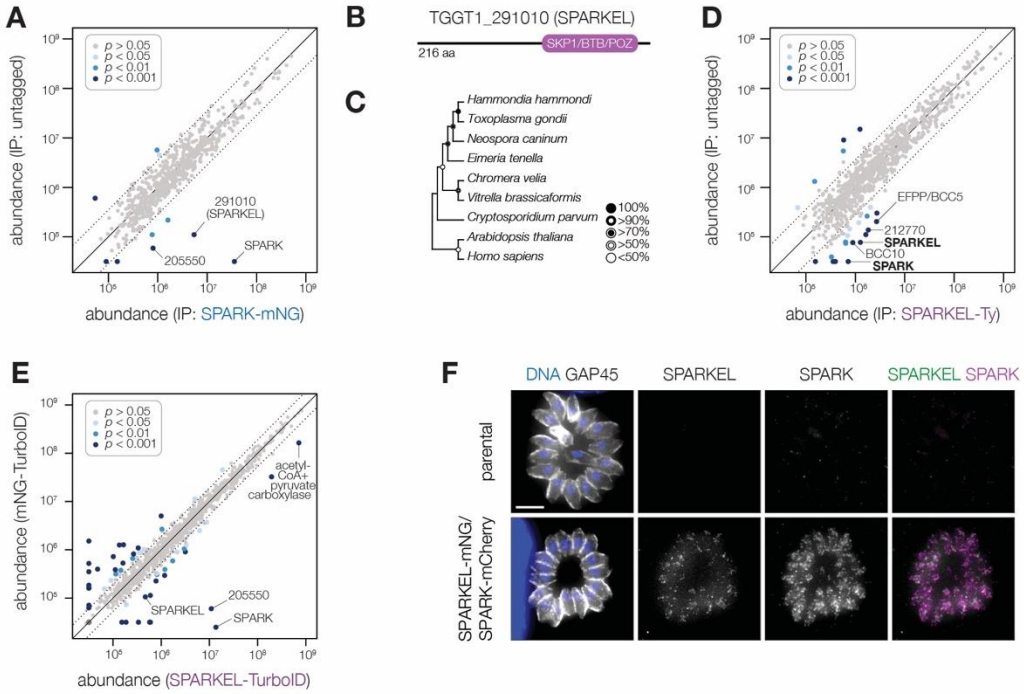

1816

1817 **Figure 1. SPARK interacts with an Elongin C-like protein. (A)** Protein abundances from
1818 immunopurified SPARK-mNG lysates or an untagged control strain. Dotted lines correspond to one
1819 modified z-score. Only proteins quantified by greater than one peptide are shown. Proteins identified in
1820 only one IP were assigned a pseudo-abundance of $10^{4.5}$. **(B)** TGGT1_291010 SPARK elongin-like protein
1821 (SPARKEL) gene model. **(C)** Neighbor-joining phylogenetic tree of SKP1/BTB/POZ domains of
1822 TGGT1_291010 orthologs in apicomplexan species along with human and arabidopsis proteins as
1823 outgroups. Bootstrap values determined from 1000 replicates. **(D)** Protein abundances from
1824 immunopurified SPARKEL-Ty lysates or an untagged control strain. Dotted lines correspond to one
1825 modified z-score. Only proteins quantified by greater than one peptide are shown. Proteins identified
1826 in only one IP were assigned a pseudo-abundance of $10^{4.5}$. **(E)** Protein abundances following
1827 biotinylation and streptavidin enrichment of samples derived from parasites expressing mNG- or
1828 SPARKEL-TurboID fusion constructs. A pseudocount of $10^{4.5}$ was assigned to proteins identified in only
1829 one sample. Point colors correspond to significance thresholds. Dotted lines correspond to one median
1830 absolute deviation. **(F)** Immunofluorescence microscopy of intracellular parasites co-expressing
1831 SPARKEL-mNG and SPARK-mCherry. Parasites and nuclei were stained with GAP45 and Hoechst
1832 33342, respectively.
1833

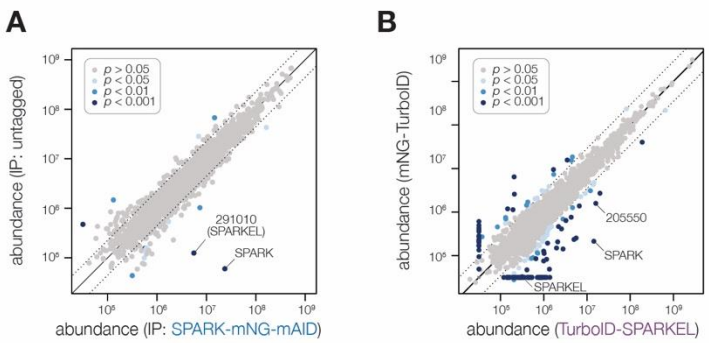

Figure 1—figure supplement 1. Additional data supporting the interaction between SPARK and SPARKEL. (A) Protein abundances from immunopurified SPARK-mNG-mAID (Smith et al., 2022) lysates or an untagged control strain. Dotted lines correspond to one modified z-score. Only proteins quantified by greater than one peptide are shown. Proteins identified in only one IP were assigned a pseudo-abundance of $10^{4.5}$. **(B)** Protein abundances following biotinylation and streptavidin enrichment of samples derived from parasites expressing mNG- or TurboID-SPARKEL fusion constructs. A pseudocount of $10^{4.5}$ was assigned to proteins identified in only one sample. Point colors correspond to significance thresholds. Dotted lines correspond to one median absolute deviation.

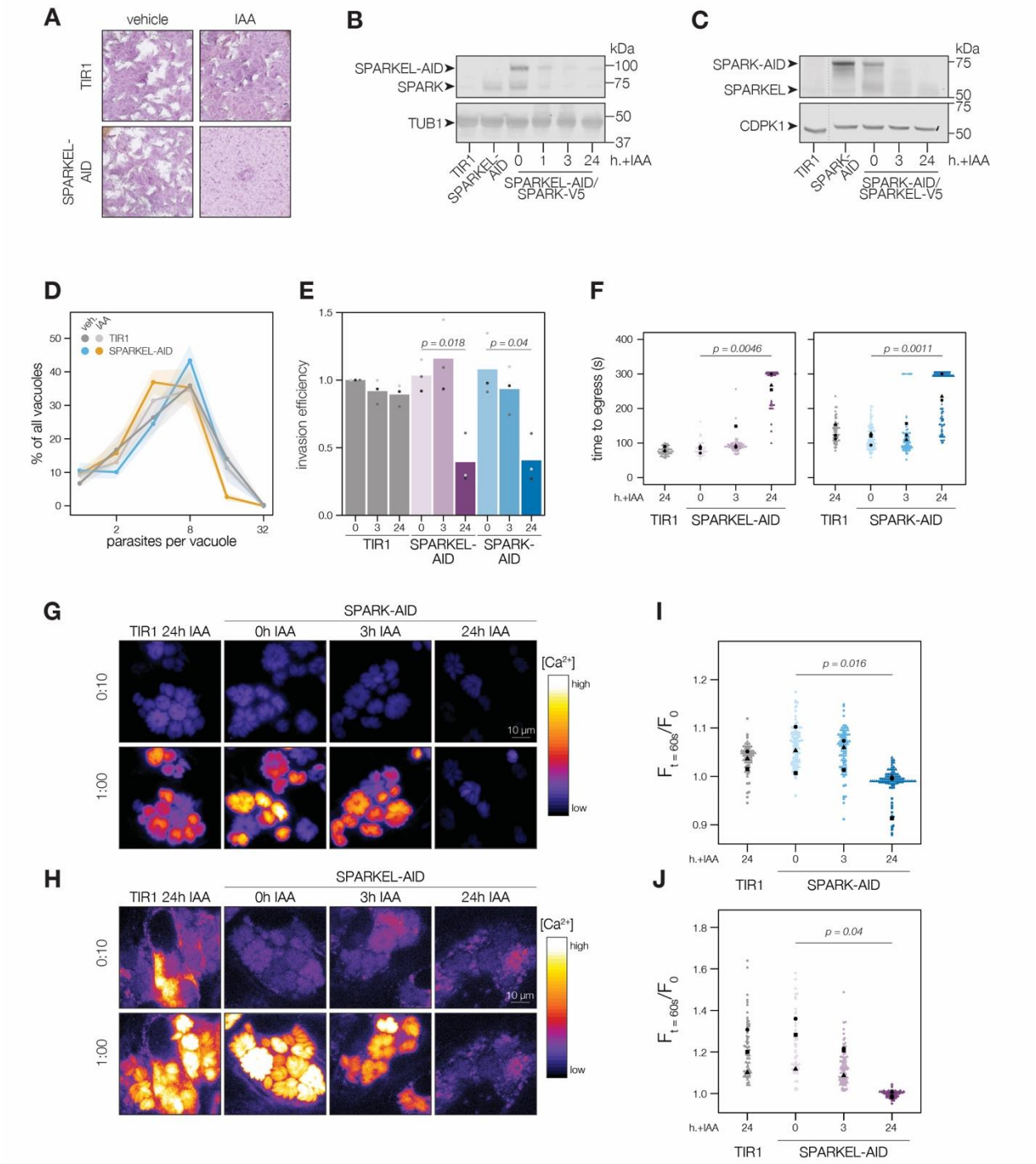

Figure 2. SPARKEL depletion phenocopies the loss of SPARK. (A) Plaque assays of 500 TIR1 or SPARKEL-AID parasites infected onto host cell monolayers and allowed to undergo repeated cycles of invasion, replication, and lysis for 7 days in media with or without 500 µM IAA. **(B)** Immunoblot of parasites expressing SPARKEL-V5-AID and SPARK-V5 after the indicated hours with IAA. TUB1 serves as a loading control. **(C)** Immunoblot of parasites expressing SPARK-V5-AID and SPARKEL-V5 after the indicated hours with IAA. CDPK1 serves as loading control. **(D)** The number of parasites per vacuole measured for SPARKEL-AID and the parental strain after 24 hours of 500 µM IAA treatment. Mean counts (*n* = 8) are expressed as a percentage of all vacuoles counted. SEM is shown as shaded area. No

1853 comparisons yielded significant p-values using ANOVA and Tukey's test. **(E)** Invasion assays SPARKEL-
1854 AID, SPARK-AID or TIR1 parental strains treated with IAA or vehicle for 3 or 24 hours. Parasites were
1855 incubated on host cells for 20 minutes prior to differential staining of intracellular and extracellular
1856 parasites. Parasite numbers were normalized to host cell nuclei for each field. Different shapes
1857 correspond to means of n = 3 biological replicates. For clarity, only significant comparisons (Welch's
1858 one-sided *t*-test) are shown. **(F)** The time to egress of individual intracellular vacuoles following
1859 zaprinast treatment. Points correspond to different vacuoles; shapes different replicates. Black shapes
1860 are the mean for each replicate. P-values were calculated from a one-tailed *t*-test. **(G, H)** Selected
1861 frames from live video microscopy of zaprinast-treated SPARK-AID and SPARKEL-AID parasites,
1862 respectively, expressing the calcium indicator GCaMP6f, and the corresponding parental strain, 25
1863 hours after infection and with the indicated IAA treatment period. See also **Video S1** and **Video S2**. **(I,**
1864 **J)** Relative GCaMP fluorescence of SPARK-AID or SPARKEL-AID vacuoles, respectively, 60 s following
1865 zaprinast treatment. Points correspond to different vacuoles; shapes different replicates. Black shapes
1866 are the mean for each replicate. P-values were calculated from a one-tailed t-test.
1867

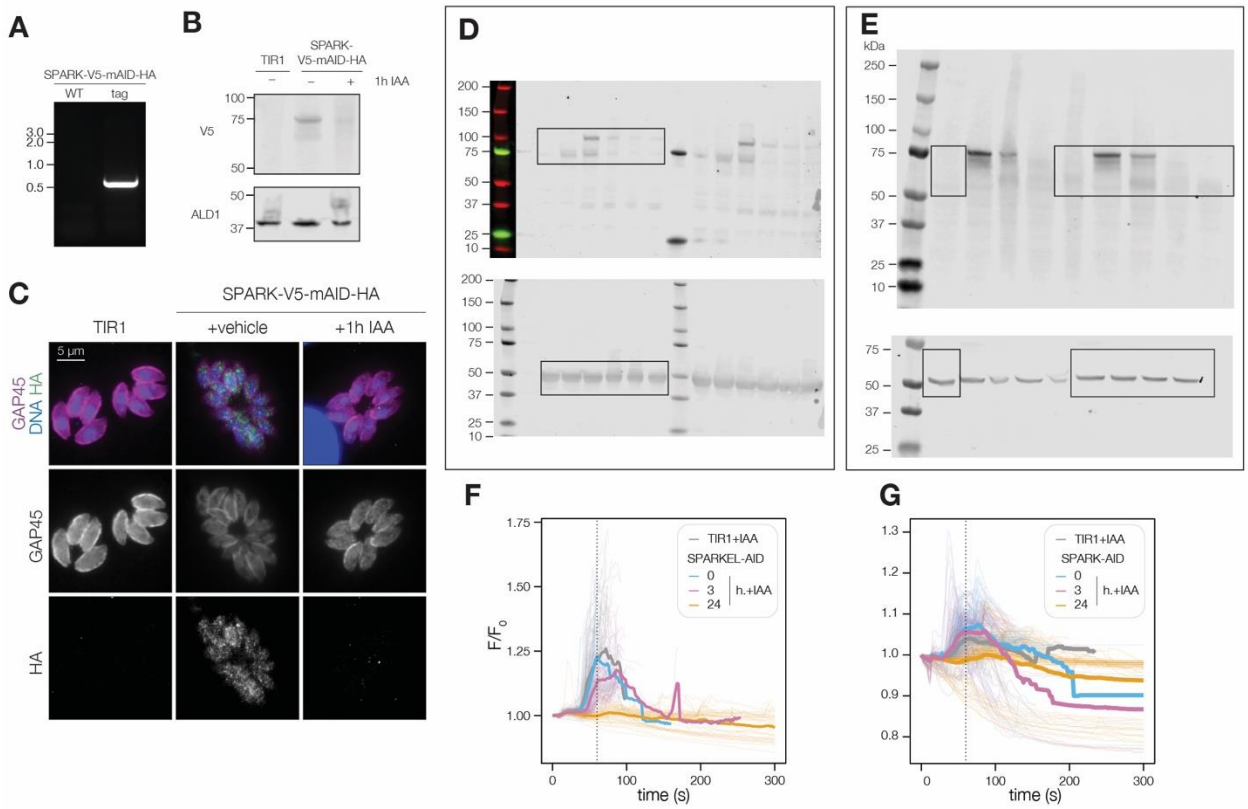

Figure 2—figure supplement 1. (A) Primers specific to the 3′ terminus of SPARK and the V5-mAID-HA tagging payload amplified a product in the SPARK-V5-mAID-HA strain but not the untagged parental strain. **(B)** Confirmation of SPARK-V5-mAID-HA depletion via immunoblot using the V5 epitope. ALD1 was used as a loading control. **(C)** SPARK-V5-mAID-HA depletion was visualized in formaldehyde-fixed intracellular parasites using the HA epitope and GAP45 staining as a parasite marker. DNA was visualized with Hoechst. HA signal intensity was normalized relative to the TIR1 parental strain. **(D)** Uncropped immunoblots corresponding to **Figure 2B**. **(E)** Uncropped immunoblots corresponding to **Figure 2C**. **(F, G)** Normalized GCaMP6f fluorescence of individual SPARK-AID and SPARKEL-AID vacuoles, respectively, after zaprinast treatment and prior to egress (transparent lines) for the indicated period of IAA treatment. The solid line represents the mean normalized fluorescence of all vacuoles across *n = 3* biological replicates.

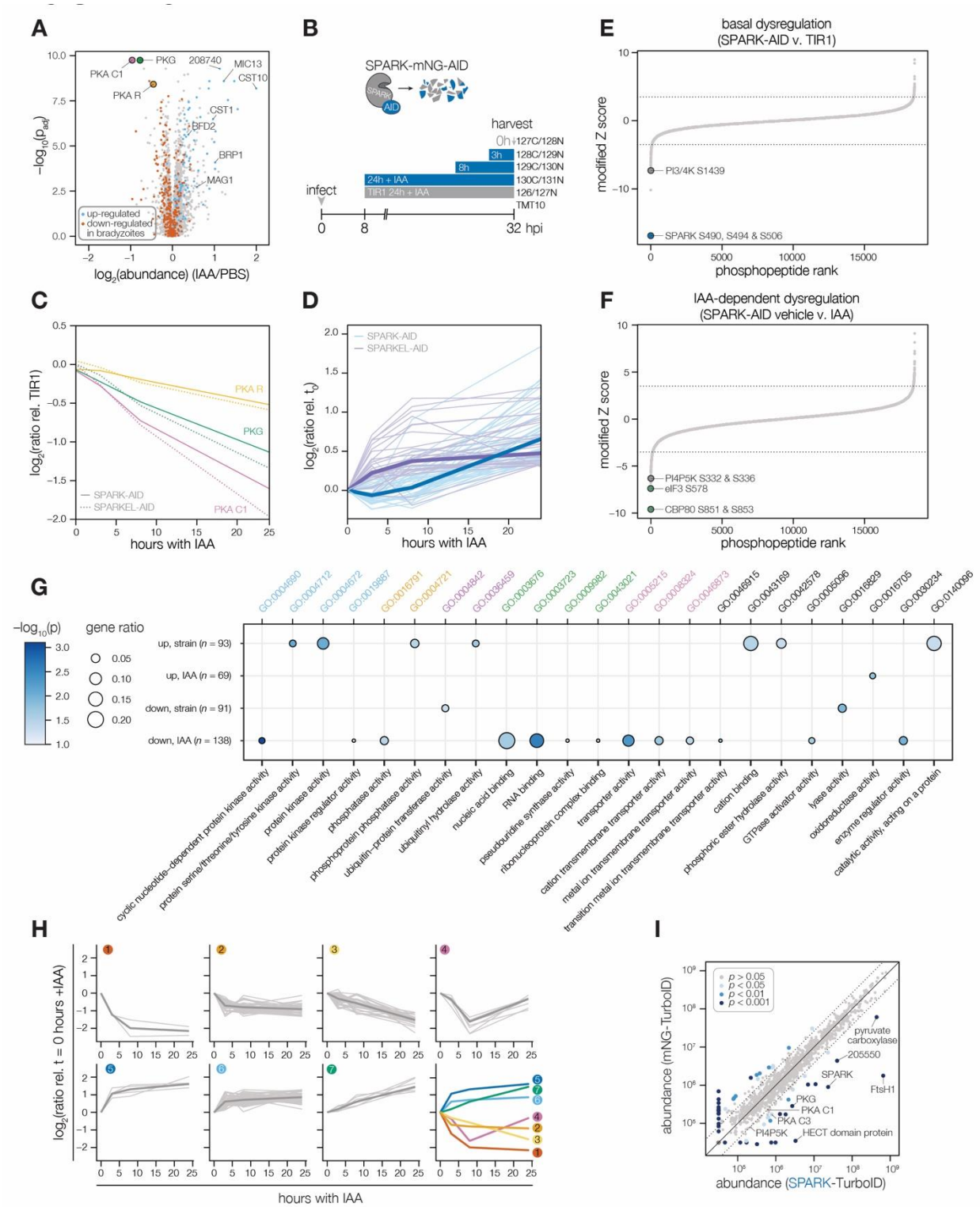

Figure 3. Depletion of SPARK or SPARKEL leads to downregulation of AGC kinases and upregulation of chronic-stage markers. (A) Volcano plot displaying the protein abundance ratios of SPARK-AID parasites treated with IAA or vehicle for 24 hours and adjusted p-values. Proteins identified as up- or down-regulated in parasites overexpressing the driver of differentiation (BFD1) (Waldman et al., 2020) are shown in blue and vermilion, respectively. In total, 4474 proteins were quantified, 3847 of

which registered more than one peptide. **(B)** Schematic of the phosphoproteomics experiment following SPARK depletion. Intracellular parasites expressing SPARK-AID were treated with 500 µM IAA for 24, 8, 3, or 0 h and were harvested simultaneously with the TIR1 parental strain as a control. Samples were multiplexed with tandem mass tags (TMT). The same experimental design was used for SPARKEL-AID proteomics. Each experiment included two biological replicates. **(C)** Protein abundances of PKG, PKA-R, and PKA-C1 relative to the TIR1 parental strain after the indicated period of SPARK (thick lines) or SPARKEL (dotted lines) depletion. **(D)** Protein abundances of up-regulated bradyzoite genes relative to the TIR1 parental strain after the indicated period of SPARK (blue lines) or SPARKEL (purple lines) depletion. Up-regulated bradyzoite proteins were defined as those significantly increased in parasites overexpressing BFD1 (Waldman et al., 2020) and two modified Z-scores above the median in the SPARK depletion proteome. Rank-ordered plots of **(E)** Phosphopeptide basal dysregulation score (peptide abundance in the SPARK-AID strain without IAA treatment relative to the TIR1 parental strain) or **(F)** IAA-dependent score (summed peptide ratios relative to the SPARK-AID t_0 peptide abundance). Dotted lines correspond to 3.5 modified Z scores. Colored points correspond to phosphosites discussed in the main text. **(G)** Gene ontology (GO) enrichment of phosphoproteins exhibiting SPARK-dependent regulation. Gene ratio is the proportion of proteins with the indicated GO term divided by the total number of proteins. Significance was determined with a hypergeometric test; only GO terms with $p < 0.05$ are shown. Redundant GO terms were removed. Categories discussed in the main text are highlighted with colored text. **(H)** Gaussian mixture modeling of SPARK-dependent peptides identified by more than one PSM revealed seven kinetically resolved clusters. Individual peptides or the median ratios in each cluster are depicted by light and dark gray lines, respectively. Clusters are numbered according to their discussion in the main text. **(I)** Protein abundances following biotinylation and streptavidin enrichment of samples derived from parasites expressing mNG- or SPARK-TurboID fusion constructs. A pseudocount of $10^{4.5}$ was assigned to proteins identified in only one sample. Point colors correspond to significance thresholds. Dotted lines correspond to one median absolute deviation.

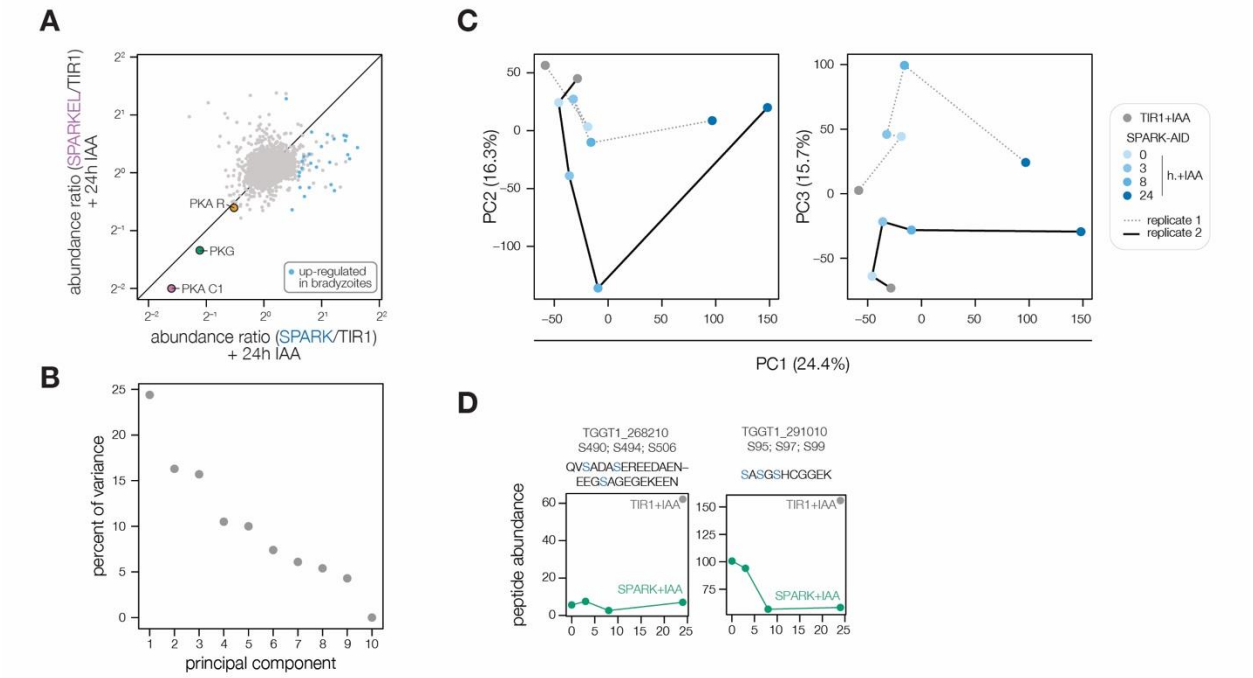

Figure 3—figure supplement 1. Extended analysis of the SPARK-AID depletion phosphoproteome. **(A)** Protein abundance ratios of SPARK- or SPARKEL-AID parasites treated with IAA for 24 hours relative to the untreated samples. Enriched proteins identified as up-regulated in alkaline-induced bradyzoites (Waldman et al., 2020) are shown in blue. The points corresponding to PKA C1, PKA R, and PKG are highlighted in pink, orange, and green, respectively. **(B, C)** Principal component analysis of the SPARK-AID depletion phosphoproteome. Plots show the three components accounting for the greatest proportion of the variance **(D)** Abundances of SPARK and SPARKEL peptides detected by mass spectrometry.

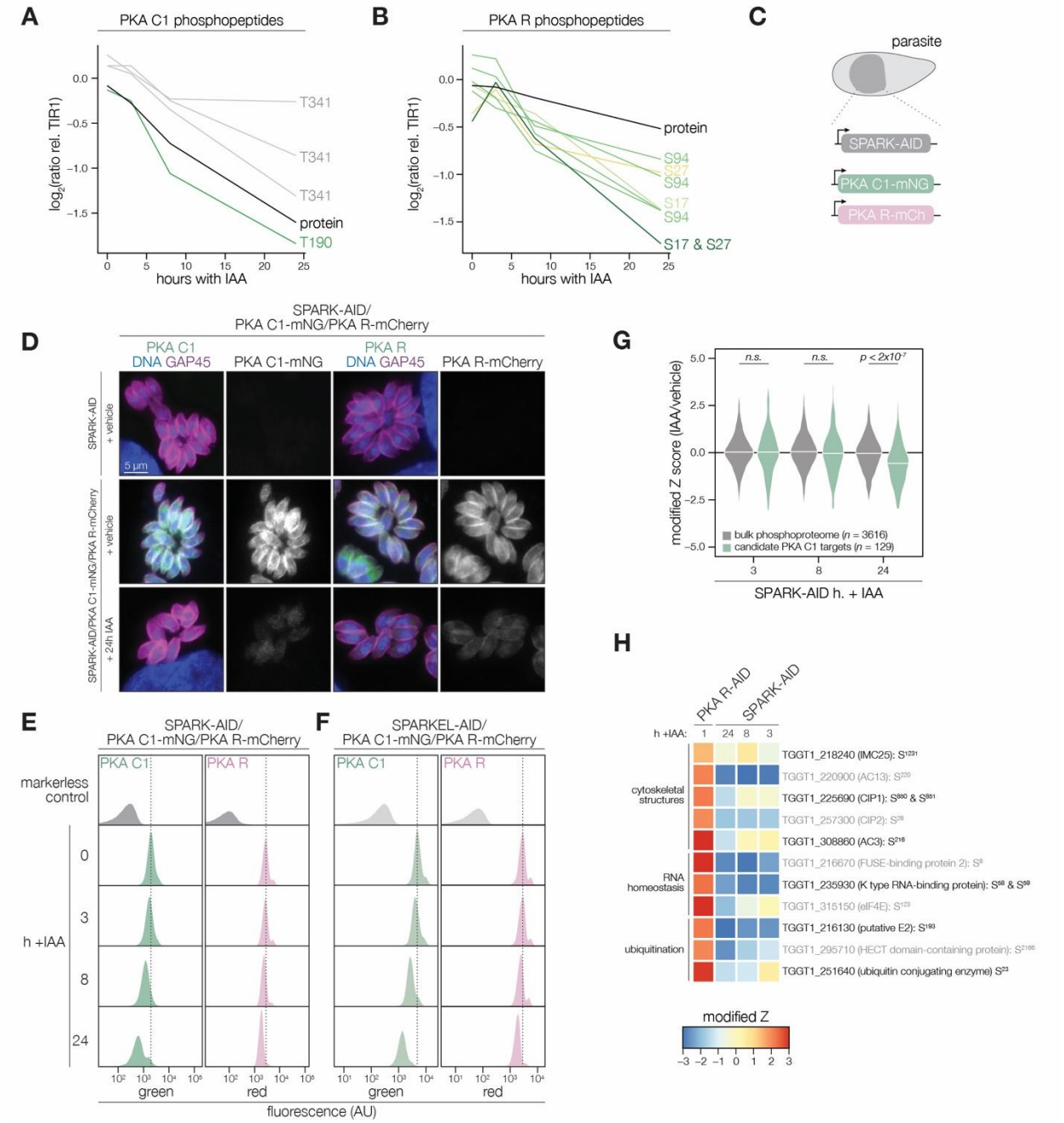

Figure 4. PKA C1 levels are down-regulated upon SPARK depletion. (A–B) Protein and phosphopeptide abundances of PKA C1 **(A)** and PKA R **(B)** following SPARK depletion. **(C)** Schematic of the genetic strategy used to monitor PKA C1 and PKA R abundances following SPARK (or SPARKEL) down-regulation with IAA. **(D)** Immunofluorescence microscopy of parasites expressing SPARK-AID, PKA C1-mNG, and PKA R-mCherry after 0 or 24 hours of IAA treatment to degrade SPARK. Parasites and nuclei were stained with GAP45 and Hoechst 33342, respectively. GAP45 staining and mNG or mCherry staining were normalized to vehicle-treated tagged samples. **(E, F)** Flow cytometry analysis of parasites expressing PKA C1-mNG, PKA R-mCherry, and SPARK-AID or SPARKEL-AID, respectively, after the indicated period of IAA treatment. The dotted line centers the mode of the vehicle-treated sample. Traces were normalized by unit area. **(G)** Violin plots displaying the distribution of phosphopeptide abundance values following SPARK depletion. The distributions of candidate PKA C1

1935 targets, as defined in the text and methods, are shown in green. The distributions and p-values (KS test)
1936 were derived from the overlapping subset of phosphopeptides identified in each dataset. **(H)** Heat map
1937 of the abundance ratios of candidate PKA C1 targets following SPARK depletion. PKA R depletion
1938 results in up-regulation of PKA C1, and candidate PKA C1 targets therefore have positive abundance
1939 ratios following PKA R down-regulation.
1940

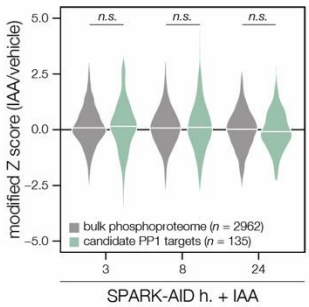

Figure 4—figure supplement 1. Overlap between the SPARK and PP1 phosphoproteomes. Violin plots displaying the distribution of phosphopeptide abundance values following SPARK depletion. The distributions of candidate PP1 targets, as defined in the text and methods, are shown in blue. The distributions and p-values (KS test) were derived from the overlapping subset of phosphopeptides identified in each dataset. PP1 proteome data was obtained from (Herneisen et al., 2022).

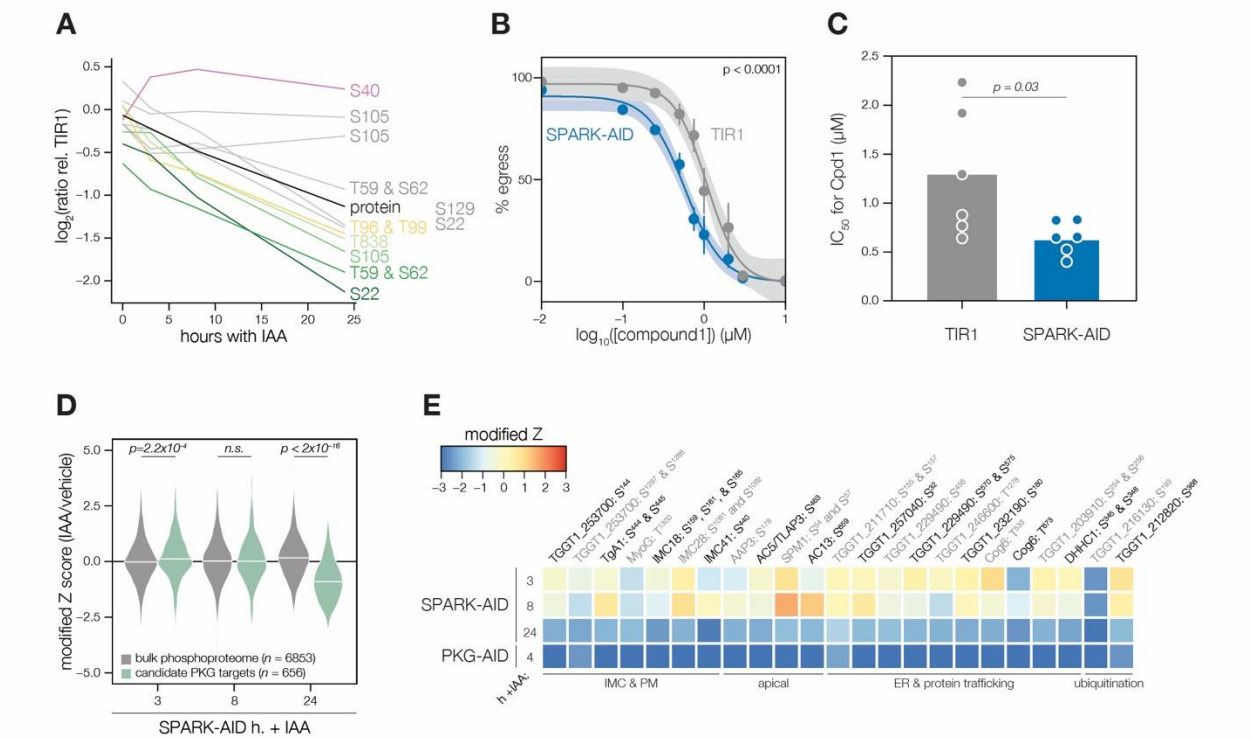

Figure 5. Characterization of PKG function during SPARK depletion. (A) Protein and phosphopeptide abundances of PKG following SPARK depletion. **(B)** A23187-stimulated egress assays performed at different concentrations of compound 1 after TIR1 and SPARK-AID parasites had been treated with IAA for 24 hours. Curves were fit to the average values of six replicates and were compared with an extra sum of squares F test. **(C)** The IC50 values of each strain for compound 1; each point represents a biological replicate. Significance was assessed with a two-tailed *t*-test. **(D)** Violin plots displaying the distribution of phosphopeptide abundance values following SPARK depletion. The distributions of candidate PKG targets are shown in green. The distributions and *p*-values (KS test) were derived from the overlapping subset of phosphopeptides identified in each dataset. **(E)** Heat map of the abundance ratios of candidate PKG targets following SPARK depletion.

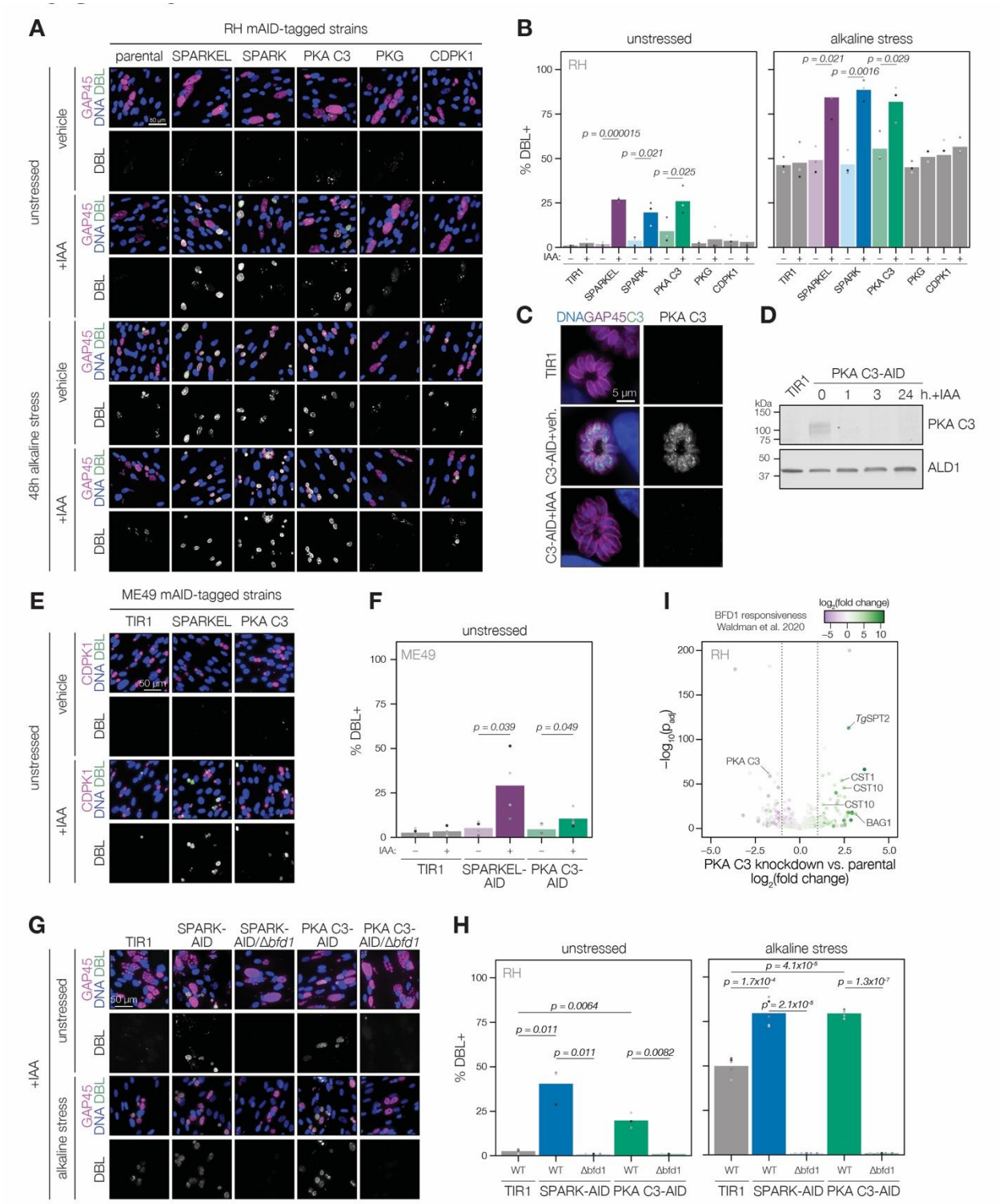

Figure 6. SPARK, SPARKEL, and PKA C3 are negative regulators of differentiation. (A) Immunofluorescence differentiation assays following knockdown of the indicated AID strains for 48 h under standard growth conditions (unstressed) or alkaline stress. GAP45 was used to stain parasite vacuoles. Differentiated vacuoles were stained with biotinylated DBA/streptavidin-APC. Nuclei were stained with Hoechst. **(B)** Quantification of the number of DBL$^+$ vacuoles expressed as a percentage of

1966 the total stained vacuoles is shown for parasites grown under unstressed or stressed conditions. One-
1967 sided *t*-test, $n = 3$ biological replicates. **(C)** Fixed, intracellular PKA C3-mNG-AID parasites visualized by
1968 immunofluorescence microscopy using the mNG epitope after 1 h of vehicle or IAA treatment. The
1969 mNG signal was internally normalized to the TIR1 parental strain. **(D)** Immunoblot of PKA C3-AID
1970 parasites following the addition of vehicle or 500 µM IAA for 1, 3, or 24h. TIR1 was included as an
1971 untagged control. PKA C3-AID was detected with V5, and ALD1 was probed as a loading control. **(E)**
1972 Immunofluorescence differentiation assays following knockdown of the indicated ME49/AID strains
1973 under unstressed conditions for 48 hours. Staining was performed as described above, except CDPK1
1974 was used as a parasite vacuole marker. **(F)** Quantification of the number of DBL+ vacuoles expressed as
1975 a percentage of the total stained vacuoles in (E). Two-sided *t*-test, $n = 5$ biological replicates. **(G)**
1976 Immunofluorescence differentiation assays of parasite strains with or without BFD1, depleted of PKA
1977 C3 or SPARK with 500 µM IAA and grown under unstressed conditions or alkaline stress for 48 h. **(H)**
1978 The percentage of DBL^+ vacuoles corresponding to (G). One-sided *t*-test. **(I)** Effects of 24 hours of PKA
1979 C3 knockdown on the transcriptome relative to the untagged strain. Dotted lines correspond to an
1980 absolute $\log_2$ change of 1. Genes significantly affected by BFD1 overexpression (p-value < 0.001 as
1981 previously defined (Waldman et al., 2020)) are colored according to $\log_2$ change in the chronic-stage
1982 transcriptome. Highlighted points are discussed in the text.
1983

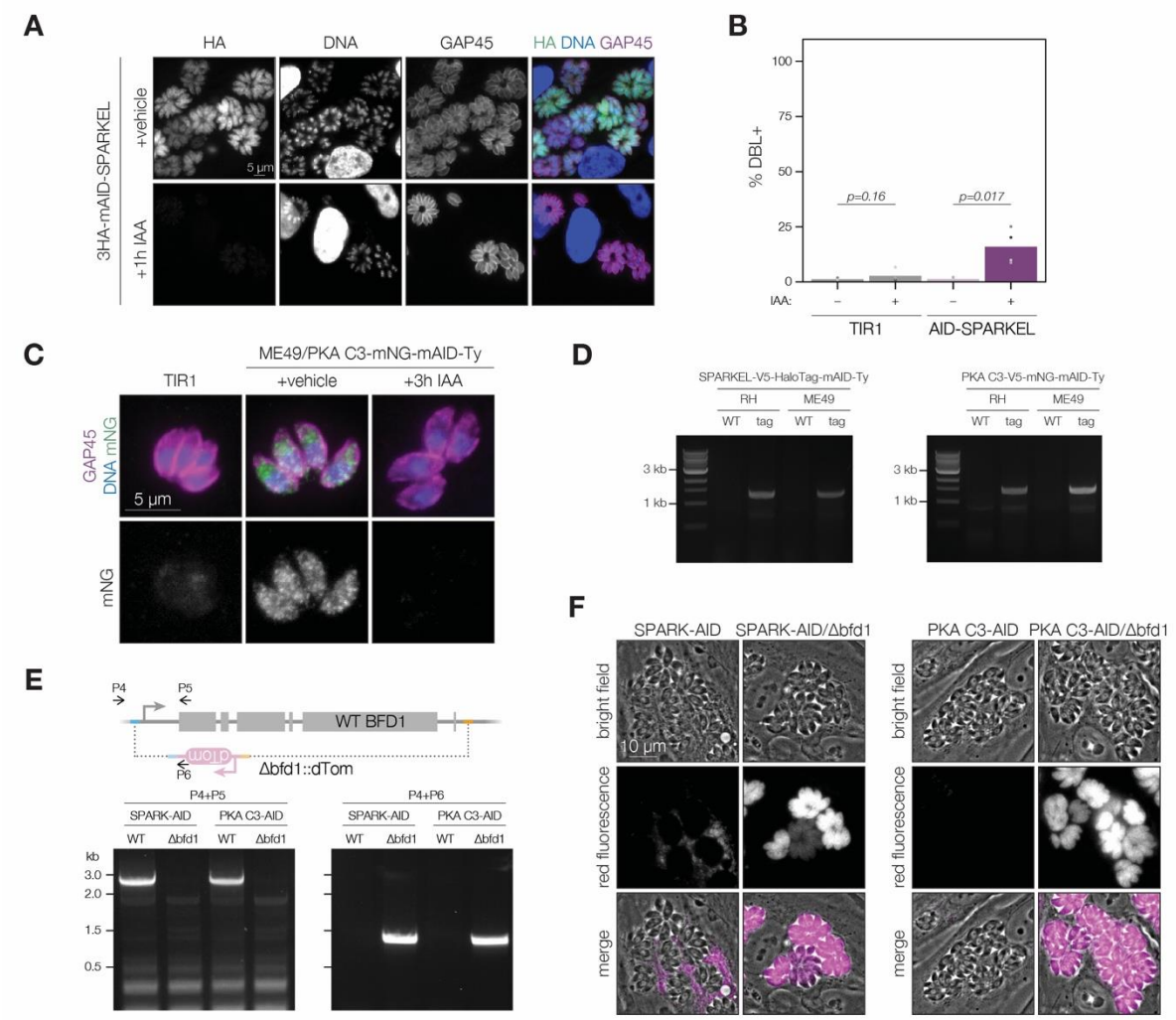

Figure 6—figure supplement 1. (A) Fixed, intracellular RH/3HA-mAID-SPARKEL parasites visualized by immunofluorescence microscopy using the HA epitope after 1h of vehicle or IAA treatment. The HA signal was normalized to the vehicle-treated sample. **(B)** Quantification of the number of DBL+ vacuoles expressed as a percentage of the total stained vacuoles following 48h of AID-SPARKEL knockdown. Two-sided t-test. **(C)** Fixed, intracellular ME49/PKA C3-mNG-AID parasites visualized by immunofluorescence microscopy using the mNG epitope after 3h of vehicle or IAA treatment. The mNG signal was normalized to the vehicle-treated sample. **(D)** Amplification of the SPARKEL-AID and PKA C3-AID genomic loci using tag-specific primers to confirm correct integration of the tagging payload. The integration was confirmed with Sanger sequencing between the 3' gene junction and CDPK3 3'UTR from the tag (Smith et al., 2022). **(E)** The strategy used to knock out BFD1 with a dTomato cassette containing homology to sequenced flanking the BFD1 locus (Waldman et al., 2020). Amplification of sequences specific to the intact locus or dTom knockout for the indicated strains are shown below the schematic. Oligonucleotide sequences are listed in Supplementary Table 5. **(F)** Live microscopy images of intact or Δbfd1::dTom parasites showing red fluorescence arising from the knockout cassette.

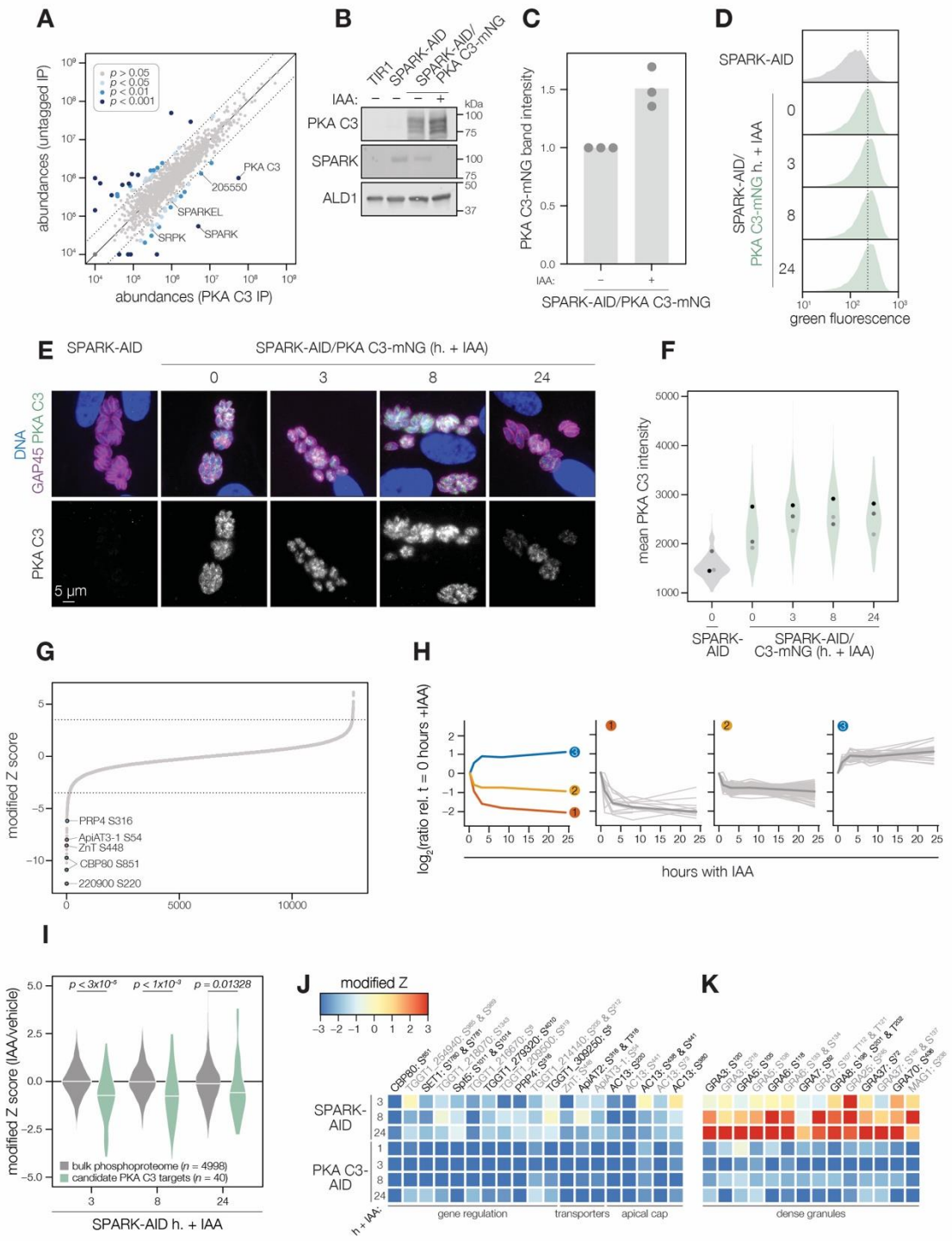

Figure 7. SPARK and PKA C3 physically and genetically interact. (A) Protein abundances from immunopurified PKA C3-mNG-AID lysates or an untagged control strain. Dotted lines correspond to one modified z-score. Only proteins quantified by greater than one peptide are shown. Proteins identified in only one IP were assigned a pseudo-abundance of $10^{4.5}$. Point colors correspond to significance thresholds. **(B)** Immunoblot of parasites expressing SPARK-V5-AID-HA and PKA C3-mNG after 24 hours of IAA treatment. ALD1 serves as a loading control. Band intensity normalized to the dual-tagged strain is shown in **(C)** from 3 replicates. **(D)** Flow cytometry analysis of SPARK-AID

2009 parasites expressing PKA C_3-mNG treated with IAA for the indicated number of hours. Traces are
2010 representative of two biological replicates. The dotted line centers the mode of the vehicle-treated
2011 sample. Traces were normalized by unit area. **(E–F)** Fixed, intracellular SPARK-AID/PKA C_3-mNG
2012 parasites visualized by immunofluorescence microscopy using the mNG epitope after the indicated
2013 period of IAA treatment **(E)**. The mNG signal was internally normalized to the SPARK-AID parental
2014 strain. Quantification of the PKA C_3 signal intensity of three replicates is shown in **(F)**. **(G)**
2015 Phosphopeptide IAA-dependent score (summed peptide ratios relative to the PKA C_3-AID t_0 peptide
2016 abundance). Dotted lines correspond to 3.5 modified Z scores. Colored points correspond to
2017 phosphosites discussed in the main text. **(H)** Gaussian mixture modeling of PKA C_3-dependent peptides
2018 identified by more than one PSM revealed three kinetically resolved clusters. Individual peptides or the
2019 median ratios in each cluster are depicted by light and dark gray lines, respectively. Clusters are
2020 numbered according to their discussion in the main text. **(I)** Violin plots displaying the distribution of
2021 phosphopeptide abundance values following SPARK depletion. The distributions of candidate PKA C_3
2022 targets are shown in green. The distributions and p-values (KS test) were derived from the overlapping
2023 subset of phosphopeptides identified in each dataset. **(J)** Heat map of the abundance ratios of
2024 candidate PKA C_3 targets following SPARK depletion. **(K)** Heat map of the abundance ratios of dense
2025 granule proteins following SPARK depletion, as discussed in the text.
2026

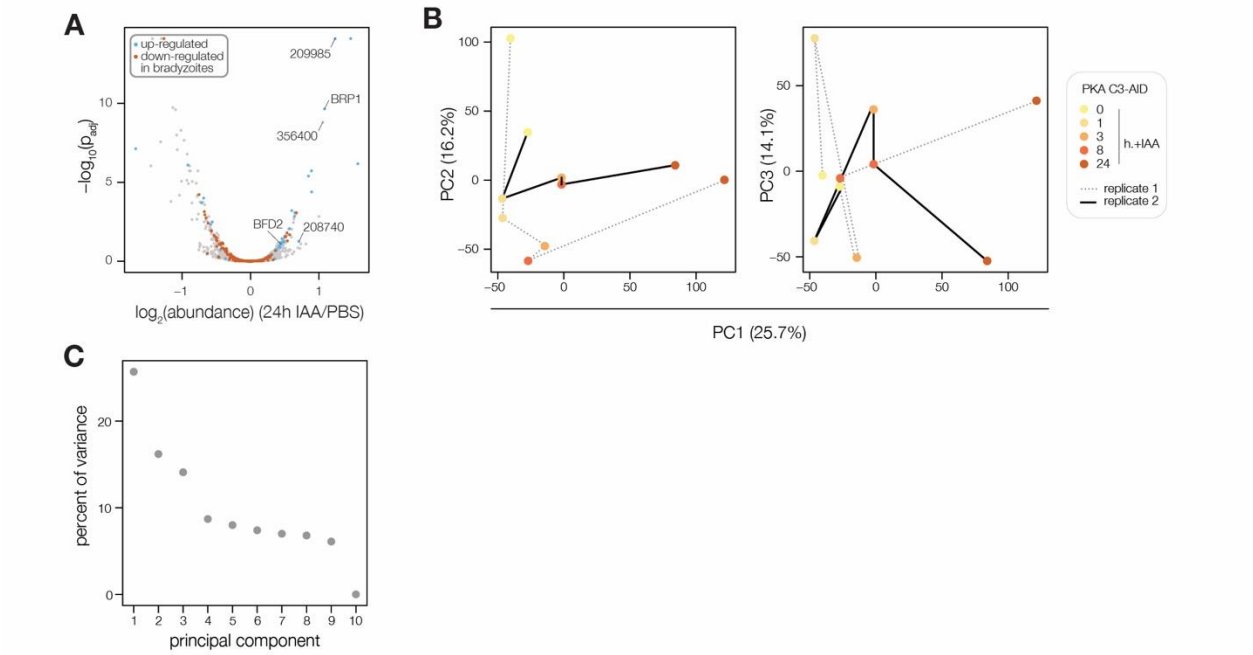

Figure 7—figure supplement 1. Extended analysis of the PKA C3 depletion proteome. (A) Volcano plot displaying the protein abundance ratios of SPARK-AID parasites treated with IAA or vehicle for 24 hours and adjusted p-values. Proteins identified as up- or down-regulated in parasites overexpressing the driver of differentiation (BFD1) (Waldman et al., 2020) are shown in blue and vermilion, respectively. **(B, C)** Principal component analysis of the PKA C3-AID depletion phosphoproteome. Plots show the three components accounting for the greatest proportion of the variance.